Development of Instrument for Interplanetary Scintillation Observations and Study of Heliospheric Tomography

Kimmo Asel

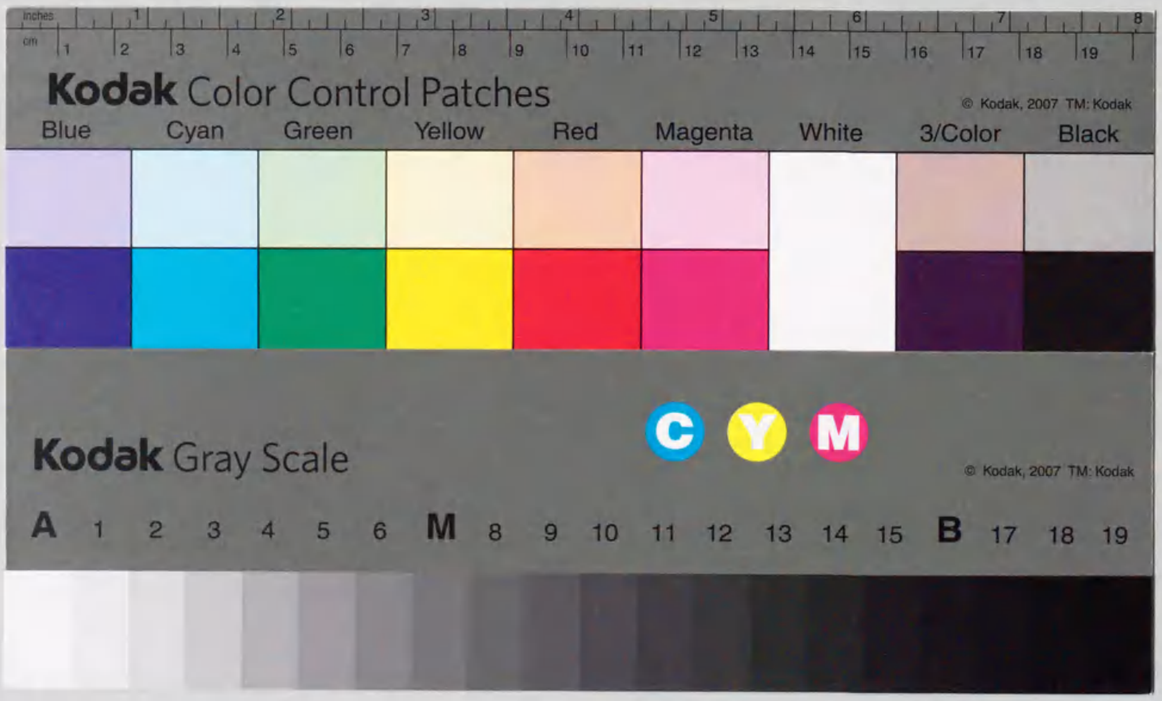

(1)



# Development of Instrument for Interplanetary Scintillation Observations and Study of Heliospheric Tomography

Kikuo Asai

A thesis
submitted for the degree Doctor of Philosophy
in Electric and Electronic Engineering

NAGOYA UNIVERSITY

1998

ABSTRACT OF THE THESIS

Development of Instrument for Interplanetary Scintillation Observations
and Study of Heliospheric Tomography

by
Kikuo Asai
Doctor of Philosophy in Electrical and Electronic Engineering
Nagoya University, Aichi, 1998

The inner heliosphere is filled with the solar wind which is a radial outflow of fully ionized gas carrying the magnetic field and density fluctuations. Interplanetary scintillation (IPS) caused by radio scattering due to the electron density irregularities is used to probe the solar wind. The solar wind observations using the IPS have been carried out at the Solar-Terrestrial Environment Laboratory which has four separated radio telescopes operated at a frequency of 327MHz. The forth telescope was constructed at Kiso in 1993, requiring high sensitivity to measure a large number of compact radio sources.

This thesis presents the optimum-design method of the primary feed installed in an asymmetric parabolic cylinder antenna and the calibration methods of gain and phase in the phased array system. The relationship is examined between illumination efficiency and structure parameters of the primary feed. The optimum-designed primary feed then gave high aperture efficiency of 71% including reflection efficiency. We have introduced three methods to calibrate the phased array system. The loop-method can keep the gain error less than $\pm 0.1$dB and the phase error less than $\pm 2°$ for all the array-elements. The loop-method is compared with Rotating Electric-Field Vector method to check the paths which are not measurable with the loop-method. The reflection-method is also used to determine the absolute gain for each array-element.

Although the IPS is a useful means to measure global structure of the solar wind, direct results from IPS observations indicate solar wind properties integrated along the line-of-sight. We have developed a computer assisted tomography (CAT) program to remove this path integration effect. The program uses solar rotation and solar wind motion to provide perspective views of the solar wind, and requires data both of velocity and scintillation index. We have found from a CAT analysis that the relation between wind speed ($V$) and electron density fluctuations ($\delta N_e$) appears to be $\delta N_e \propto V^{-0.5}$ on the spatial scales around 100 km at heliocentric distances between 0.3 and 0.8 AU.

To my parents

ACKNOWLEDGMENTS

I would like to express my sincere gratitude to my advisor, Professor Masayoshi Kojima for giving me the opportunity of this work and constant guidance throughout the research. We have discussed many topics like IPS observations, scintillation theory, remote sensing technique, and solar wind physics. From the IPS observations, he demonstrated significance to obtain high-quality data for producing new results and keeping the advanced research. His unique ideas extend beyond academic matters into our research circumstances and daily lives. I was very comfortable living in the WDC with the observation system for three years. I am grateful to Associate professor Munetoshi Tokumaru for helpful suggestions and comments in my tomography analysis and understanding on interplanetary physics. I wish to thank Professor Tadahiko Ogawa and Professor Tatsuki Ogino for careful readings of this thesis and helpful comments.

My special thanks are due to Technical Officials Y. Ishida, K. Maruyama, and N. Yoshimi who have continuously helped me on technical information and engineering skills such as manufacture of low noise amplifiers, measurements of the phase shifter characteristics, calibration experiments of the phased array system, scintillation index observations, and so on. I am thankful to Mrs. Yoshida for her clerical supports.

I would also like to extend my deep appreciation to Dr. H. Misawa for valuable discussions and useful advise in proceeding the research. His bearded face was very impressive and attracted me into the IPS group. I learned an attitude toward research through his daily research. I wish to thank Dr. H. Washimi and Dr. T. Watanabe for giving me understandable interpretation about plasma physics and solar physics through their seminars.

During this work many scientists visited the STELab as short time visitors, and I learned a great deal from discussing about the research with them and listening to their understandable lectures. I am thankful to Dr. P. K. Manoharan for many suggestions on obtaining the scintillation index using our IPS observation system. Half year later after his stay, I had a chance to go to India for participating in the IAU Colloquium, and met him again. We had a long travel to Ooty by Indian train, and at last I could see the Ooty Radio Telescope which is the same shape as ours. I am also grateful to Dr. B. V. Jackson and Dr. P. L. Hick for many useful discussions and comments for my "tomography" paper. They especially gave me many good suggestions as to how I can improve English.

The graduate students of our IPS group gradually increased during my stay in the STELab. We held seminars every week, including the staffs. In the seminar we discussed about many scientific topics with my mates, Y. Kozuka, Y. Yamauchi, H. Watanabe, A. Yokobe, M. Hamada, H. Waki, E. Furukawa, Y. Uramoto, K. Miyasato, M. Mori, and S. Nozawa.

I spent the first two years at the student dormitory in the STELab with my

friends, S. Goto, K. Nakamura, F. Takahashi, and H. Yoshikawa who belonged to the same department in the Graduate School of Engineering. We shared much time at the student dormitory together and enjoyed playing softball, badminton, and ski tours. H. Ohsaki, M. Ohyama and I made an exciting trip to Indonesia to visit Dr. R. Mamat who had stayed at our laboratory for around one year. Of the ten day travel in Indonesia we had trouble with our stomach due to the food for two days. But Dr. Mamat took care of us very well. It was a very memorable experiences for us. My thanks also go to N. Yokoyama and H. Matsuoka who were regular members of the "Friday's Meeting". We discussed about many things watching on TV, the program "Ironman on Cook". Also, I would like to express my special thanks to all the staff of the STELab.

Unfortunately, I could not complete this thesis while I stayed in the STE Lab. I would like to thank to Drs. K. Kondo, K. Tanaka, H. Ohnishi, T. Kobayashi, K. Yuki, and Z. Hayashi, who are my colleagues at National Institute of Multimedia Education, for their generosity and support in permitting me to spare time for completing this thesis.

Finally, I would like to acknowledge the continuous and warm supports of my family. Thank you.



## PUBLICATIONS

"Design of an Asymmetric Parabolic Cylinder Antenna with High Aperture Efficiency", K. Asai, M. Kojima, H. Misawa, Y. Ishida, K. Maruyama, N. Yoshimi, M. Wakasa, and M. Karakida, *Transactions of the Institute of Electronics, Information and Communication Engineers* (Japanese), Vol. J78-B-II, No. 3, pp.102-109, March 1995.

"Multi-Station System for Solar Wind Observation using the Interplanetary Scintillation Method", K. Asai, Y. Ishida, M. Kojima, K. Maruyama, H. Misawa, and N. Yoshimi, *Journal of Geomagnetism and Geoelectricity*, Vol. 47, pp.1107-1112, 1995.

"Calibration of Gain and Phase on the Phased Array System Installed in a Radio Telescope ", K. Asai, M. Kojima, Y. Ishida, K. Maruyama, N. Yoshimi, H. Misawa, and K. Miyasato, *Transactions of the Institute of Electronics, Information and Communication Engineers* (Japanese), Vol. J79-B-II, No. 12, pp.994-1002, December 1996.

"Heliospheric tomography using interplanetary scintillation observations III – Correlation between speed and electron density fluctuations in the solar wind", K. Asai, M. Kojima, T. Tokumaru, A. Yokobe, B. V. Jackson, P. L. Hick, and P. K. Manoharan, *Journal of Geophysical Research*, Vol. 103, No. A2, pp.1991-2001, 1998.

# Contents

# Chapter 1

# Introduction

## 1.1 Solar Wind

The solar wind is an ionized gas (plasma) which flows radially away from the Sun carrying with the solar magnetic field into interplanetary space. The outward flow of the solar wind carves out a spatial cavity, known as the heliosphere, in the local interstellar medium. The solar wind also encounters the Earth whose magnetosphere traps plasma particles. This interaction produces geophysical phenomena as Aurora, magnetic storms, and so on. Interplanetary disturbances related with solar flares often give damages to radio communications, satellite instruments, and electric power lines. The research of the solar wind has increasingly become important because it is expected that manned space activity and space utilization make further progress in the 21st century.

The solar wind was theoretically predicted by E. N. Parker [1] who proposed a hydrodynamic model. The model is that the solar wind is driven outward to supersonic velocities as a result of high coronal temperature ($> 10^6$ K) and large difference in gas pressure between the solar corona and the interstellar space, despite the restraining influence of solar gravity. The *in situ* observations have been performed after Parker's prediction, within a few years of 1960 (Russian deep-space probes Luna 3 and Venus 1 launched in 1959 [2], American space probe Explore 10 launched in 1961, and Mariner 2 sent to Venus in late 1962 [3]). They demonstrated that the interplanetary space was pervaded by a supersonic flow of magnetized plasma and confirmed Parker's hydrodynamic model of the solar wind.

Observations of the solar wind have been made from spacecraft such as Pioneer, Voyager (planetary missions), Helios [4], IMP satellite (Earth's orbit), and so on, which enabled us to explore wide heliosphere regions. However, these spacecraft observations have been confined to regions near the ecliptic plane. The ULYSSES spacecraft has recently made a northbound pass over both solar poles at a heliocentric distance of 2 to 4 AU [5], and encountered continuous fast wind at high latitudes, generally in a rage of 700 to 800 km $s^{-1}$ [6]. There has been no direct measurement at solar distance inside 70 $R_\odot$ where the solar wind is significantly accelerated. The various phenomena near the Sun have been measured with the indirect measurements such as SOHO (Solar and Heliospheric Observatory) mission, Yohkoh X-ray observations, ground-based remote sensing observations, etc.

### 1.1.1 Properties

The physical properties of the solar wind around the orbit of the Earth (1 AU: one astronomical unit from the Sun's center) are summarized in Table 1.1. The solar wind is categorized to two modes: low-speed wind and high-speed wind. In low solar activity, the high-speed wind emanates from coronal holes which appear at polar regions, while the low-speed wind is distributed along the equatorial streamer belt. During the solar activity maximum, the low-speed wind occupies the entire region of the Sun. Interestingly, proton temperature of the high-speed wind is higher than that of low-speed wind at 1 AU in spite of the opposite condition at their source regions in the corona. Furthermore, as shown in Table 1.1, fast solar wind has different temperature at 1 AU between the proton and the electron. Two-fluid model were proposed [7, 8], and explained the electron temperature ($T_e$) with electron heat conduction ($T_e \propto r^{-2/7}$) and the proton temperature ($T_p$) with adiabatic cooling ($T_p \propto r^{-4/3}$). This predicts that the proton temperature is lower than the electron temperature at 1 AU taking the same temperature at the corona base. However, $T_p > T_e$ has been observed in the fast solar wind. Some mechanisms are necessary for the selective proton heating in the fast solar wind.

The magnetic field can be "frozen-in" to the solar wind plasma because the



Table 1.1: Properties of the solar wind at 1 AU.

| Property | Low-speed wind | High-speed wind |
|---|---|---|
| Flow speed | <450 km $s^{-1}$ | 700~800 km $s^{-1}$ |
| Proton density | ~10 $cm^{-1}$ | 2~3.5 $cm^{-1}$ |
| Flux density | $3\times10^8$ $cm^{-2}$ $s^{-1}$ | $2\times10^8$ $cm^{-2}$ $s^{-1}$ |
| Temperature | $T_p \sim 4\times10^4$ K | $T_p \sim 2\times10^5$ K |
| | $T_e \sim 1.3\times10^5$ K | $T_e \sim 10^5$ K |
| | $T_p < T_e$ | $T_p > T_e$ |
| | $T_p$: isotropic | $T_p(\perp) > T_p(\parallel)$ |
| Associated with | Quiet regions | Coronal holes |
| Structure | Filamentary | Uniform |
| In sunspot minimum | Equatorial streamer belt within ±20° | Polar regions above 20° |
| In sunspot maximum | Dominant | Compact regions around pole |

conductivity of the plasma is so high (collisionless), so that the diffusion of the magnetic field is negligible. In the low corona the magnetic field dominates the plasma while above the source surface, which is at a distance of 2.5 $R_\odot$ (solar radii) from the Sun's center, the plasma flow drags out the frozen-in magnetic field with it. The solar wind flow expands radially outward from the Sun and the Sun rotates with a period of about 27 days for an observer at the Earth. These facts make the magnetic field lines into Archimedes spirals. Since the solar wind has two modes on velocity as shown in Table 1.1, which are fast solar wind and slow solar wind, the spirals of the fast solar wind are less tightly wound than those of the slow solar wind. The fast stream overtakes and collides with the slow wind region. However, the high electric conductivity of the magnetized plasma inhibits penetration into different streams. The fronts of the fast solar wind is then compressed producing high densities, which is referred to as a corotating interaction region (CIR). A shock front would be formed at the leading edge of the compressed region, between 1 and 3 AU. A rarefaction region forms behind the fast stream with lower density.

The Sun has an 11 year activity cycle which is identified in a sunspot number. A series of synoptic maps of solar wind speed over the last 11 years is shown in Figure 1.1. These synoptic maps were made with tomography analysis using the data from interplanetary scintillation observations (see Chapter 5 for details). These maps display

clearly the evolution of the large-scale structure. Comparisons with magnetic field and white light corona observations [9] have revealed relationship on the solar cycle change between solar wind speed and coronal structure. In the minimum phase of solar activity fast flows appear from the solar poles to the middle latitudes which are low-density open magnetic field regions of coronal holes and slow streams appear along the neutral sheet which is nearly located above dense closed-field regions near the solar equator [10]. In the minimum condition typical of 1986 and 1995 to 1996 in Figure 1.1, the boundary between the fast and slow wind regions has a steep gradient that is consistent with the recent ULYSSES observations [6]. Near solar activity maximum the solar wind structure exhibits approximately spherical symmetry with a mean speed around 400 km $s^{-1}$ [11] and the magnetic field becomes complicated. Interplanetary transients often occur such as shock waves and plasma clouds associated with solar flares and coronal mass ejections (CMEs).

### 1.1.2 Density Fluctuations

Observations of soft X-rays provide more direct views of hot plasma in the solar corona. The X-ray images by Skylab and Yohkoh satellite have revealed that coronal holes of dark brightness regions are identified as the source of fast solar wind [12, 13]. Temperature in the coronal holes is less than or comparable with that in quiet regions [14, 15, 16] where the kinetic temperature is about $2 \times 10^6$ K at the corona. According to the thermal driven model of Parker's theory, the solar wind from the coronal holes should not be so fast as that from actual observations [10, 17, 18]. Recent SPARTAN observations show that the plasma above coronal holes has kinetic temperature of $7 \times 10^6$ K at a few $R_\odot$ [19]. It has been suggested that the thermal-driven model is not enough to understand the fast solar wind from coronal holes, and this requires some mechanisms to heat and accelerate the fast solar wind additionally [20]. One of the most possible candidates for the important energy source is dissipation of MHD waves, particularly Alfvén waves, because *in situ* measurements of the solar wind show evidence for Alfvénic fluctuations [21, 22]. These fluctuations are considered to be mainly remnants of Alfvén waves generated at the magnetic reconnection region above the closed loop [23]. McKenzie



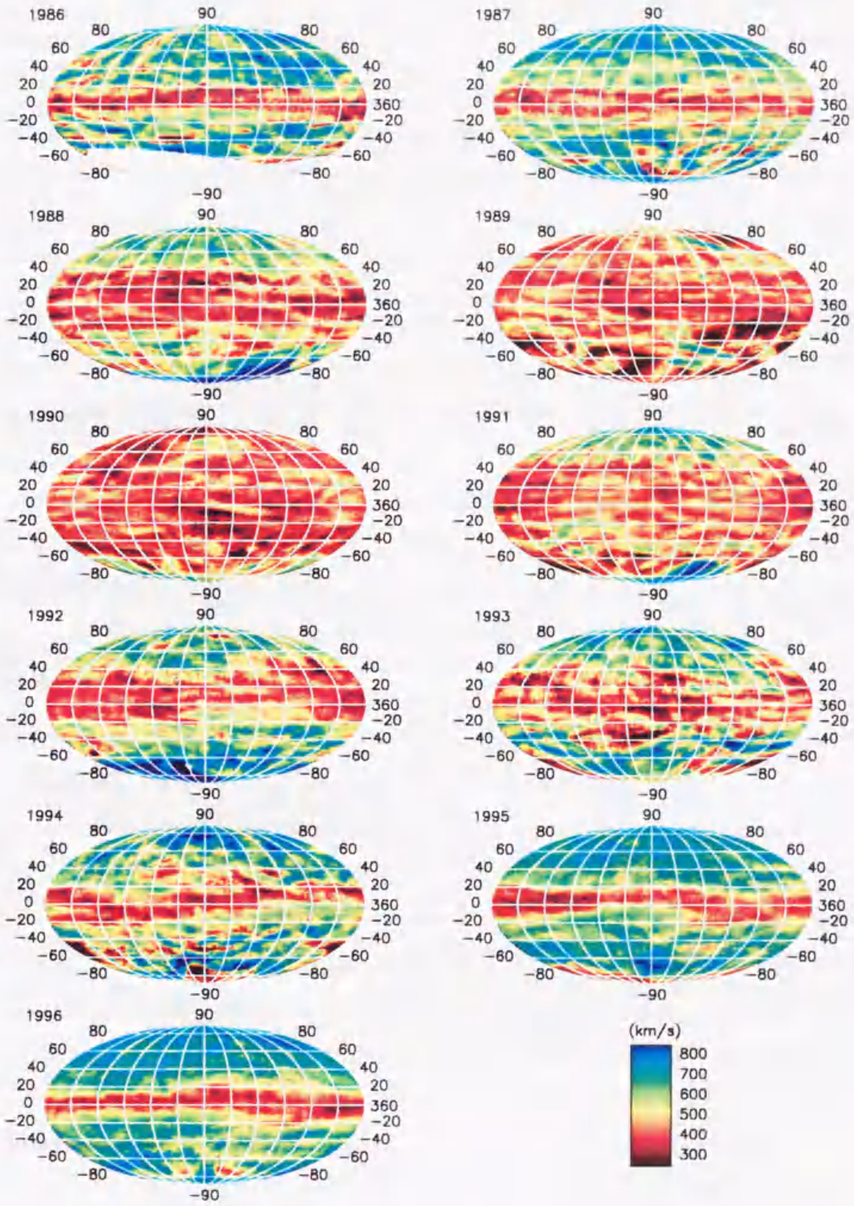


Figure 1.1: Synoptic maps of the solar wind speed in the coordinate of the Carrington longitude and heliographic latitude, produced by using IPS data from the Solar-Terrestrial Environment Laboratory.

et al. [24] has suggested that efficient dissipation requires any Alfvén waves responsible to have frequencies in the range of 0.01 Hz to 10 kHz. If Alfvén waves propagating outward from the Sun transfer energy to the solar wind [25], they can also affect the turbulence level of density fluctuations in the solar wind. Thus, the solar wind density fluctuations are an important subject to understand mechanisms of the wave dissipation related to solar wind acceleration and coronal heating. The density fluctuations are measurable with interplanetary scintillation.

The density fluctuations of the solar wind exhibit power-law spectrum $\Phi(\kappa) \propto \kappa^{-\alpha}$ where $\kappa$ is the three-dimensional wavenumber. *In situ* measurements of density fluctuations have shown a Kolmogorov like spectrum at the large scale range [26, 27, 28]. The density fluctuations of scale sizes smaller than $10^3$ km have been measured by various radio propagation observations using spacecraft signals and natural radio sources, such as intensity scintillations, spectral broadening, and phase scintillations [29, 30, 31, 32, 33]. The investigations by Coles and Harmon [34] and Coles et al. [35] indicate that the electron density spectrum has a Kolmogorov power-law form ($\alpha$=11/3) for scales greater than $10^3$ km, local flattening ($\alpha \approx 3$) for the smaller scales, and steepening at much smaller scales.

Tu and Marsch [28] made a spectral analysis of the fractional proton density fluctuations $\delta N_P/N_P$ at the wavenumbers of $10^{-7}$ to $3\times10^{-5}$ km$^{-1}$, measured by the Helios spacecraft at distances beyond 0.3 AU. In low-speed wind the power spectra are generally Kolmogorov-like (one-dimensional spectral index of -5/3) and the power density stays fairly constant with the solar distance. In high-speed wind the spectral index shows a flattening at the small scales and the power density increases with the solar distance at the large scales. The power spectra indicate that the power density of the high-speed wind becomes comparable with that of the low-speed wind at wavenumbers larger than $2 \times 10^{-5}$ km$^{-1}$, though the power density in the low-speed wind is higher than that in the high-speed wind at the smaller wavenumbers. The local flattening implies power enhancement, and the steepening suggests a dissipation process of the turbulence. There is another evidence that supports the power enhancement at the intermediate scales. Unti et al. [27] presented power spectra between 0.0048 and 13.3 Hz of the solar wind

flux observed by the satellite OGO 5 at the Earth orbit. They noted enhancements in power spectra of solar wind ion flux at frequencies around 0.5 Hz.

The power-law index $\alpha$ of the density fluctuation spectrum also depends on the radial distance from the Sun [36] and solar wind speed [33] as well as the spatial scale. Manoharan et al. [33] showed the speed dependence of spectral index that increases from 2.8 to 3.5 for a speed increase of 250 to 650 km $s^{-1}$ at the spatial wavenumber of $2\times10^{-3}$ to $10^{-1}$ $km^{-1}$. Yamauchi et al. [36] showed the radial dependence of spectral index that varies from 2.9 to 3.6 for the solar distance of 10 to 60 $R_\odot$ in the spatial wavenumber range of $2\times10^{-2}$ to $2\times10^{-1}$ $km^{-1}$.

## 1.2 Interplanetary Scintillation

When radio waves from a distant compact radio source pass through the solar wind, they are scattered by electron density irregularities in the solar wind. The scattered radio waves propagating to the earth interfere with each other, and produce a diffraction pattern on an observer's plane. Since the density irregularities drift with the solar wind, the diffraction pattern moves with the velocity of the solar wind. Then it makes intensity fluctuations of the received signals. This phenomenon is referred to as "interplanetary scintillation (IPS)". The radio scintillation process is analogous to the "twinkling" of the starlight due to the density irregularities in the earth's atmosphere.

Compact natural radio source such as Quasars, Pulsars, and $H_2O$ maser can be used for the IPS measurements. In fact, since radio waves from the distant source pass through not only interplanetary medium but also interstellar medium and Earth's ionosphere, they uniquely affect the radio signals and make the scintillations. The time scales of scintillation depend on the scale size of the diffraction pattern and flow speed. The IPS has time scales typically less than one second, but interstellar scintillation has the order of minutes to days and ionospheric scintillation tens of seconds [37]. Thus, temporal filtering enables us to distinguish just IPS component from others and to probe the solar wind plasmas.

IPS was discovered in 1964 by Hewish, Scott and Wills [38]. The IPS has been



first used to catalog the angular diameter of radio sources [39]. The second application is to probe the solar wind plasma. The velocity of the diffraction pattern can be estimated by measuring time lags of scintillation signals detected at remotely separated receivers. The scintillation level can provide us with information on turbulence in the solar wind [40]. Although the solar wind properties from the IPS observation are biased by a line-of-sight integration, it has several advantages as remote sensing:

1. Measure dynamics and structure of the solar wind in three dimensions, including regions near the Sun and at high latitudes where *in situ* measurements are difficult;
2. Measure long term change such as the solar cycle dependence of the solar wind; and
3. Measure the vast interplanetary space in a short period by using a large number of IPS radio sources.

The largest scale size measurable by the intensity scintillation is limited by Fresnel filtering up to a Fresnel radius (~150 km at 327 MHz). The intensity scintillation gives a scintillation index that is proportional to electron density fluctuations. Since the scintillation index saturates at the strong scattering region close to the Sun, different frequencies are used to probe the various distances from the Sun.

The interferometer technique measures fluctuations in the differential phase on the baseline. The phase scintillation with VLBI (very long baseline interferometer) has observed the spectrum between scales of $10^3$ and $10^4$ km [34]. In addition to the scintillations, radio propagation methods such like source angular broadening are used to probe the interplanetary medium [41]. The angular broadening is a brightness distribution measurement of the radio source and provides two dimensional information on the microstructure of the solar wind turbulence. The angular broadening using VLA (very large array) have observed the electron density fluctuations to be highly anisotropic and radially aligned inside 10 $R_\odot$ at the scales corresponding to the baseline length [42, 43].

If a coherent signal is used instead of natural radio sources, Doppler scintillation is available for measurements of scale sizes larger than 100 km [44]. The Doppler scintillation is obtained from phase by differentiating the phase time series, and reflects

both electron density fluctuations and flow speed. The Doppler scintillation can probe the solar wind plasma over the entire heliospheric distance range from the near-Sun region to near the orbit of the Earth [45]. The spectral broadening of coherent spacecraft beacons [29, 46] has been also used for the spectrum measurements of scale sizes smaller than 100 km. Thus, the radio scattering measurements can cover the wide ranges of the scale size on the spectrum and the solar distance in the inner heliosphere.

Several groups have been making IPS observations with single-station and multi-station system using natural radio sources. The Cambridge group used a single-station with 18000 $m^2$ array at 81.5 MHz [39] and two halves of the 447 m $\times$ 18 m parabolic cylinder reflector as an interferometer of small spacing [47]. The former measured nearly 900 radio sources each day, and focused on interplanetary disturbances detected by calculating daily values of the disturbance factor, g-value [48]. The Radio Astronomy Centre, Tata Institute of Fundamental Research (Ooty, India) has been operating a large parabolic cylinder antenna at a frequency of 327 MHz, which is the same type as ours. The Kashima Space Research Center, Communications Research Laboratory (Kashima, Japan), has been making high-frequency observations at 2 and 8 GHz to measure the near Sun regions. Ooty and Kashima groups use a spectral-fitting method to obtain physical parameters of the solar wind. Multi-station observations have been carried out at the University of California at San Diego (UCSD, USA) and the Solar-Terrestrial Environment Laboratory (STELab), Nagoya University (Japan). They can estimate solar wind velocity from time lags obtained by cross-correlation analysis between the received signals at spaced antennas. The UCSD group operated an 8000 $m^2$ phased array at 74 MHz, but recently they have shifted to use the European Incoherent Scatter (EISCAT) array at 932 MHz, which is a three-station incoherent backscatter radar designed to study the Earth's magnetosphere and ionosphere in the auroral zone.



## 1.3 Multi-Station System for Interplanetary Scintillation Observations

We have been carrying out solar wind measurements using the interplanetary scintillation (IPS) method since the early 1970s, and have been producing synoptic maps of solar wind speed. Our IPS observations were started at a frequency of 69 MHz (VHF) using a three-station system consisting of Toyokawa, Fuji and Sugadaira (Figure 1.2), which are widely separated from each other. At this frequency, however, the IPS of natural radio signals cannot probe the solar wind at distances within 0.3 AU because radio scattering becomes strong. Although solar wind measurements within 0.3 AU are particularly important to study the acceleration mechanisms of the solar wind and dynamics of traveling interplanetary disturbances, *in situ* measurements have not been made so far. Therefore we shifted the frequency to 327 MHz (UHF) so that the IPS can probe the distances within 0.3 AU.

Three UHF radio telescopes were built from 1977 to 1982 at the same sites where the VHF observations had been carried out. The IPS observations at UHF permit us to measure the solar wind plasma at heliocentric distances of 0.1 to 1 AU as well as at all heliographic latitudes. One more telescope was built at Kiso in 1993 [49] to construct a four-station system (Figure 1.2) for more extended observations. This new telescope has improved our IPS observations on the following points. 1) The baseline length between Toyokawa and Sugadaira is a little longer than a Fresnel radius at 327 MHz: when a solar wind flow is projected nearly perpendicular to this baseline, the cross-correlation of IPS signals obtained at these two stations is rather low and this makes velocity estimate less reliable. The Kiso station is located midway between Toyokawa and Sugadaira, and makes two shorter baselines. 2) The radio environment at Toyokawa is now quite noisy because of the rapid growth of industrial factories: the new site can be used as a replacement for this noisy site. 3) Four stations are minimally necessary to obtain the full parameters of a flow vector, the spatial anisotropy of density turbulence and their error estimate from the cross-correlation analysis when random velocities exist near the sun [50].

We are now carrying out the solar wind observations using the four-station system. Each station is fully-automatically operated and connected to the host station


Figure 1.2: Geometrical arrangement of the four stations. Toyokawa is the host station, where the STELab is located.



(Toyokawa) with two public telephone lines for system control and data acquisition. Observations are carried out on a routine basis through the year except during the winter season. Besides their use for the IPS, the Kiso and Fuji telescopes have been used for observations of a millisecond pulsar survey and the comet Shoemaker-Levy 9 collisions with Jupiter.

## 1.4 Outline of the Thesis

The purpose of this thesis is to study global structure of the solar wind with IPS observations, and to develop instruments for the IPS observations. The study of the solar wind concentrates on relationship between solar wind speed and density fluctuations at heliocentric distance beyond 0.3 AU during the low solar activity. For this data analysis we developed a computer assisted tomography (CAT) technique for eliminating the bias due to effect of the line-of-sight integration on IPS. The CAT analysis with good spatial and temporal resolution requires good quality of the IPS data. The IPS data are obtained by detecting the intensity fluctuations of the faint signals from distant radio sources. So a radio telescope with high sensitivity is necessary for receiving the signals. We have then developed and improved the UHF radio telescopes dedicated to the IPS observations. The works in this thesis focus on design of the feed system of an asymmetric parabolic cylinder antenna and development of gain and phase calibration system of the phased array system installed in the UHF radio telescope.

Chapter 2 presents system synopsis of the UHF radio telescope dedicated to the IPS observations. Since the design of the telescope system at each station is basically the same, we here describe the antenna system, feed system, and receiver system of Kiso radio telescope which is the newest one constructed in 1993. The specifications and performance of the Kiso radio telescope are displayed. After the construction of the Kiso radio telescope, we have conducted the upgrade project for the other telescopes (Toyokawa, Fuji, and Sugadaira station). Improvements in the upgrade project are reported, and performance is compared between the pre- and post-improvements.

Chapter 3 presents design technique used to maximize aperture efficiency of an

asymmetric parabolic cylinder antenna. The aperture efficiency is discussed with respect to illumination efficiency and reflection efficiency. We calculate dependence of the illumination efficiency on various structure parameters of primary feed network which consists of the phased array with a corner reflector. The reflection efficiency is estimated from transmission loss and phase error loss of the reflecting surface. Including the illumination efficiency and reflection efficiency, the aperture efficiency is estimated to be 75.9%. The estimated aperture efficiency is confirmed with the actual measurement of a natural radio source.

Chapter 4 presents calibration methods of the phased array system installed in the feed network of the UHF radio telescope. Relative gain and phase among each array-element should be calibrated for source-tracking with the phased array. Several methods to measure the gain and phase are discussed. First, problems of the previous method are disclosed. Second, a loop-method is introduced to solve the problem. Although the loop-method is useful for determining the gain and phase of the phased array system backward from pre-amplifier units, one cannot measure the gain and phase in the path from the antenna reflector to the pre-amplifier input. Therefore, the rotating electric-field vector method (REV-method) is tried in order to deal with all the path from the reflector through the pre-amplifier units. The loop-method is compared with the REV-method, and the difference between their methods is estimated.

Chapter 5 presents analysis of IPS data obtained at the Solar-Terrestrial Environment Laboratory (STELab). It is shown how electron density fluctuations in the solar wind at scale sizes around 100 km is related to the speed in the heliocentric distance range of 0.3 to 0.8 AU. The solar wind properties derived from the IPS data are biased by line-of-sight integration through the three-dimensional structured solar wind. Therefore, a computer assisted tomography (CAT) technique is applied to deconvolve the line-of-sight integration to reconstruct the solar wind structure. The analysis was made for the solar wind speed $V$ and electron density fluctuations $\delta N_e$ in the solar activity minimum phase. From results of the CAT analysis, the best fit power-law relation of $\delta N_e \propto V^{-\gamma}$ is calculated, and the relationship between speed and fractional electron density fluctuations $\delta N_e/N_e$ is estimated.

# Bibliography


[1] E. N. Parker, Dynamics of the interplanetary gas and magnetic fields, *Astrophysical Journal*, **128**, pp.664–676, 1958.

[2] K. Gringauz, Some results of experiments in interplanetary space by means of charged particle traps on soviet space probes, *Space Research II COSPEAR*, pp.539–553, 1961.

[3] M. Neugebauer, and C. Snyder, Mariner 2 observations of the solar wind, *Journal of Geophysical Research*, **71**, pp.4469–4484, 1966.

[4] R. Schween, and E. Marsch (Eds.), *Physics of the Inner Heliosphere*, Springer-Verlag, Berlin Heidelberg, 1990.

[5] E. J. Smith, R. G. Marsden, and D. E. Page, Ulysses above the sun's south pole: An introduction, *Science*, **268**, pp.1005–1006, 1995.

[6] J. L. Phillips, S. J. Bame, A. Barnes, B. L. Barraclough, W. C. Feldman, B. E. Goldstein, J. T. Gosling, G. W. Hoogeveen, D. J. McComas, M. Neugebauer, and S. T. Suess, Ulysses solar wind plasma observations from pole to pole, *Geophysical Research Letters*, **22**, pp.3301–3304, 1995.

[7] P. A. Sturrock, and R. E. Hartle, Two-fluid model of the solar wind, *Physical Review Letters*, **16**, pp.628–631, 1966.

[8] R. E. Hartle, and P. A. Sturrock, Two-fluid model of the solar wind, *Astrophysical Journal*, **151**, pp.1155–1170, 1968.

[9] B. J. Rickett, and W. A. Coles, Evolution of the solar wind structure over a solar cycle: Interplanetary scintillation velocity measurements compared with coronal observations, *Journal of Geophysical Research*, **96**, pp.1717–1736, 1991.

[10] M. Kojima, and T. Kakimuna, Solar cycle dependence of global distribution of solar wind speed, *Space Science Reviews*, **53**, pp.173–222, 1990.

[11] W. A. Coles, B. J. Rickett, V. H. Rumsey, J. J. Kaufman, D. G. Turley, S. Ananthakrishnan, J. W. Armstrong, J. K. Harmons, S. L. Scott, D. G. sime, Solar cycle changes in the polar solar wind, *Nature*, **286**, pp.239–241, 1980

[12] A. S. Krieger, A. F. Timothy, and E. C. Roelof, A coronal hole and its identification as the source of a high velocity solar wind stream, *Solar Physics*, **29**, pp.505–525, 1973.

[13] D. G. Sime, and B. J. Rickett, Coronal density and the solar wind speed at all latitudes, *Journal of Geophysical Research*, **86**, pp.8869–8876, 1981.

[14] G. L. Withbroe, The temperature structure, mass, and energy flow in the corona and inner solar wind, *Astrophysical Journal*, **325**, pp.442–467, 1988.

[15] H. Hara, S. Tsuneta, L. W. Acton, M. E. Bruner, J. R. Lemen, and Y. Ogawara, Temperatures of coronal holes observed with the Yohkoh SXT, *Publications of the Astronomical Society of Japan*, **46**, pp.493–502, 1994.

[16] R. Kano, and S. Tsuneta, Temperature Distributions and energy scaling law of solar coronal loops obtained with Yohkoh, *Publications of the Astronomical Society of Japan*, **48**, pp.535–543, 1996.

[17] W. A. Coles, R. Esser, U.-P. Løvhaug, and J. Markkanen, Comparison of solar wind velocity measurements with a theoretical acceleration method, *Journal of Geophysical Research*, **96**, pp.13849–13859, 1991.

[18] R. R. Grall, W. A. Coles, M. T. Klinglesmith, A. R. Breen, P. J. S. Williams, Jussi Markkanen, and Ruth Esser, Rapid acceleration of the polar solar wind, *Nature*, **379**, pp.429–432, 1996.



[19] J. L. Kohl, L. D. Gardner, L. Strachan, R. Fisher, and M. Guhathakurta, Spartan 201 coronal spectroscopy during the polar passes of Ulysses, *Space Science Review*, **72**, pp.29–38, 1995.

[20] A. Barnes, Acceleration of the solar wind, *Reviews of Geophysics*, **30**, pp.43–55, 1992.

[21] J. W. Belcher, and L. Davis, Jr., Large-amplitude Alfvén waves in the interplanetary medium, 2, *Journal of Geophysical Research*, **76**, pp.3534–3563, 1971.

[22] B. Bavassano, and R. Bruno, Large-scale solar wind fluctuations in the inner heliosphere at low solar activity, *Journal of Geophysical Research*, **94**, pp.168–176, 1989.

[23] W. C. Feldman, B. L. Barraclough, J. L. Phillips, and Y.-M. Wang, Constraints on high-speed solar wind structure near its coronal base: a Ulysses perspective, *Astronomy and Astrophysics*, **316**, pp.355-367, 1996.

[24] J. F. Mckenzie, M. Banaszkiewicz, and W. I. Axford, Acceleration of the high speed solar wind, *Astronomy and Astrophysics*, **303**, pp.L45–L48, 1995.

[25] R. Esser, S. R. Habbal, W. A. Coles, and J. V. Hollweg, Hot protons in the inner corona and their effect on the flow properties of the solar wind, *Journal of Geophysical Research*, **102**, pp.7063–7074, 1997.

[26] D. S. Intriligator, and J. H. Wolfe, Preliminary power spectra of the interplanetary plasma, *Astrophysical Journal* **162**, pp.L187–L190, 1970.

[27] T. Unti, and C. T. Russel, On the causes of spectral enhancements in solar wind power spectra, *Journal of Geophysical Research*, **81**, pp.469–482, 1976.

[28] C.-Y. Tu, and E. Marsch, MHD structures, waves and turbulence in the solar wind: observations and theories, *Space Science. Review*, **73**, pp.1–210, 1995.

[29] R. Woo, and J. W. Armstrong, Spacecraft radio scattering observations of the power spectrum of electron density fluctuations in the solar wind, *Journal of Geophysical Research*, **84**, pp.7288–7296, 1979.

[30] L. M. Celnikier, C. C. Harvey, R. Jegou, M. Kemp, and P. Moricet, A determination of the electron density fluctuation spectrum in the solar wind, using ISEE propagation experiment, *Astronomy and Astrophysics*, **126**, pp.293–298, 1983.

[31] L. M. Celnikier, L. Muschietti, and M. V. Goldman, Aspects of interplanetary plasma turbulence, *Astronomy and Astrophysics*, **181**, pp.138–154, 1987.

[32] W. A. Coles, and J. P. Filice, Changes in the microturbulence spectrum of the solar wind during high-speed streams, *Journal of Geophysical Research*, **90**, pp.5082–5088, 1985.

[33] P. K. Manoharan, M. Kojima, and H. Misawa, The spectrum of electron density fluctuations in the solar wind and its variations with solar wind speed, *Journal of Geophysical Research*, **99**, pp.23411–23420, 1994.

[34] W. A. Coles, and J. K. Harmon, Propagation observations of the solar wind near the Sun, *Astrophysical Journal*, **337**, pp.1023–1034, 1989.

[35] W. A. Coles, W. Liu, J. K. Harmon, and C. L. Martin, The solar wind density spectrum near the Sun: Results from Voyager radio measurements, *Journal of Geophysical Research*, **96**, pp.1745–1755, 1991.

[36] Y. Yamauchi, M. Kojima, M.Tokumaru, H. Misawa, H. Mori, T. Tanaka, H. Takaba, T. Kondo, and P. K. Manoharan, Micro-turbulence in the solar wind at 5–76 Rs observed with interplanetary scintillation, *Journal of Geomagnetism and Geoelectricity*, **48**, pp.1201–1217, 1996.

[37] B. Rickett, Radio astronomical scintillation in the interstellar plasma, *Wave propagation in Random Media (Scintillation)*, edited by V. I. Tatarskii, A. Ishimaru, and V. U. Zavorotny, pp.169–185, SPIE and IOP Publishing, 1993.

[38] A. Hewish, P. F. Scott, and D. Wills, Interplanetary scintillation of small diameter radio sources, *Nature*, **203**, pp.1214–1217, 1964.

[39] A. C. S. Readhead, Interplanetary scintillation of radio sources at meter wavelength, II. Theory, *Monthly Notices of Royal Astronomical Society*, **155**, pp.185–197, 1971.



[40] W. A. Coles, Interplanetary Scintillation, *Space Science Review*, **21**, pp.411–425, 1978.

[41] M. K. Bird, Coronal investigations with occulted spacecraft signals, *Space Science Review*, **33**, pp.99–126, 1982.

[42] R. Narayan, K. Anantharamaiah, and T. Cornwell, Refractive radio scintillation in the solar wind, *Monthly Notices of the Royal Astronomical Society*, **241**, pp.403–413, 1989.

[43] J. W. Armstrong, W. A. Coles, M. Kojima, and B. J. Rickett, Observations of field-aligned density fluctuations in the inner solar wind, *Astrophysical Journal*, **358**, pp.685–692, 1990.

[44] R. Woo, Radial dependence of solar wind properties deduced from Helios 1/2 and Pioneer 10/11 radio scattering observations, *Astrophysical Journal*, **219**, pp.727–739, 1978.

[45] R. Woo, Spacecraft radio scintillation and solar system exploration, *Wave Propagation in Random Media (Scintillation)* edited by V. I. Tatarskii, A. Ishimaru, and V. U. Zavorotny, SPIE, pp.50–83, 1993.

[46] O. I. Yakovlev, A. I. Efimov, V. M. Razmanov, and V. K. Shtrykov, Inhomogeneous structure and velocity of the circumsolar plasma based on data of the Venera-10 station, *Soviet Astronomy*, **24**, pp.454–459, 1980.

[47] L. T. Little, and A. Hewish, Radio source structure derived from interplanetary scintillation, *Monthly Notices of Royal Astronomical Society*, **138**, pp.393–406, 1968.

[48] G. R. Gapper, A. Hewish, A. Purvis, and P. J. Duffett-Smith, Observing interplanetary disturbances from the ground, *Nature*, **296**, pp.633–636, 1982.

[49] K. Asai, Y. Ishida, M. Kojima, K. Maruyama, H. Misawa, and N. Yoshimi, Multi-station system for solar wind observation using the interplanetary scintillation method, *Journal of Geomagnetism and Geoelectricity*, **47**, pp.1107–1112, 1995.

[50] S. L. Scott, W. A. Coles, and Bourgois, Solar wind observations near the Sun using interplanetary scintillation, *Astronomy and Astrophysics*, **123**, pp.207–215, 1983.

# Chapter 2

# UHF Radio Telescope

Study of global structure of the solar wind requires the solar wind measurements with adequate spatial and temporal resolution. For the requirement, the radio telescope dedicated to the IPS observation needs to have high sensitivity so that one can observe a large number of compact radio sources. The IPS observations using the four-station system have been made since the last station was built at Kiso in 1993. The Kiso radio telescope (Figure 2.1) has included several new techniques for design of the primary feed system [1] and calibration system [2] as described in the following Chapters. We mainly describe the system of the Kiso radio telescope whose system design is basically the same as the others.

## 2.1 Configuration of the Radio Telescope

The radio telescope consists of an antenna system, a receiver system, and a computer system, illustrated in Figure 2.2. The antenna acts as a collector of radio waves from a distant celestial source. If an aperture of the antenna is larger and the sensitivity increases, it can collect more power of radio waves. The half-power beam width of an aperture antenna $\theta_h$ [rad] is given by [3, 4]

$$\theta_h = \lambda / D, \tag{2.1}$$

where $\lambda$ is wavelength and $D$ is aperture width of the antenna. That is, the shorter wavelength and larger aperture width can provide better spatial resolution. However, higher surface accuracy of a parabolic reflector is required at the shorter wavelength. We

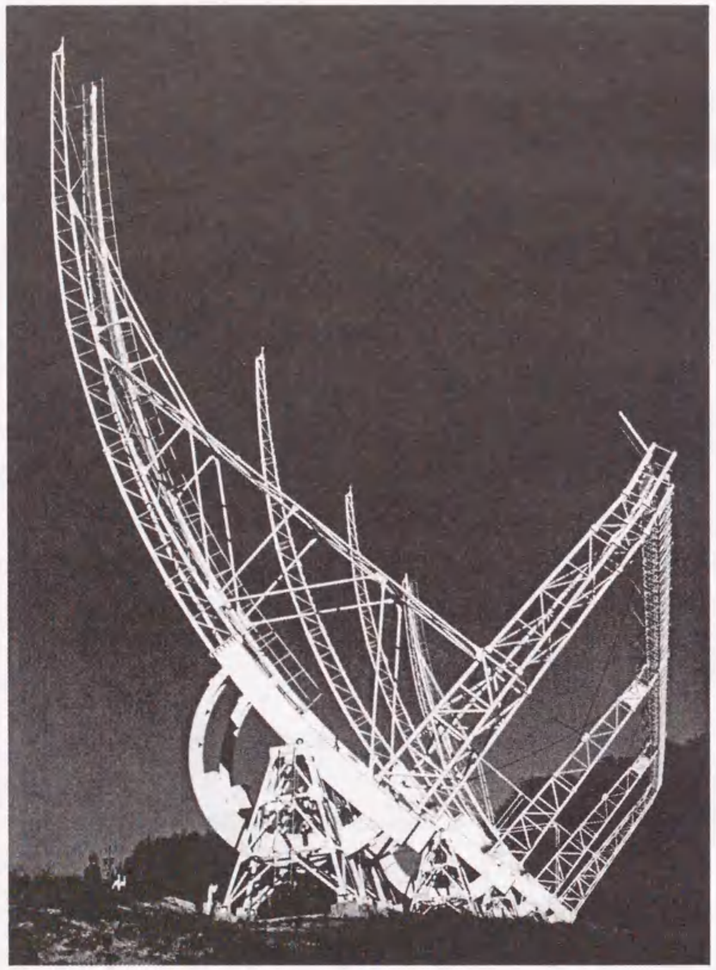

Figure 2.1: Panoramic view of the antenna at the Kiso station.



use a UHF band as a receiving frequency, so our radio telescopes posses wires for the main and sub reflector and a dipole array for the feed system .

The receiver system is comprised of a front-end and a back-end, which amplifies and detects the collected radio waves. The front-end (pre-amplifier) located near the antenna focus amplifies the faint radio signal, converts a frequency from RF to IF, and then transfers the signal to the back-end without reducing signal to noise ratio. In the back-end, the signal from the front-end is amplified again and square-law detected. This receiver system is called the superheterodyne receiver which is the most common type for radio science and engineering. In the superheterodyne receiver, the main amplification is set at a stage after the frequency conversion of the mixer as shown in Figure 2.2, and the RF center frequency is determined by a local oscillator frequency and the band-pass filter. In the Kiso system, the RF signals are down-converted to IF signal in the pre-amplifier unit, and then combined to one signal.

A computer system acquires the digital signal converted from the analog signal and makes signal integration, calibration, and analysis. The computer system also controls an antenna drive system for the radio source tracking and the receiver system for circuit-switching.

## 2.2 Antenna System

The shape of the antenna is an asymmetric parabolic cylinder (Figure 2.3) which has the advantages of easy maintenance of the primary feed system and good cost-performance. High sensitivity requires a large physical collecting area of the antenna. To satisfy this requirement, we select this kind of antenna shape, though the feed system is a little complicated. The parabolic cylinder antenna has been used for radio astronomy. The 178 MHz aperture-synthesis interferometer radio telescope at Cambridge University (England) has a tiltable cylindrical parabolic reflector which is 442 m long (East-West) by 20 m wide. In this telescope, a smaller, movable section is mounted on tracks to move 300 m in the north-south direction for aperture synthesis observations [5]. The 326.5 MHz radio telescope was built in 1970's at Ootacamund (India), having a parabolic cylinder reflector

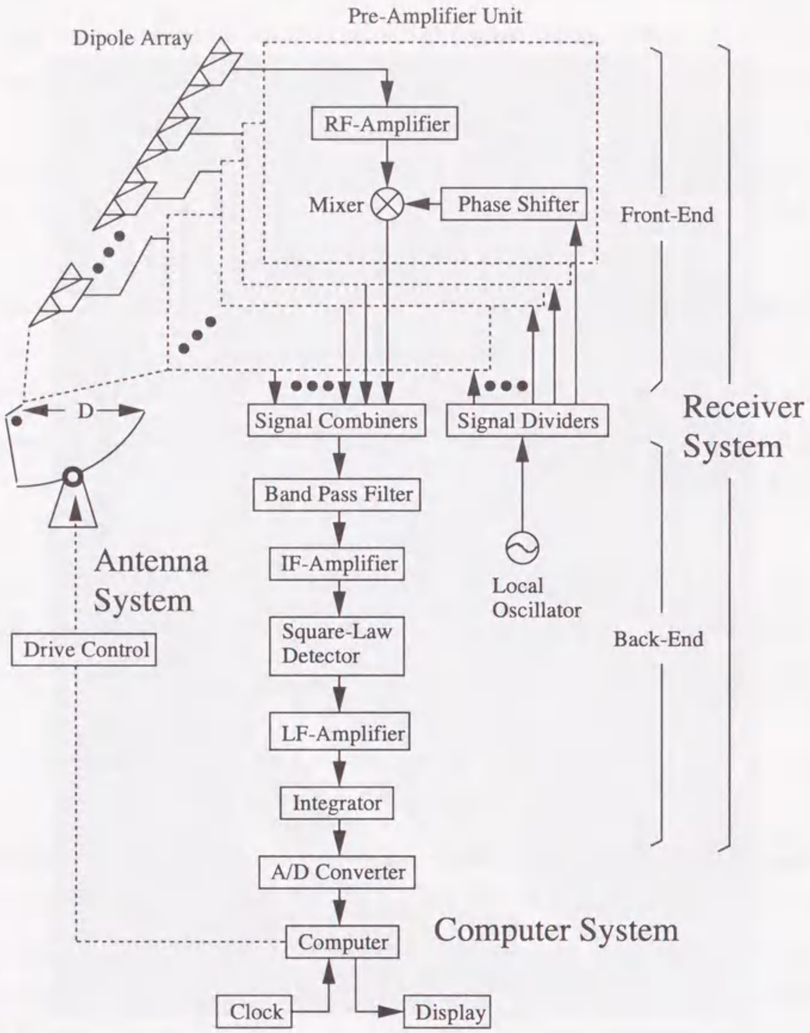


Figure 2.2: Configuration of radio telescope. The radio telescope consists of an antenna system, a receiver system, and a computer system. The antenna system has an asymmetric parabolic cylinder antenna and a phased array system with a corner reflector. The receiver system has the front-end and the back-end. The computer system controls data acquisition, calibration, and antenna drive.



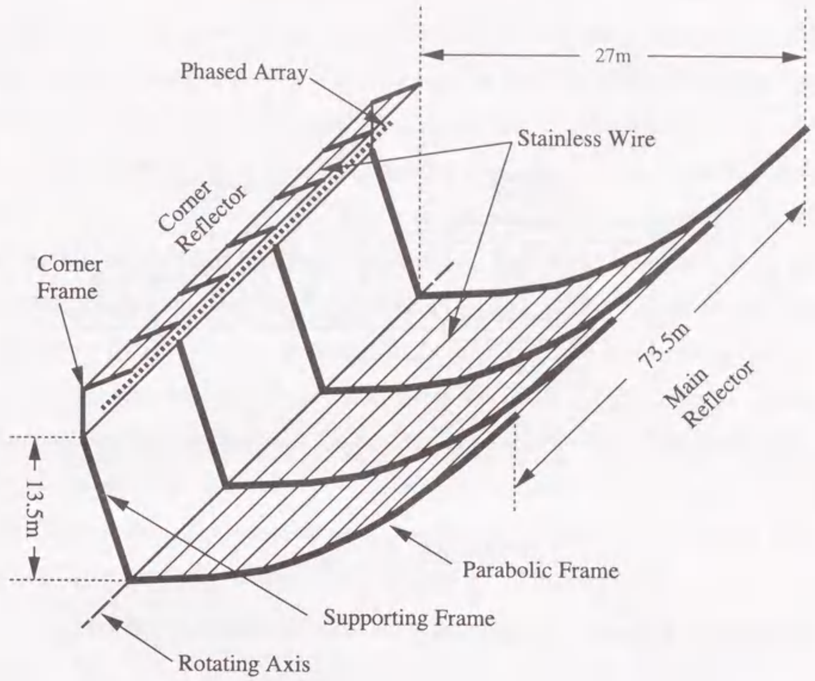


Figure 2.3: Configuration of the asymmetric parabolic cylinder antenna. The antenna consists of four parabolic frames in the east-west direction, with stainless steel wires stretched through the frames to make a $73.5 \times 27$ m$^2$ parabolic reflector.

with 530 m long in north-south and 30 m wide in east-west direction [6]. This radio telescope has been employed to measure a lunar occultation, interplanetary scintillation, etc. EISCAT (European Incoherent SCATter) have operated the VHF and UHF radar. The VHF radar [7] uses a 40 m by 120 m parabolic cylinder antenna which is mechanically steerable in the geographic meridian plane. The radars make measurements of the Earth's ionosphere and its interactions with the upper atmosphere, the magnetosphere and the interplanetary medium.

Our parabolic cylinder antenna is composed of a main parabolic reflector, a corner reflector, and a phased array system. This cylinder antenna has a rotating axis

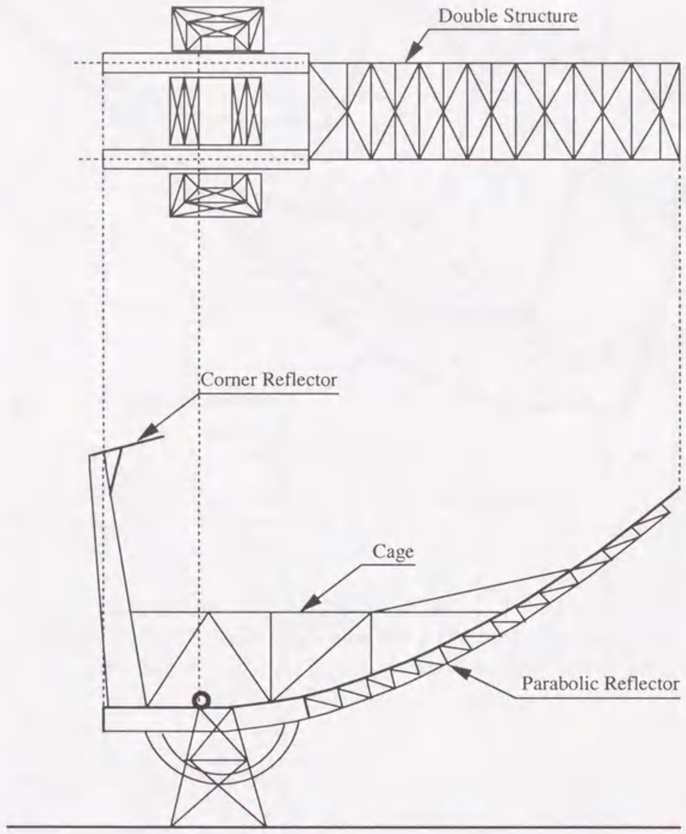


Figure 2.4: Cross section of the parabolic edge frame. The offset parabola is introduced to avoid blockage loss by the corner reflector.



in the east-west direction. Tracking of a radio source is done by mechanical rotation of the parabolic frames in the elevation direction and by electrical beam scanning with the phased array in the azimuth direction. The steering range in the transit plane with the mechanical rotation is 20° north to 75° south of the zenith. The tracking range with the phased array is about ±2 hours of the transit plane. The aperture width in the north-south direction is 27 m, the cylinder length in the east-west direction is 73.5 m, and the focal length of the parabola is 13.5 m. The surface of the main reflector is made up of more than 1000 thin stainless steel wires stretched at an interval of 3 cm and is supported by four parabolic frames placed at 24.5 m apart from one another in the east-west direction. The corner reflector is also made up of stainless wires, but the wire interval is 2 cm and the supporting frame interval is 6.125 m in order to improve the surface accuracy. The radio wave signals reflected from the main reflector are received by a dipole-array with a 120° corner reflector. The dipole-array consists of 144 half-wave dipoles placed along the focal line of the parabolic cylinder, and is phased by 72 phase shifters.

Actually, the antenna size of the Kiso telescope is different from those at the other sites, though the physical collecting area is almost the same. The other antennas except Kiso have a 20 m aperture width, a 100 m cylinder length, and a 10 m focal length. Thus the parabolic frames of Kiso antenna are longer than those of the others. It causes a strong strain to the both edge frames due to total tension of around 1000 stainless steel wires. Therefore, the parabolic frame at the both edges is doubled-structured. But the long frame and doubled-structure induce a bending due to the deadweight of the frames. Hence, cages are added to the both edge frames, and wires inside-frames. The cross section of the edge frame is illustrated in Figure 2.4. The antenna is an offset parabola to avoid blockage loss by the large corner reflector.

## 2.3 Feed System

A phased array is installed in the primary feed system of the asymmetric parabolic cylinder antenna, as shown in Figure 2.2. Phase, gain, and calibration switches in the primary feed system are controlled through optical fibers for a counterplan to thunderbolt. The phased

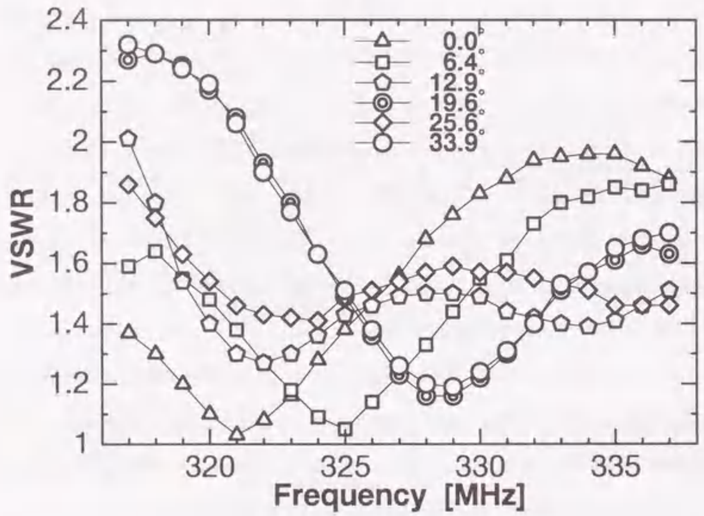


Figure 2.5: VSWR of center elements in the five dipole array with a corner reflector. The marks denote the tilted angle of the main beam, phasing the dipole-elements.

array consists of 144 half-wave dipoles, 72 pre-amplifier units including phase shifters, and signal combiners (gathering network) to combine signals. Each half-wave dipole spaced 0.56 wavelength apart is connected to a balun, and the impedance is matched to the line impedance by tuning a stub line at a center frequency of 327 MHz. Actually, the mutual impedance between array-elements varies with scanning the beam, and the VSWR then changes at the feeding point. Figure 2.5 shows input VSWR of the center element in the condition that five dipole-elements with a corner reflector is fed RF power. The marks denote tilted angles of the main beam. The average VSWRs in the frequency range of 317 to 337 MHz are 1.5 to 1.7 for the beam angle between 0° and 33.9°.

A new calibration system was introduced in the Kiso radio telescope. The calibration system adjusts the phase and gain of each array-element properly, so that the beam of the antenna is formed with the maximum available gain and the minimum possible sidelobe levels. The minimum control angle with the phase shifter is 11.25° and



the minimum control gain with the variable attenuator is 0.2 dB. The calibration system can keep the phase errors less than ±2° and the amplitude errors less than ±0.1 dB for all the array-elements using a loop-method [2] described in detail in Chapter 4.

## 2.4 Receiver System

A block diagram of the receiver system is shown in Figure 2.6 for the front-end system and in Figure 2.7 for IF and LF sections. Adjacent two dipoles in the dipole-array are connected to the pre-amplifier unit where a received signal is amplified at a radio-frequency (RF: 327 MHz), and then down-converted to an intermediate frequency (IF: 70 MHz) with a mixer. The phase of the IF signal is controlled with a phase shifter located in the local-oscillator branch. The IF signal is then amplified again, and reaches the terminal of the preamplifier unit. The output signals from the preamplifier units are combined into one signal with signal combiners and transferred to an observation room through a coaxial cable. This IF signal is introduced into a square-law-detector after passing through amplifiers and a band-pass filter. The bandwidth of the band-pass filter is variable up to 10 MHz so that the receiver may get the maximum IPS power without the saturation, because the coherent bandwidth becomes narrow when the radio wave goes into a strong scattering region near the Sun. The characteristic of the 5 MHz band-pass filter is shown in Figure 2.8. The low-frequency signal out of the square-law-detector is amplified again, integrated with a time constant of 200 ms and digitized with a 13-bit A/D converter. The over-sampled A/D converter is used so that aliasing noise is digital-filtered.

When the phased array tracks a radio source, power gain of the phased array system changes. This is a serious problem for the IPS observations. The gain change is caused by gain variation in controlling the phase shifters. To reduce the gain variation, 5-bit phase shifters are tuned carefully and double-balanced mixers (DBMs) are used. The DBM compresses the IF gain variation due to the phase shifter installed into the local oscillator branch. The characteristics of a pre-amplifier unit with the 5-bit phase shifter and DBM are shown in Figure 2.9. The phase shifting makes amplitude variation of 0.018 dB(rms) and phase error of 0.384°(rms).

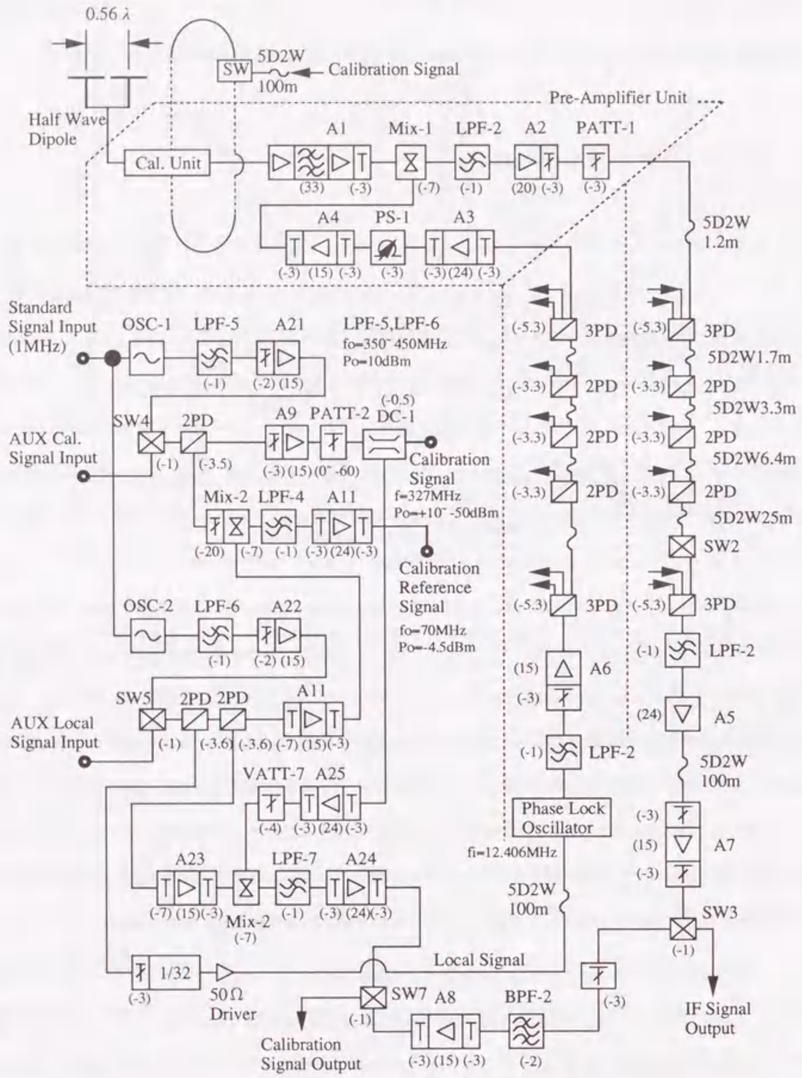


Figure 2.6: Block diagram of the receiver system at the front-end. The phased array consists of 144 half-wave dipole-antennas, 72 phase shifters, and signal combiners(gathering network). The phase shifter is controlled through the optical fiber.



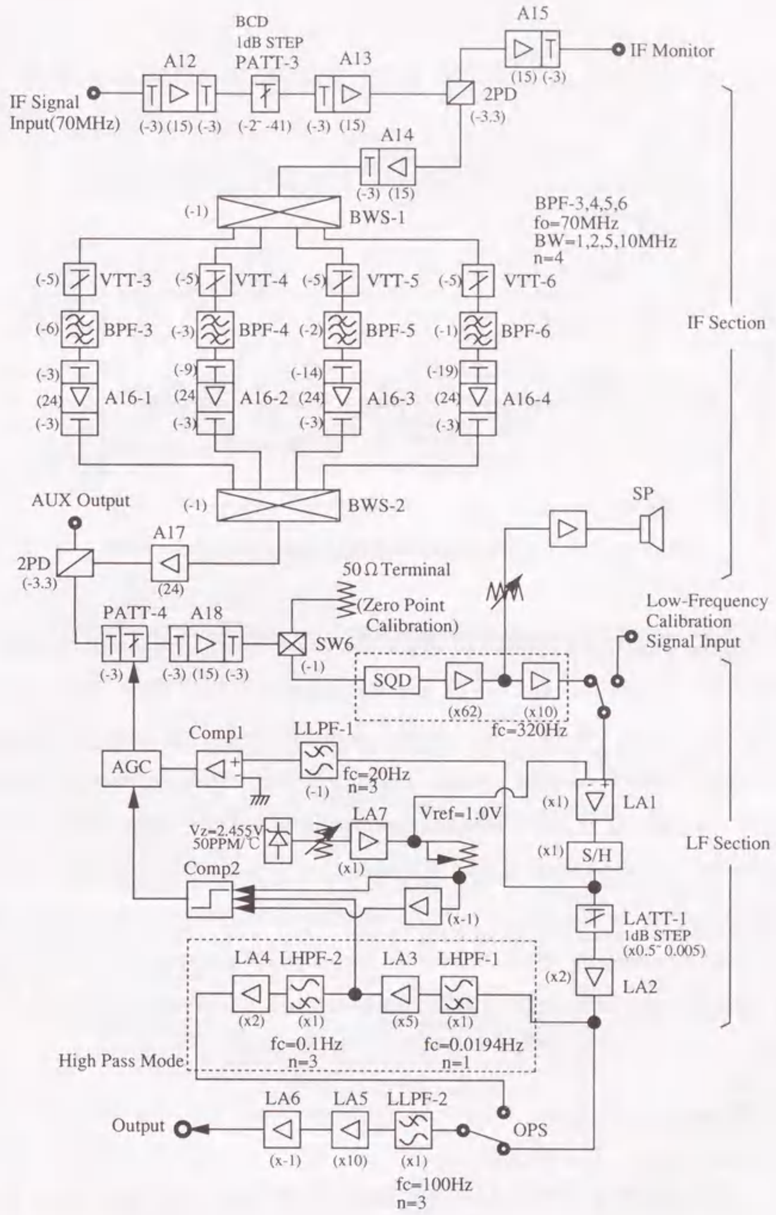


Figure 2.7: Block diagram of the receiver system at the back-end. The IF stage has four band-pass filters (bandwidth: 1, 2, 5, and 10 MHz) to be selected. The LF section after the SQD has two modes: high-pass mode and non high-pass mode.

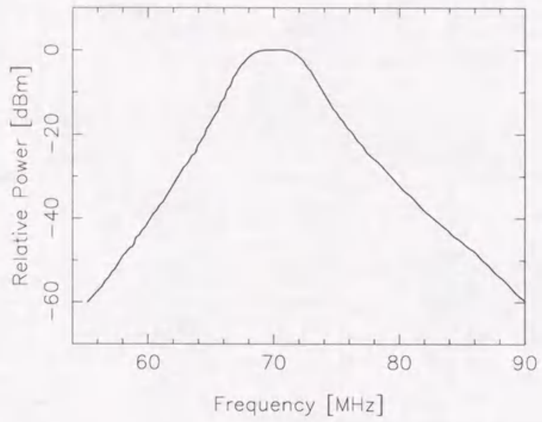


Figure 2.8: Characteristic of the 5 MHz band-pass filter.

The detection is conducted with a non-linear circuit. We install the square law detector (SQD) which uses the square characteristics of a FET (field effect transistor). After the SQD stage, we have two modes: high-pass mode and non-high-pass mode. The high-pass mode is used to measure the scintillating signal by filtering out the low frequency components affected by ionospheric scintillation and interstellar scintillation. While, the non-high-pass mode is used to measure absolute intensity of a radio source. We can select the mode with a switch (OPS). Source tracking makes tracking noise which is spikes caused by switching phase shifters. To keep a power level constant in the high-pass mode, the automatic gain control (AGC) works through a feedback loop.

## 2.5 Sensitivity

### 2.5.1 Minimum Detectable Flux Density

The sensitivity of a radio telescope is limited by fluctuations of the receiver output caused by white noise involving receiver system noise, sky-background noise, and so on. The



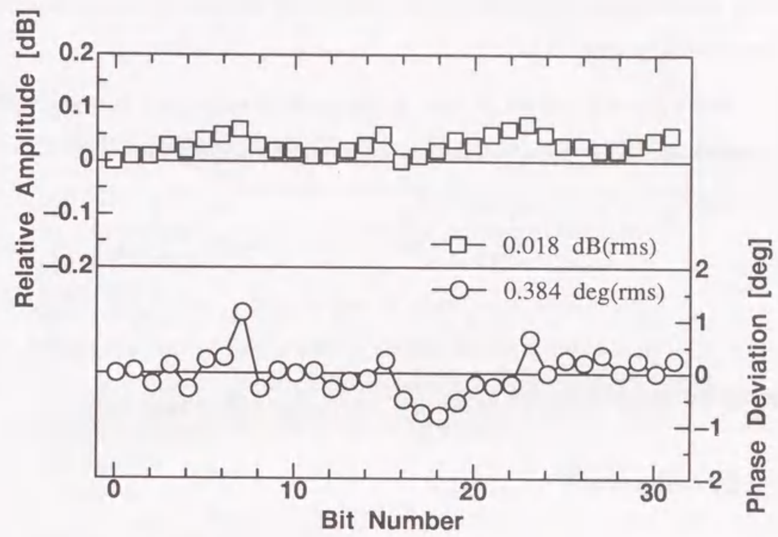


Figure 2.9: Amplitude variation and phase deviation of a pre-amplifier unit in shifting phase.

minimum detectable flux density $\Delta S_{min}$ of a radio telescope is defined as [3]

$$\Delta S_{min} = \frac{2kT_{sys}}{A_e\sqrt{\tau B_{IF}}} \quad [\mathrm{W \cdot m^{-2} \cdot Hz^{-1}}]. \tag{2.2}$$

Here, $k$ is a Boltzmann's constant (=$1.38\times10^{-23}$ J K$^{-1}$), $T_{sys}$ system noise temperature, $A_e$ effective aperture of antenna, $B_{IF}$ predetection bandwidth, $\tau$ postdetection integration time. $T_{sys}$ is expressed as

$$T_{sys} = T_A + (L_0 - 1)T_L + L_0T_R, \tag{2.3}$$

where $T_A$ is antenna noise temperature, $T_L$ physical temperature of transmission line (coaxial cable) between antenna and receiver, $T_R$ receiver noise temperature, and $L_0$ resistive losses in the feed. $T_A$ involves noise temperature due to sky background radiation and ground radiation. $T_R$ is given as

$$T_R = (N_f - 1)T_P, \tag{2.4}$$

where $N_f$ is noise figure of the receiver, and $T_P$ physical temperature of the receiver. $T_L$ and $T_P$ are approximately the same as the surrounding atmosphere temperature in our case of no cooling system.

Noise figure is defined as ratio of the signal to noise ratio between input and output. In the multistage amplifier, the total noise figure is given by

$$N_f = N_{f1} + \frac{N_{f2}-1}{G_1} + \frac{N_{f3}-1}{G_1 G_2} + \cdots + \frac{N_{fn}-1}{G_1 G_2 \cdots G_{n-1}}, \tag{2.5}$$

where $N_{fm}(m = 1,2,\cdots,n)$ is noise figure of each amplifier, and $G_m(m = 1,2,\cdots,n)$ is power gain. That is, the ability of the receiver is determined by the preamplifier. Hence, the preamplifier should make low noise.

### 2.5.2 Performance

The primary feed system in the Kiso radio telescope was designed to make an optimum illumination distribution on the parabola aperture with least spillover, providing high illumination efficiency. The main and corner reflector were also designed to optimize the surface accuracy under the structural and economic restrictions. The effective collecting area was then obtained to be 1409 $m^2$ from measurement of a natural radio source, which corresponds to the aperture efficiency of 71 %.

The low noise receiver system is necessary for measuring very faint radio intensity variations of the IPS, because the power level of the instrumental noise is comparable with that of sky-background noise encountered at a frequency of 327 MHz. The preamplifier has low noise figure of less than 1.61 dB at 327 MHz with a bandwidth of 20 MHz at temperature of 20°C. The total system temperature of 221 K has been achieved, including the antenna temperature of 70 K due to sky background radiation and ground radiation entering the feed from the spillover, the resistive losses of 0.21 dB in the feed, and the receiver temperature derived from the mean noise figure of 1.61 dB. Consequently the minimum detectable flux density is estimated to be 0.43 Jy (1 Jy = $10^{-26}$ W$\cdot$ $m^{-2}\cdot Hz^{-1}$), assuming a bandwidth of 10 MHz and an integration time of 100 ms. Table 2.1 summarizes the specifications and performance of the Kiso radio telescope.



Table 2.1: Specifications and performance of the Kiso radio telescope.

| | |
|---|---|
| Antenna : | Asymmetric cylindrical parabola |
| Aperture width : | 27 m (North-South) |
| Cylinder length : | 73.5 m (East-West) |
| Focal length : | 13.5 m |
| Steering range of transit plane : | 20° North to 75° South of zenith |
| Feed : | 144 dipole array<br>(with a 120° corner reflector) |
| Tracking range : | ± 1 hour of transit plane |
| Center frequency : | 327 MHz |
| Bandwidth : | 1 ∼ 10 MHz, variable |
| Calibration system : | phase error < ± 2°<br>amplitude error < ± 0.1 dB |
| Feed loss : | 0.21 dB |
| Noise figure : | 1.61 dB |
| System noise temperature : | 221 K |
| Effective collecting area : | 1409 $m^2$ |
| Time constant : | 100 ms |
| Minimum detectable flux density : | 0.43 Jy |

Notes :

a) The total system temperature is expected from a sum of the antenna temperature, resistive losses in the feed, and the receiver temperature. The receiver temperature is derived from a measurement of the noise figure of the preamplifier unit.

b) The antenna temperature is predicted to be 70 K due to: 1)sky background radiation away from the galactic plane for 327 MHz and 2)ground radiation entering the feed due to the spillover.

c) The effective collecting area is deduced from the aperture efficiency which is a product of the following four effects: 1)aperture illumination, 2)spillover, 3)blockage, 4)surface accuracy of the wired reflectors.

d) The minimum detectable flux density expressed in Jansky (1 Jansky (Jy) = $10^{-26}$ W$\cdot m^{-2}\cdot Hz^{-1}$) was determined by measuring the radio source 3C274.

## 2.6 Upgrade Project

The fact that the Kiso radio telescope realized the predicted sensitivity, has proved that the design method of the primary feed system is successful for maximizing illumination efficiency. The upgrade project [9] was then conducted for the other telescopes of Fuji, Sugadaira, and Toyokawa stations, which were improved in the primary feed system and the receiver system.

Although the physical collecting area of the Fuji antenna has not been changed in this improvement, high aperture efficiency was achieved by optimizing the primary feed system with the same design method which was employed for the Kiso antenna [1]. The primary feed system with the optimum illumination distribution on the aperture provided the maximum illumination efficiency of 89.5 %. The reflection efficiency based on the losses with respect to surface accuracy of the reflectors is 84.5 %. Including blockage loss by a support of the feed system (blockage efficiency : 91.5 %), the total aperture efficiency is estimated to be 69.2 %. The feed structures of the Sugadaira and Toyokawa antennas were not changed.

We have developed a pre-amplifier using a GaAsFET, which was designed to have extremely low noise at room temperature. The input impedance to maximize the gain is not generally the same as that to minimize the noise. So we optimized a source lead inductance to obtain both of an impedance match and a low noise figure simultaneously, which reduces a difference between these two impedances [10, 11]. For the Fuji lots, the preamplifier achieved the noise figure of less than 0.87 dB at 327 MHz with the bandwidth of 20 MHz at a temperature of 25°C. We obtained 0.75 dB for the Sugadaira lots and 0.65 dB for the Toyokawa lots under the same condition. Although the circuit design was almost the same among the Fuji, Sugadaira and Toyokawa lots, the latter two were tuned well. The circuit design of the pre-amplifier of the Toyokawa lot is displayed in Figure 2.10, and the characteristics are summarized in Table 2.2. In addition to the low noise preamplifiers, the loss in the feed system is decreased using a low loss matching circuit.



Table 2.2: Average characteristics of the pre-amplifiers in the Toyokawa lot.

| | |
|---|---|
| Center frequency | 327 MHz |
| Total gain | 30± 0.5 dB |
| Bandwidth (3 dB down) | 20± 1 MHz |
| Image reduction | 45 dB at $f$=467 MHz |
| Input return loss | 17 dB at $f_0 = \pm 10$ MHz |
| | 19 dB at $f_0 = \pm 5$ MHz |
| Output return loss | 13 dB at $f_0 = \pm 10$ MHz |
| | 16 dB at $f_0 = \pm 5$ MHz |
| Noise Figure (average) | 0.65 dB at 22°C |
| Temperature dependence of NF | 0.65±0.03 dB at $T_0$ between 0 and 50°C |

The minimum detectable flux density was measured by observing the calibration source 3C274 (605 Jy at 327 MHz) with the same bandwidth and time constant as those used for the Kiso radio telescope. Figure 2.11 shows the comparison of the sensitivity of the Fuji system before and after the improvement. These two patterns were obtained from the observations of 3C274 with a fixed beam. The solid line is the pattern after the improvement and the dashed line is before the improvement. The intensity level below zero corresponds to the relative system temperature referred to the intensity of 3C274. The difference between the two levels at a direction of zero degree is proportional to the difference of the sensitivities. The Fuji system after the improvement is nearly five times more sensitive than the previous system. This is consistent with the sensitivity expected from a 12 % increase in the effective area and a 70 % reduction in the system noise. Table 2.3 lists characteristics with respect to sensitivity of the radio telescope at each station.

Table 2.3: Sensitivity of the radio telescope system at each station under the conditions: $B_{IF}$=10 MHz, $\tau$=100 ms, $T_A$: 70 K, $T_P$: 290 K.

| Station | $L_0$ [dB] | $N_f$ [dB] | $T_{sys}$ [K] | $A_e$ [m$^2$] | $\Delta S_{min}$ |
|---|---|---|---|---|---|
| Toyokawa | 2.16 | 0.65 | 334 | 1013 | 0.91 |
| Fuji | 0.21 | 0.87 | 151 | 1500 | 0.28 |
| Sugadaira | 1.15 | 0.75 | 229 | 1120 | 0.58 |
| Kiso | 0.21 | 1.61 | 221 | 1409 | 0.43 |

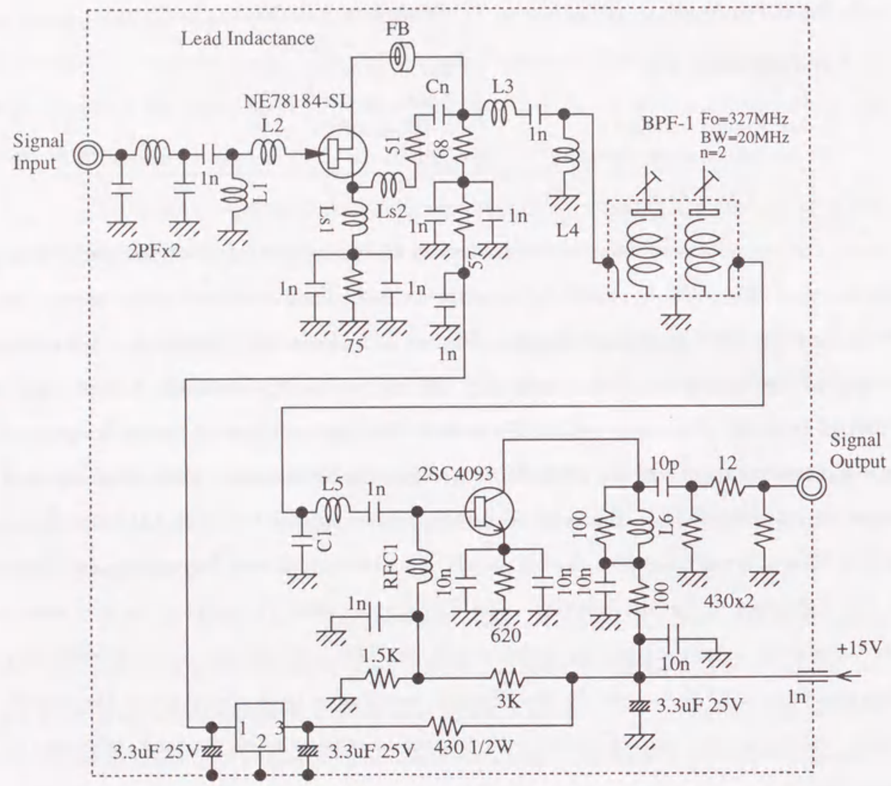


Figure 2.10: Circuit design of a low noise amplifier (LNA) employed as the pre-amplifier of Toyokawa station. The LNA has two amplifying stages: GaAs FET(NE78184-SL) stage and Si(2SC4093) stage. In the GaAs FET stage, Ls1 is a source lead inductance and L2 dominates the input return loss.



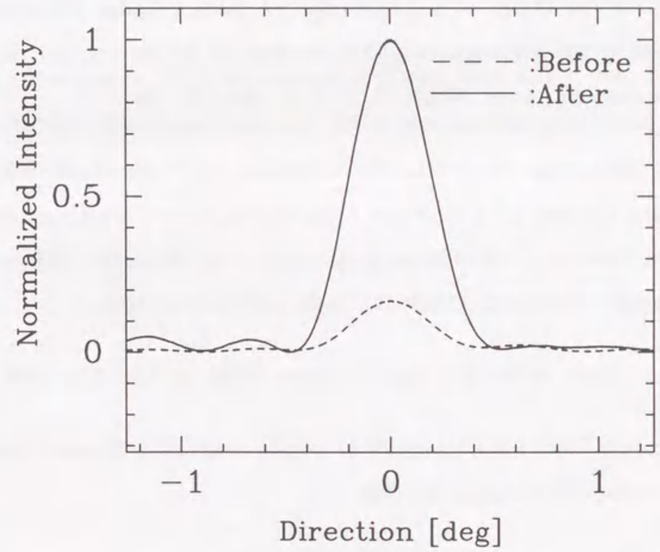


Figure 2.11: Comparison of sensitivity of the Fuji antenna before and after system improvement. These are the detector outputs of the antenna when the radio source of 3C144 made transit through an antenna-beam.

# Bibliography


[1] K. Asai, M. Kojima, H. Misawa, Y. Ishida, K. Maruyama, N. Yoshimi, M. Wakasa, and M. Karakida, Design of an asymmetric parabolic cylinder antenna with high aperture efficiency, *Transactions of the Institute of Electronics, Information and Communication Engineers*, **J78-B-II**, No.3, pp.102–109, 1995.

[2] K. Asai, M. Kojima, Y. Ishida, K. Maruyama, N. Yoshimi, H. Misawa, and K. Miyasato, Calibration of Gain and Phase on the Phased Array System Installed in a Radio Telescope, *Transactions of the Institute of Electronics, Information and Communication Engineers*, **J79-B-II**, No.12, pp.994–1002, 1996.

[3] J. D. Kraus, Radio Astronomy, *Cygnus-Quasar Books*, pp.3.43–3.45, 1986.

[4] The Institute of Electronics, Information and Communication Engineers (ed.), *Handbook of antenna technology*, Ohm, 1980.

[5] M. Ryle, and A. Hewish, The synthesis of large radio telescope, *Monthly Notices of the Royal Astronomical Society*, **120**, pp.220–230, 1960.

[6] G. S. Swarup, N. V. G. Sarma, M. N. Jashi, V. K. Kapahi, D. S. Bagri, S. H. Damle, S. Ananthakrishnan, V. Balasubramanian, S. S. Bhave, and R. P. Sinha, Large steerable radio telescope at Ootacamund, India, *Nature Physical Science*, **230**, pp.185–188, 1971.

[7] T. Hagfors, P. S. Kildal, H. J. Kärcher, B. Liesenkötter, and G. Schröer, VHF parabolic cylinder antenna for incoherent scatter radar research, *Radio Science*, **17**, No.6, pp.1607–1621, 1982.







[8] M. Morimoto, and N. R. Labrum, The phase and gain calibration system, *Proceedings of the Institute of Radio and Electronics Engineers Australia*, **28**, No.9, pp.352–360, 1967.

[9] K. Asai, Y. Ishida, M. Kojima, K. Maruyama, H. Misawa, and N. Yoshimi, Multi-station system for solar wind observation using the interplanetary scintillation method, *Journal of Geomagnetism and Geoelectricity*, Vol.47, pp.1107–1112, 1995.

[10] D. R. Williams, W. Lum, and S. Weinreb, L-band cryogenically cooled GaAs FET amplifier, *Microwave Journal*, **28**, pp73–76, 1980.

[11] A. J. Selvanayagam, A. Praveenkumar, D. Nandagopal, and T. Velusamy, Sensitivity boost to the Ooty Radio Telescope: A new phased array of 1056 dipoles with 1056 low noise amplifiers, *IETE Technical Review*, **10**, No.4, pp.333–339, 1993.

# Chapter 3

# Design of Asymmetric Parabolic Cylinder Antenna

## 3.1 Aperture Efficiency of Parabolic Antenna

The forth radio telescope for interplanetary scintillation observations was constructed at the Kiso station in 1993. The radio telescope has an asymmetric parabolic cylinder antenna with a large aperture area at a frequency of UHF band. High receiving sensitivity requires high aperture efficiency as well as the large physical collecting area of the antenna. The antenna is then designed to increase the aperture efficiency by optimizing the primary feed system [1]. In this optimum design the beam shape or sidelobe suppression are disregarded, because the main objective is not to investigate the radio source configuration but to detect an infinitesimal intensity fluctuations of the weak celestial radio wave. There are several attempts to make aperture efficiency high in regard to the asymmetric parabolic cylinder antenna. In the Ooty radio telescope, for example, an experimental design of the primary feed was made by measuring the primary radiation patterns [2]. In the EISCAT (European Incoherent Scatter Association), the primary feed is designed to provide equal radiation patterns for the transverse and longitudinal polarizations, and the F/D ratio of the parabola is optimized to increase the aperture efficiency [3].

In the case of the parabolic antenna, the aperture efficiency $\eta$ is mainly determined by leakage from the parabolic reflector surface $\eta_s$, illumination characteristics based on the amplitude and phase distributions on the aperture $\eta_i$, reflector surface tolerance





$\eta_r$, and blocking effect due to the subreflector and supporting frames $\eta_b$ [4],

$$\eta = \eta_s \eta_i \eta_r \eta_b. \tag{3.1}$$

The uniform illumination distribution on the aperture yields high efficiency of $\eta_i$, but it might be impossible actually. When the illumination level is increased at the edge of the parabolic reflector, the spillover necessarily increases. Hence, there exists an optimum illumination pattern on the parabolic reflector [4]. We here treat $\eta_s$ and $\eta_i$ as "illumination efficiency" based on the illumination distribution on the aperture against its spillover. In this asymmetric parabolic cylinder antenna, there is no blocking effect of the primary feed system because of the offset parabola. So, Equation 3.1 is reduced to the product of the illumination efficiency and reflection efficiency based on the reflector surface tolerance.

The primary feed is made up of a dipole-array with a corner reflector and has structure parameters dominant for its configuration. First, the relationship is examined between the illumination efficiency and the structure parameters to find the optimum design of the primary feed. Next, the method is discussed to increase the reflection efficiency under the restricted conditions for the main and corner reflectors. Finally, the design methods are verified with measurement of the aperture efficiency.

## 3.2 Antenna Configuration and Structure Parameters

Figure 3.1 shows a schematic configuration of the asymmetric parabolic cylinder antenna, which was described in detail in Chapter 2. The $x$ axis is parallel to the line connecting the parabola focus to the parabola origin and $z$ axis is along the focal line of the parabolic cylinder. The parabola reflector is formed by stretching the stainless wires among the supporting parabolic frames. The corner reflector is also formed in the same way as the parabola reflector. Each stainless wire is stretched by a spring. The interval and tension of the stainless wires are important factors for the reflection efficiency. The stainless wires are placed only along the east-west direction, so single polarization of the radio wave is caught. The offset cylindrical parabola is employed to avoid surface blockage by the feeder. The feed system of the antenna is a phased array with the corner reflector.

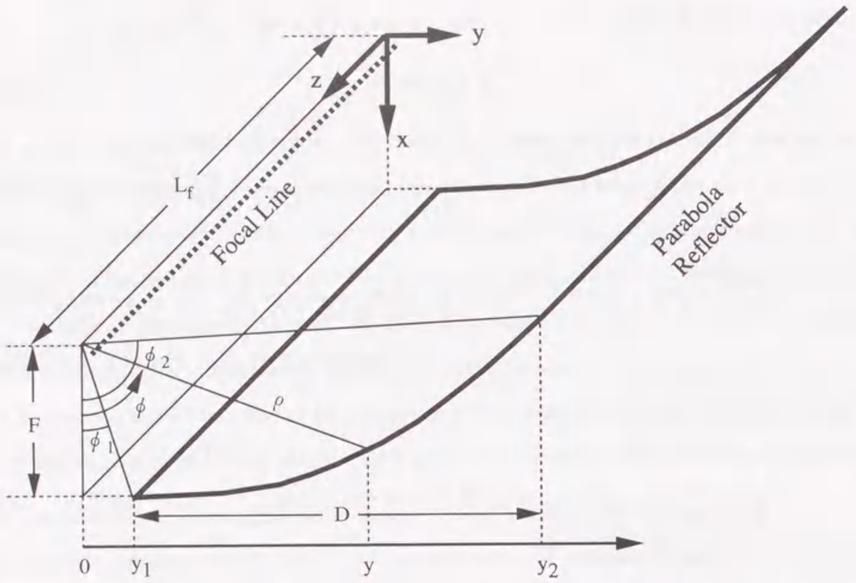


Figure 3.1: Schematic configuration of the asymmetric parabolic cylinder antenna. The parabolic cylinder is shown as an area within heavy lines. The focal line is shown as a heavy dashed line.

Figure 3.2 shows the transverse positional relationship of the corner reflector, dipole-antenna of the primary feed, and the focal point of the main reflector. The structure parameters important for the configuration of the primary feed are the apex angle $\alpha$ of the corner reflector, the distance $s_\lambda$ between the dipole-antenna and the corner apex, and the distance $\rho_0$ between the parabola focus and the corner apex. The optimum values of these parameters are determined for the maximum illumination efficiency, and the derivation method is discussed in the next section.

## 3.3 Illumination Efficiency

The illumination efficiency $\eta_I$ consists of efficiency $\eta_s$ caused by the leakage from the parabola reflector and efficiency $\eta_i$ based on the illumination characteristics (amplitude and phase distributions on the aperture), but the both efficiencies are contradictive each other. There is an optimum value in the illumination distribution over the aperture



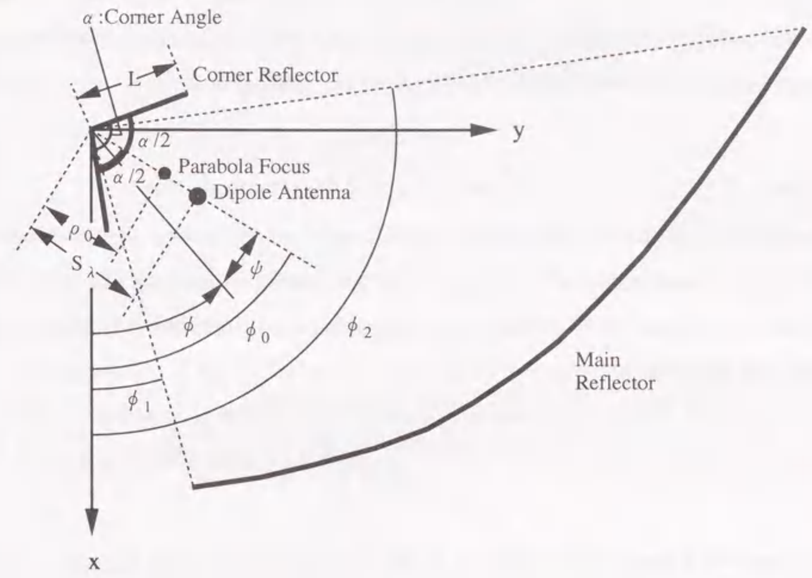


Figure 3.2: Transverse configuration of the primary feed and the main reflector. The parabola is shown as a heavy line. $\phi_0$ is taken to the direction of the dipole antenna which is located on the bisector of the corner angle.

such that the illumination efficiency $\eta_I$ takes the maximum. The primary feed system with a corner reflector is then designed to make an optimum radiation pattern. Here the radiation pattern of the primary feed only in the vertical plane ($x$-$y$ plane) is taken into consideration for the illumination efficiency, and leakage outside the reflector in the cylinder axis is assumed to be negligible.

The parabola reflector with a focal length $F$ is defined by

$$\rho = \frac{F}{\cos^2 \frac{\phi}{2}}. \tag{3.2}$$

If the line feed is assumed to radiate an ideally cylindrical wave, the radiation field in the vertical plane is given by [5]

$$E(\rho) = K \frac{1}{\sqrt{\rho}} G(\phi) \exp(-jk\rho), \tag{3.3}$$

where $K$ is a constant and $G(\phi)$ is the radiation pattern in the vertical plane.

When the parabolic cylinder surface is illuminated by the primary feed, the illumination efficiency $\eta_I$ [3] is defined as ratio of the coherently received radiation power by the reflector to the total radiation power from the primary feed,

$$\eta_I = \frac{\left|\int_{y_1}^{y_2} \frac{G(\phi)}{\sqrt{\rho}} dy\right|^2}{D \int_{-\infty}^{\infty} \frac{|G(\phi)|^2}{\rho} dy}, \tag{3.4}$$

where $D$ is the aperture-width of the parabolic reflector. $y_1$ and $y_2$ are the inner and outer edges of the parabolic reflector, respectively. Since Equation 3.4 is the integral of $y$ in spite of the function of $\phi$ in $G(\phi)$, $y$ is transformed to $\phi$. In Figure 3.1, $y$ is given by, substituting Equation 3.2,

$$y = \rho \sin\phi \tag{3.5}$$

$$= 2F \tan\frac{\phi}{2}. \tag{3.6}$$

Thus, Equation 3.4 reduces to

$$\eta_I = \frac{F}{D} \frac{\left|\int_{\phi_1}^{\phi_2} G(\phi) \frac{1}{\cos(\phi/2)} d\phi\right|^2}{\int_{-\pi}^{\pi} |\, G(\phi)\,|^2\, d\phi}, \tag{3.7}$$

where $\phi_1$ and $\phi_2$ are the inner and outer edge angles of the parabolic reflector.

### 3.3.1 Formula for Radiation Pattern of the Primary Feed

In the coordinate system shown in Figure 3.2, the radiation pattern $G(\phi)$ of the infinitesimal dipole with a corner reflector in the vertical plane [6, 7] is given by

$$G(\phi) = G_f(\phi) e^{jk\rho_0 \cos(\phi_0 - \phi)}, \tag{3.8}$$

where

$$G_f(\phi) = \sum_{n=1}^{\infty} e^{jn\pi u/2} \sin(nu\phi_0) \sin(nu\phi) J_{nu}(ks_\lambda). \tag{3.9}$$

Here $u = \pi/\alpha$. In Equation 3.8 and 3.9, $k$ is the wavenumber, $\alpha$ is the apex angle of the corner reflector, $s_\lambda$ is the distance between the corner apex and the dipole antenna, $\rho_0$ is the distance between the corner apex and the parabola focal point, and $J_{nu}$ is the Bessel function of an order $nu$. Also, $\phi_0$ is the angle of the vector connecting the corner apex and the dipole antenna with respect to $x$ axis, and $\phi$ is the direction of the radiation. The



phase reference point of the radiation from the primary feed with the corner reflector is located at the corner apex in the equation given by E. A. Wolff [7]. To shift the phase reference point to the parabola focal point, the term of $e^{jk\rho_0 \cos(\phi_0 - \phi)}$ is added to the right hand side of Equation 3.9 [8].

The structure parameters $\alpha$, $s_\lambda$ and $\rho_0$ in Equations 3.8 and 3.9 determine the radiation characteristics of the primary feed. So the optimum values for the maximum illumination efficiency can be determined from Equation 3.7. In the analysis, the reflection surface made by stretching the stainless wires is approximated by a totally reflecting metal plate for calculation of the radiation characteristics. It is also assumed that the length $L$ of the corner reflector is infinite and the leakage of the wave radiated from the primary feed at the corner reflector is neglected.

### 3.3.2 Ratio of Focal-Length to Aperture-Width

Dependency of illumination efficiency on structure parameters of the primary feed is shown in Figure 3.3 for various focal length to aperture-width ratio ($F/D$). The top, middle, and bottom panels represent (1) efficiency versus an corner angle with the fixed dipole and parabola-focus position, (ii) efficiency versus dipole position with the fixed corner apex angle and parabola-focus position, and (iii) efficiency versus parabola-focus position with the fixed corner apex angle and dipole position. The characters (a), (b), (c), and (d) denote $F/D$ ratio of 0.3, 0.4, 0.5, and 0.7, respectively. Figure 3.3 (i) indicates that the optimum $\alpha$ at the maximum $\eta_I$ depends on the $F/D$ ratio, and the optimum $\alpha$ decreases as the $F/D$ ratio increases. Figure 3.3 (ii) indicates that $\eta_I$ for $s_\lambda < 0.45\ \lambda_0$ is almost constant, but for $s_\lambda > 0.5\ \lambda_0$ rapidly decreases (where $\lambda_0$ is the wavelength at 327 MHz). Figure 3.3 (iii) indicates that the optimum $\rho_0$ also exists for each $F/D$ ratio. In Figure 3.3 (ii) and (iii), $F/D$ ratio of 0.5 (c) provides the maximum efficiency, which is mainly due to $\alpha = 120°$. The corner apex angle dominates the $F/D$ ratio with the maximum efficiency.

As shown in Figure 3.3 (i), on the other hand, if $\rho_0$ and $s_\lambda$ can be set without restriction, $\alpha$ at the maximum $\eta_I$ depends on the $F/D$ ratio. That is, the flexible setting

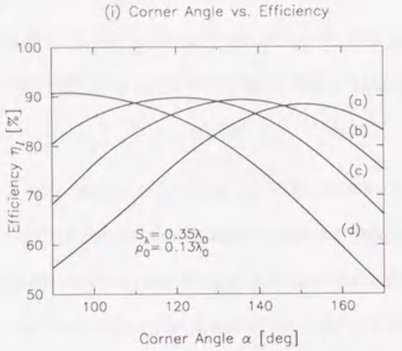


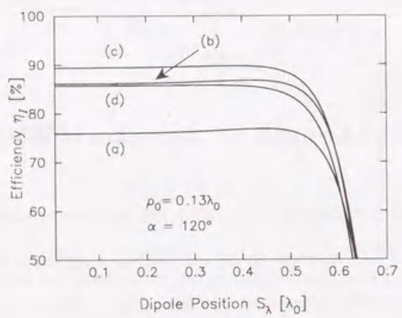


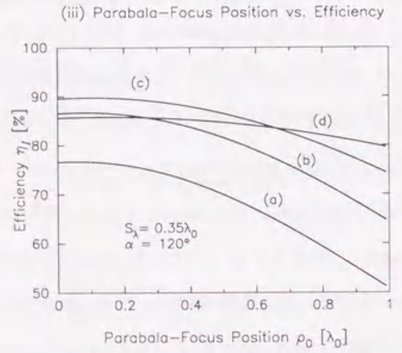


Figure 3.3: Efficiency for varying the structure parameters of the primary feed with variable $F/D$ ratio of the asymmetric parabola: (i) corner apex angle vs. efficiency, (ii) dipole position vs. efficiency, and (iii) parabola-focus position vs. Efficiency. (a), (b), (c), and (d) denote $F/D$ ratio of 0.3, 0.4, 0.5, and 0.7, respectively.



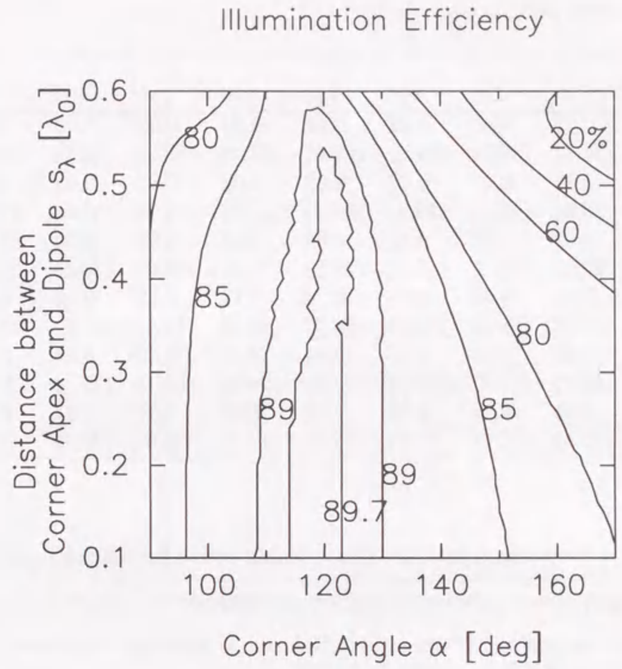


Figure 3.4: Illumination efficiency vs. an apex angle of the corner reflector and a distance between the corner apex and the dipole antenna. The distance $\rho_0$ between the corner apex and the parabola focus is chosen to make the illumination efficiency maximum. The number near contours represents percentage of the illumination efficiency.

of the structure parameters of the primary feed enables to make the illumination efficiency maximum for the parabola antenna with any $F/D$ ratio of 0.3 to 0.7. Here the value of $F/D$ ratio is set at 0.5 from the mechanical restriction of the weight balance.

### 3.3.3 Relationship between Structure Parameters and Illumination Efficiency

In general, if a focal point of the main reflector coincides with the phase center of the primary feed, a radio wave can be received at high efficiency. However, when there

Table 3.1: $\rho_0$ for the combination of $\alpha$ and $s_\lambda$. The value enclosed with a parenthesis is $\eta_I$ [%] in these structure parameters.

| $s_\lambda$ | $\alpha[^\circ]$ | | | | | | | | |
|---|---|---|---|---|---|---|---|---|---|
| $[\lambda_0]$ | 90 | 100 | 110 | 120 | 130 | 140 | 150 | 160 | 170 |
| 0.1 | 0.02 | 0.02 | 0.10 | 0.02 | 0.02 | 0.02 | 0.02 | 0.03 | 0.02 |
| | (81.0) | (86.7) | (89.2) | (89.7) | (89.0) | (87.3) | (85.2) | (82.9) | (80.2) |
| 0.2 | 0.02 | 0.02 | 0.02 | 0.02 | 0.02 | 0.02 | 0.02 | 0.03 | 0.02 |
| | (81.0) | (86.6) | (89.2) | (89.7) | (89.0) | (87.2) | (84.7) | (81.6) | (77.9) |
| 0.3 | 0.02 | 0.02 | 0.02 | 0.02 | 0.03 | 0.04 | 0.04 | 0.03 | 0.02 |
| | (80.9) | (86.4) | (89.0) | (89.7) | (89.0) | (86.8) | (83.0) | (78.0) | (72.0) |
| 0.4 | 0.02 | 0.02 | 0.05 | 0.11 | 0.16 | 0.17 | 0.15 | 0.10 | 0.04 |
| | (80.5) | (85.7) | (88.6) | (89.8) | (88.9) | (85.0) | (77.5) | (67.7) | (56.6) |
| 0.5 | 0.02 | 0.06 | 0.24 | 0.37 | 0.44 | 0.45 | 0.43 | 0.38 | 0.27 |
| | (79.2) | (83.7) | (87.3) | (89.8) | (87.2) | (76.6) | (59.1) | (39.2) | (22.2) |
| 0.6 | 0.02 | 0.33 | 0.77 | 0.98 | 1.12 | 1.32 | 1.67 | 1.97 | 0.05 |
| | (75.4) | (77.5) | (85.0) | (87.6) | (72.6) | (47.7) | (29.0) | (20.2) | (2.9) |

is a corner reflector in the primary feed, the phase center cannot be defined at a point such as at a dipole-antenna. Hence, the distance $\rho_0$ between the corner apex and the parabola focal point is chosen so that the illumination efficiency $\eta_I$ becomes maximum [5]. Note that $\rho_0$ can be uniquely determined once the apex angle $\alpha$ of the corner reflector and the distance $s_\lambda$ between the corner apex and the dipole antenna are given. These structure parameters do not take minus quantity because of a structural limit of the antenna.

Figure 3.4 shows $\alpha$ and $s_\lambda$ versus $\eta_I$. It is clear that there exists $\alpha$ that provides the maximum $\eta_I$ for each $s_\lambda$. It is found that the optimum value of $\alpha$ is around 120°, and there is little difference in $\eta_I$ that reaches 90 %, if $s_\lambda$ is set at less than 0.5 $\lambda_0$. On the other hand, $\eta_I$ is reduced for $s_\lambda > 0.55\ \lambda_0$. This result suggests that there is an upper limit in $s_\lambda$ that provides the maximum $\eta_I$ whereas it is optimum to set $\alpha$ at 120°. The value of $\rho_0$ and $\eta_I$ (enclosed with a parenthesis) for each combination of $\alpha$ and $s_\lambda$ is listed in Table 3.1.

To discuss the relationship between illumination efficiency and structure parameters of the primary feed, we investigate the power level at the edge of the main reflector, and radiation pattern and phase distribution of the primary feed. Figure 3.5 shows the variation of the edge level when $\alpha$ changes for $s_\lambda$ of $0.10\lambda_0$, $0.35\lambda_0$ and $0.60\lambda_0$.



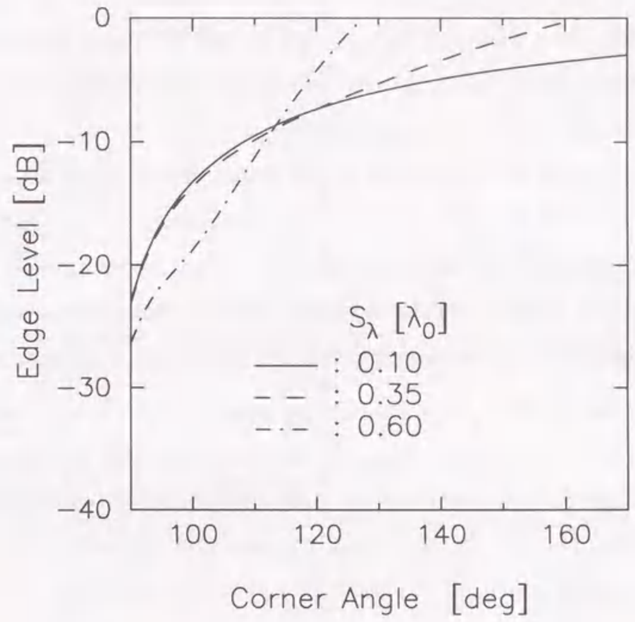


Figure 3.5: Edge level vs. an apex angle of the corner reflector. The edge level is taken as a relative gain level normalized by the main beam level. $\rho_0$ is chosen to make the illumination efficiency maximum.

For each value of $s_\lambda$ the edge level increases with $\alpha$, and the slope of the increment increases with $s_\lambda$. Figure 3.6, 3.7, and 3.8 shows the radiation pattern of the primary feed with a corner reflector and the phase distribution centered at the parabola focal point for $s_\lambda$ of 0.10 $\lambda_0$, 0.35 $\lambda_0$, and 0.60 $\lambda_0$. The horizontal axis $\psi$ is an angle from the direction of the dipole antenna which is set as 0°. Of the four marks on the horizontal axis, the two internal ones indicate the location of the edges of the parabola surface and the two outer ones indicate the corner angle of the corner reflector. From Figure 3.6 and 3.7, the radiation pattern of the primary feed becomes broader with $\alpha$, which is linked to the increase of the edge level shown in Figure 3.5. The phase distribution is almost uniform

regardless of the apex angle of the corner reflector. This uniform distribution implies the optimum positional relationship between the parabolic reflector and the primary feed.

For $s_\lambda$ of 0.10 $\lambda_0$ and 0.35 $\lambda_0$, the edge levels at $\alpha$ of 120° are approximately −7.5 dB which is lower than it is for $s_\lambda$ of 0.6 $\lambda_0$, and the phase distribution on the aperture is almost uniform. While, for $s_\lambda$ of 0.60 $\lambda_0$ the edge level at $\alpha$ of 120° is high and the spillover then increases. The phase variation of roughly 20° occurs even though $\rho_0$ was chosen to maximize efficiency. These are the reason why the maximum $\eta_I$ is obtained at $s_\lambda < 0.5\ \lambda_0$ in Figure 3.4. Since the corner reflector cannot be made infinitely large in practice, there is leakage from the corner reflector. The leakage increases as $s_\lambda$ increases, that is, as the dipole-antennas are placed far from the apex of the corner reflector. Hence, it is appropriate to chose $s_\lambda$ less than 0.45 $\lambda_0$.

The combination of the structure parameters of the primary feed providing the maximum illumination efficiency is as follows. The corner apex angle $\alpha$ of the corner reflector is 120°, the distance $s_\lambda$ between the dipole-antenna and the corner apex is 0.35 $\lambda_0$, and the distance $\rho_0$ between the parabola focal point and the corner apex is 0.05 $\lambda_0$. The illumination efficiency is estimated to be 89.8% for the $F/D$ ratio of 0.5.

## 3.4 Reflection Efficiency

As losses from the reflector surface, the transmission loss and the phase error loss are taken into consideration. The transmission loss is due to the use of the stainless steel wires in place of a perfect surface in the parabola and corner reflector, and the phase error loss is caused by the deviation of the reflection surface from the ideal surface.

The transmission loss is evaluated with the wave reflection coefficient by the stainless wire grid formed in the air, whereas the scattering and diffraction by the stainless wires are neglected. The efficiency based on the transmission loss $\eta_T$ expressed in terms of power ratio of the reflected wave to the incident wave is given by

$$\eta_T = 1 - U_T^2, \tag{3.10}$$

where $U_T$ is the amplitude of the transmitted wave $V_2$ compared with that of the incident



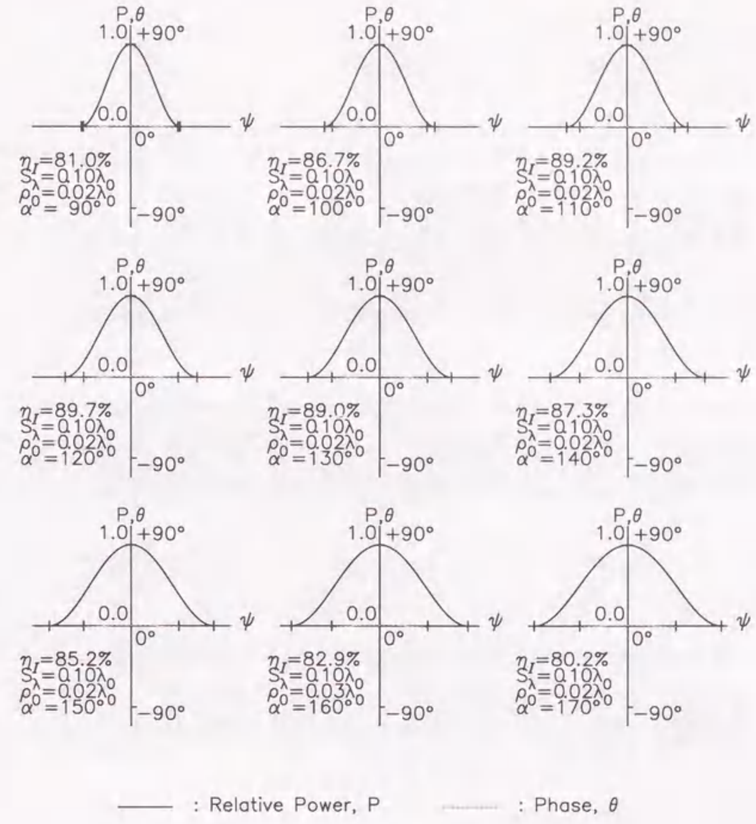


Figure 3.6: Radiation pattern of the primary feed and phase distribution on the parabola aperture ($\psi$=$\phi - \phi_0$) for $s_\lambda$ of 0.10 $\lambda_0$. The solid line is the relative power of the radiation pattern from the primary feed. The light line is the phase distribution on the parabola aperture. On the horizontal axis, two internal marks indicate the location of the parabola edges, and two outer marks indicate the corner angles of the corner reflector.

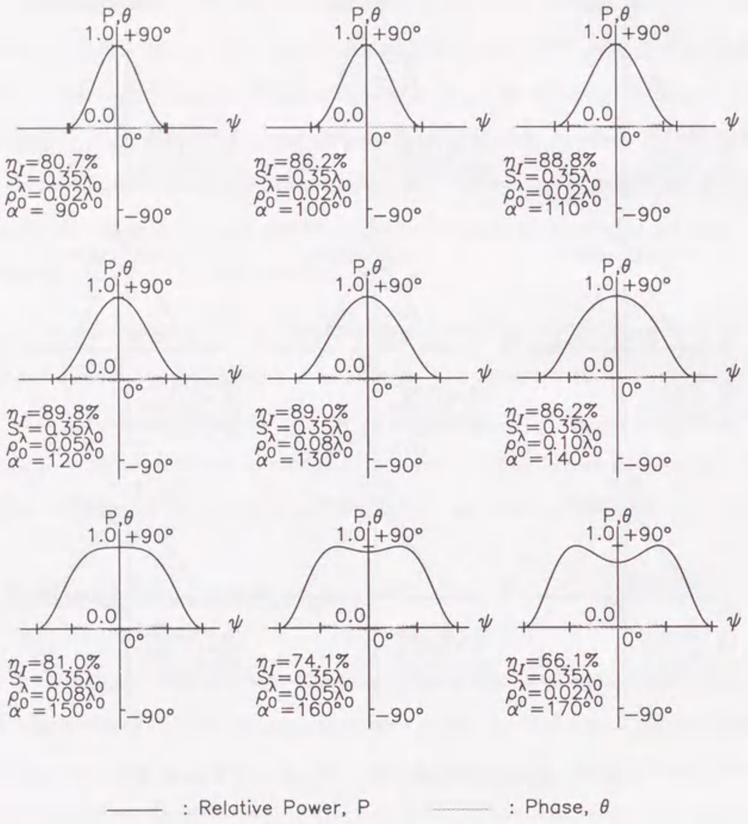


Figure 3.7: Radiation pattern of the primary feed and phase distribution on the parabola aperture ($\psi$=$\phi-\phi_0$) for $s_\lambda$ of 0.35 $\lambda_0$. The line sort and mark represent the same meanings as the previous figure.



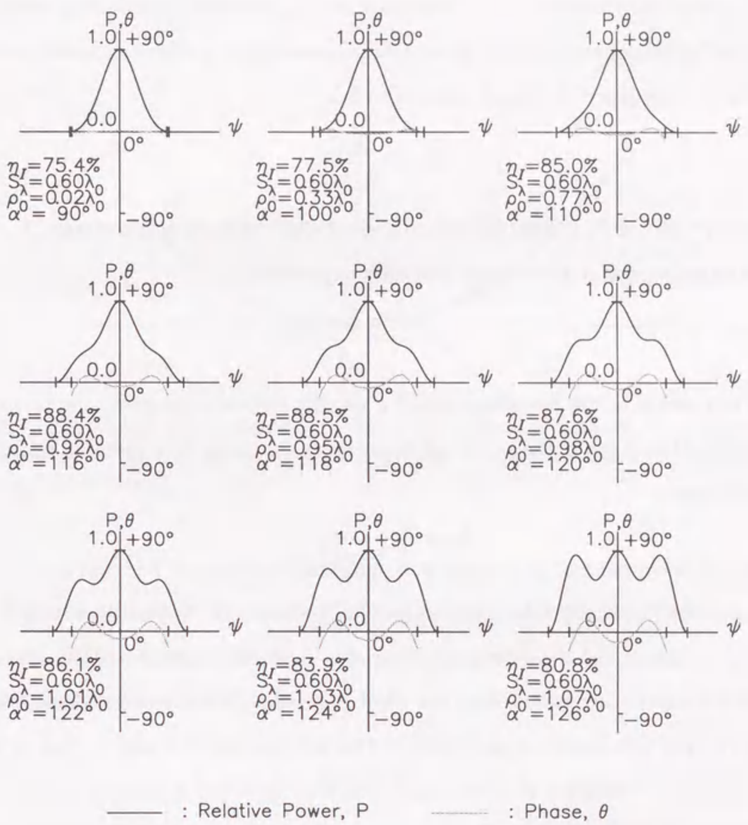


Figure 3.8: Radiation pattern of the primary feed and phase distribution on the parabola aperture ($\psi$=$\phi-\phi_0$) for $s_\lambda$ of 0.60 $\lambda_0$. The line sort and mark represent the same meanings as the previous figure.

wave $V_1$ [9],

$$U_T = \frac{V_2}{V_1}, \tag{3.11}$$

$$= \frac{2Z_2}{Z_2 + Z_1}. \tag{3.12}$$

Here $Z_1$ is the intrinsic impedance of free space and $Z_2$ refers to the reflecting medium. According to the propagation theory along transmission lines, a reflecting mesh corresponds to a lumped impedance $Z_s$ placed across the line,

$$Z_2 = \frac{Z_1 Z_s}{Z_1 + Z_s}. \tag{3.13}$$

The resistive part of $Z_s$ is usually negligible compared with the reactive part $X_s$, and the reactive impedance of a wire screen is simply expressed by

$$X_s = \frac{120\pi d \ln(\frac{d}{2\pi a})}{\lambda}. \tag{3.14}$$

Here, $a$ is a radius of the stainless wire, $d$ a spacing between the wire centers, and $\lambda$ the wavelength. If we have a wave arriving from space normally to a metallic surface, $Z_1$ is $120\pi$, and then

$$U_T = \frac{1}{1 + \frac{1}{2\frac{d}{\lambda}\ln(\frac{d}{2\pi a})}}. \tag{3.15}$$

The phase error loss of the parabolic surface is caused by two factors; the gravitational sag of the stainless wires from the horizontal surface and the deviation of the reflector supporting frame from the ideal parabola. When the stainless wire with a weight of $W$ per unit length is supported by two points separated with $l_f$ (Figure 3.9) and is stretched with a tension of $T$, the deviation $\delta(z)$ from the horizontal surface is given as a function of the horizontal distance $z$ from the maximum deviation point under the approximation by a parabolic curve [10]

$$\delta(z) = D_l - \frac{1}{2C} z^2, \tag{3.16}$$

where

$$D_l = \frac{W l_f^2}{8T}, \tag{3.17}$$

$$C = \frac{T}{W}. \tag{3.18}$$



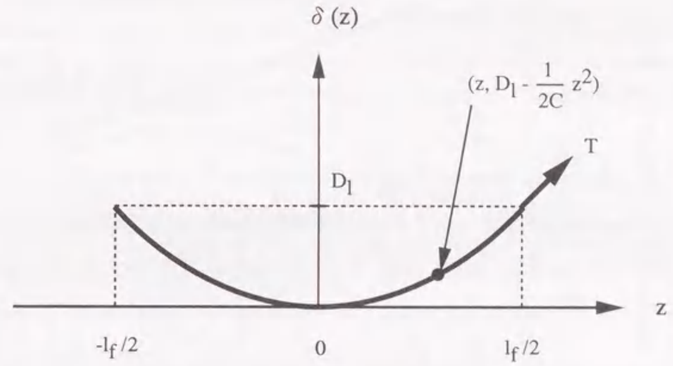


Figure 3.9: The sag of the stainless wire from the horizontal surface. The heavy line is the stainless wire which is stretched with a tension $T$. $D_l$ gives the vertical distance of the maximum deviation.

In the case of one-end suspended parabolic structure as in the asymmetric parabolic cylinder, the deviation from the ideal parabola is mainly due to the twisted deformation by the self weight. The deviation $\delta(y)$ is approximated to be proportional to the fourth power of the distance from the parabola origin,

$$\delta(y) = cy^4, \tag{3.19}$$

where $c$ is an arbitrary constant. The efficiency caused by the phase error of the parabola reflector [11] is given by

$$\eta_P = 1 - \left(\frac{4\pi}{\lambda}\sigma_{rms}\right)^2, \tag{3.20}$$

where $\sigma_{rms}$ is the root mean square of the deviation from the ideal parabola surface, and is given by

$$\sigma_{rms} = \sqrt{\frac{1}{S}\int_0^D \int_0^{l_f} \{\delta(z) + \delta(y)\}^2 dz dy}. \tag{3.21}$$

Here $S$ is the aperture area of the parabola.

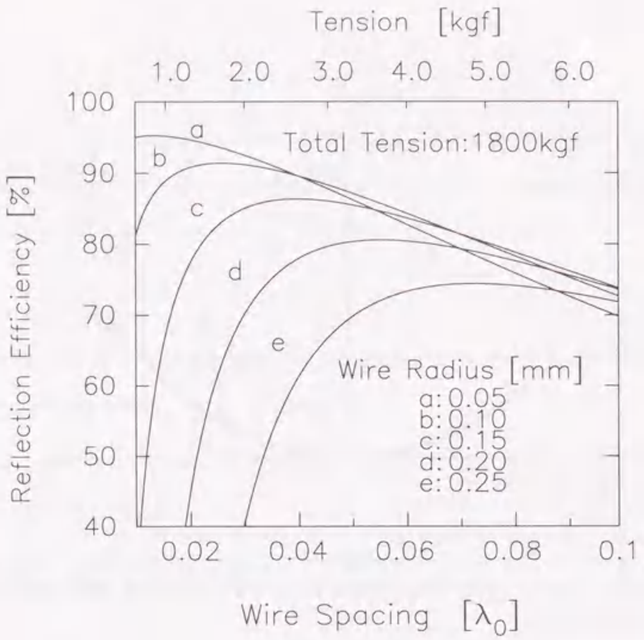


Figure 3.10: Reflection efficiency vs. wire spacing for various wire radii. The total tension to the edge frames of the parabolic reflector is 1800 kgf, so the wire spacing dominates the tension on each wire.

Figure 3.10 shows the variation of the reflection efficiency of the parabola reflector surface versus the spacing of the stainless wires, derived from Equation 3.10 and 3.20 for several values of the wire radius. In the calculation, the specific weight of the stainless wire was assumed to be 8 g $cm^{-3}$. The tension on each stainless wire is set such that the total tension applied to the edge frame of the parabolic reflector does not exceed 1800 kgf. The maximum warp at the tip of the parabolic frame was set to be 35 mm which is obtained by computer simulation for the structure design at various rotation angles of the reflector. It is found that there exists an optimum spacing between the stainless wires maximizing the efficiency for each radius if the total tension is limited, and that the efficiency is higher for thinner wires. However, if the stainless wire is made too thin, a practical problem of mechanical strength occurs. Especially, the weight due to snow attached to the stainless wires could break them. Hence, in the actual parabolic reflector the stainless wire with a radius of 0.15 mm is used, and the spacing between the stainless wires is 30 mm and the tension to each wire 2 kgf. Then, the reflection efficiency is expected to be 85.7 %.



Table 3.2: Structure parameters of the antenna.

| | | |
|---|---|---|
| Corner angle of the corner reflector: $\alpha$ | | 120° |
| Distance between the corner apex and the dipole antenna: $s_\lambda$ | | $0.35\lambda_0$ |
| Distance between the corner apex and the parabola focal point: $\rho_0$ | | $0.13\lambda_0$ |
| Corner reflector length: $L$ | | $2\lambda_0$ |
| Diameter of the stainless wire: $2a$ | | 0.3mm$\phi$ |
| Spacing between stainless wire centers: $d$ | Parabola surface | 30mm |
| | Corner reflector | 20mm |
| Tension to each stainless wire: $T$ | | 2kgf |

The surface accuracy of the corner reflector is improved by placing the support frames of the reflector at every 6.125 m and stretching the stainless wires with the spacing of 20 mm. Hence, the phase error loss due to the warp of the corner reflector surface can be neglected, and only the transmission loss is considered. The reflection efficiency of the corner reflector is 98.6 %.

## 3.5 Measurements

Table 3.2 lists the structure parameters of the primary feed, parabolic reflector, and corner reflector in the actually constructed antenna. Although the maximum illumination efficiency was obtained for $\rho_0$ of 0.05 $\lambda_0$, 0.13 $\lambda_0$ was chosen from the structural restriction. The calculation using the listed parameters gives the aperture efficiency of 75.9 %. In the analysis it is assumed that there is no leakage from the corner reflector, because the corner reflector length $L$ is 2 $\lambda_0$ which is much larger than $s_\lambda$. In this section, we actually measure the characteristics of the asymmetric parabolic cylinder antenna to confirm validity of the structure parameters of the primary feed with the corner reflector and reality of the high aperture efficiency of the antenna.

### 3.5.1 Aperture Efficiency

The gain measurement of the antenna is carried out using a celestial radio source [12]. The antenna gain is given by [13]

$$G_a = \frac{8\pi k T_a}{\lambda^2 S(\lambda)}, \tag{3.22}$$

$$= \frac{8\pi w}{\lambda^2 S(\lambda)}, \tag{3.23}$$

where $S(\lambda)$ is the flux density of the point radio source at a wavelength of $\lambda$, $k$ Boltzmann's constant, $T_a$ antenna temperature due to the radio source, $w$ power per unit bandwidth. The celestial source Cygnus A was used for the measurement because it has a strong radio intensity and long term variation in the intensity is little. In addition, the radio source can be considered as a point source for the beam width of the antenna. The radio intensity at 327 MHz is 5530 Jy (1 Jy=$10^{-26}$ W/Hz/m$^2$) which is estimated from observations at several frequencies assuming the power-law spectrum of the flux density [13].

The power difference with the antenna-beam pointed to the on-source and off-source is $-33.7\pm0.1$ dBm, which corresponds to the total power at the antenna terminals. The power was measured at an IF stage with a bandwidth of 5 MHz. The error contained in this measurement is due to the fact that the minimum pointing control angle of the antenna is 0.2° in the elevation. The gain from inputs of the pre-amplifier units to the IF stage of the receiver is $63.8\pm0.2$ dB from the measurement using a standard signal. Subtracting the measured gain from the total power, the antenna power from the radio source is

$$W_a = -33.7 - 63.8 = -97.5 \text{ dBm} = 1.778 \times 10^{-13} \text{ W}. \tag{3.24}$$

Hence, the antenna gain is obtained from Equation 3.23,

$$G_a = \frac{8\pi \times \frac{1.778\times10^{-13}}{5\times10^6}}{0.917^2 \times 5530 \times 10^{-26}} = 42.8 \pm 0.3 \text{ dBi}. \tag{3.25}$$

This antenna gain involves the phase error loss of 0.1 dB in the 5-bit digital phase shifter and the transmission line loss of 0.1 dB from the dipole antenna to the pre-amplifier unit. The VSWR of the primary feed is 1.50 on the average in the frequency range of $327\pm2.5$ MHz. The antenna gain is then corrected to be 43.2 dBi. The antenna gain is



also written as

$$G_a = \eta \frac{4\pi A_p}{\lambda^2}, \tag{3.26}$$

where $A_p$ is a physical aperture area, and $\lambda$ is wavelength. From Equation 3.26 the aperture efficiency is obtained as [14]

$$\eta = \frac{0.917^2 \times 21038}{4\pi \times 27 \times 73.5} = 71 \pm 5\ \%, \tag{3.27}$$

which corresponds to the effective aperture area of 1409 m$^2$. The 10% error of the aperture efficiency is the measurement error of the gain in the receiver system and that of the received power of the celestial source Cygnus A.

There is discrepancy of 5 % between the calculated and measured aperture efficiency. The possible reasons are that 1) the wave radiated from the primary feed leaks out from edges of the parabola reflector in the cylinder axis direction, which was ignored in the calculation, and 2) the spillover from the primary feed in the vertical plane is caused by the finite length of the corner reflector which was assumed to be infinite in the calculation.

### 3.5.2 Far-Field Pattern

The far-field patterns in the elevation direction are shown in Figure 3.11. The solid line is calculated by the radiation pattern of the primary feed in the vertical plane. The far-field pattern is derived from the Fourier transform of the aperture distribution which is assumed to be equal to the radiation pattern. The dashed line is measured using the celestial source. The elevation pattern is obtained by moving the antenna in the north-south direction so that the main beam traverses the radio source. The 3 dB beam width of the pattern is 2.1° which agrees well with the calculated value.

The locations of the sidelobes nearly coincide with the calculated ones. However, their sidelobe levels are different about 5 dB. The reason for this difference is the distortion from the ideal surface, as described in the previous section. The asymmetry of the far-field pattern is caused by the asymmetry of the aperture distribution due to the asymmetry of the parabola reflector.

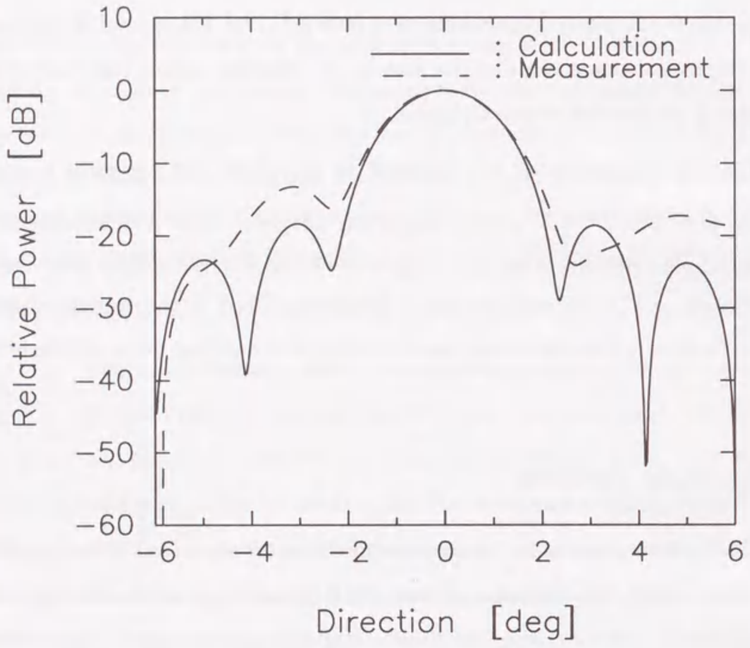


Figure 3.11: Far-field pattern of the asymmetric parabolic cylinder antenna in elevation. The solid line is derived from the calculation which is the Fourier transform of the aperture distribution. The dashed line is from the measurement which is obtained by using a celestial source.



## 3.6 Summary

We discussed about the design of the asymmetric parabolic cylinder antenna. The radiation characteristics of the primary feed and surface accuracy of the reflector have been investigated, and the optimum design was then conducted to achieve high aperture efficiency. When the positional relationship is chosen to maximize the illumination efficiency, the optimum apex angle of the corner reflector is 120° for the parabola with the $F/D$ ratio of 0.5. There is a restriction for the location of the dipole antenna providing the maximum efficiency. The same analysis method can be applied to the optimum design of the primary feed for the parabola antenna with the different $F/D$ ratio.

The reflection efficiency was computed from the transmission loss and the phase error loss of the parabola reflector and the corner reflector, formed by stretching the stainless wires. Then the aperture efficiency was estimated to be 75.9% from the reflection efficiency and the illumination efficiency. Further, the characteristics of the asymmetric parabolic cylinder antenna actually constructed were evaluated using a celestial radio source in order to obtain the feasibility of the high aperture efficiency in the antenna and the validity of the optimum parameters of the primary feed. From the measurement, it was found that the aperture efficiency and the far-field pattern were close to the computed results, and hence the validity was confirmed.

# Bibliography


[1] K. Asai, M. Kojima, H. Misawa, Y. Ishida, K. Maruyama, N. Yoshimi, M. Wakasa, and M. Karakida, Design of an asymmetric parabolic cylinder antenna with high aperture efficiency, *Transactions of the Institute of Electronics, Information and Communication Engineers*, **J78-B-II**, No.3, pp.102–109, 1995.

[2] V. K. Kapahi, S. H. Damle, V. Balasubramanian, and G. Swarup, An electrically steerable array of 96 dipoles for the Ooty radio telescope, *Journal of the Institution of Electronics and Telecommunication Engineers*, **21**, 3, pp.117–122, 1975.

[3] P.-S. Kildal, and E. Sørngård, Circularly polarized feed for cylindrical parabolic reflector antennas, *Institute of Electrical and Electronics Engineers Transactions on Antennas and Propagation*, **AP-28**, 2, pp.210–215, 1980.

[4] F. Mizusawa, Effect of the scattering pattern of the subreflector on the radiation characteristics of shaped-reflector Cassegrain antennas, *Institute of Electronics, Information and Communication Engineers Transactions*, **52-B**, pp.78–85, 1969.

[5] P.-S. Kildal, Diffraction corrections to the cylindrical wave radiated by a linear array feed of a cylindrical reflector antenna, *Institute of Electrical and Electronics Engineers Transactions on Antennas and Propagation*, **AP-32**, No.10, pp.1111–1116, 1984.

[6] P.-S. Kildal, Aperture efficiency and line feed phase center of parabolic cylindrical reflector antenna, *Institute of Electrical and Electronics Engineers Transactions on Antennas and Propagation*, **AP-32**, 6, pp.553–561, 1984.

[7] E. A. Wolff, *Antenna Analysis*, pp.299–305, John Wiley & Sons, 1966.







[8] P.-S. Kildal, Combined E- and H-plane phase centers of antenna feeds, *Institute of Electrical and Electronics Engineers Transactions on Antennas and Propagation*, **AP-31**, 1, pp.199–202, 1983.

[9] W. N. Christiansen, and J. A. Hogbom, *Radiotelescopes*, pp.61–62, Cambridge University Press, 1969.

[10] The Institute of Electrical Engineers of Japan (ed.), *Electrical Engineering Handbook*, pp.1193–1194, 1967.

[11] K. Rohlfs, *Tools of Radio Astronomy*, Springer-Verlag Berlin Heidelberg, pp.83–85, 1986.

[12] T. Satoh, and A. Ogawa, Exact gain measurement of large aperture antenna using celestial radio sources, *Institute of Electrical and Electronics Engineers Transactions on Antennas & Propagation*, **AP-30**, 1, pp. 157–161, 1981.

[13] J. D. Kraus, *Radio Astronomy (2nd edition)*, p.7-4, Cygnus-Quasar Books, 1986.

[14] J. D. Kraus, *Antennas (2nd edition)*, pp.97–104, McGraw-Hill, 1988.

# Chapter 4

# Calibration of the Phased Array System

## 4.1 Calibration Methods

The phased array installed in the primary feed system of the Kiso radio telescope (asymmetric parabolic cylinder antenna [1]) is used for tracking a radio source in the azimuth direction. Source-tracking with a phased array needs to provide the appropriate gain and phase for all the array-elements. Unless gain and phase of each array-element are correctly calibrated in the phased array, sidelobes increase and signal to noise ratio decreases. To calibrate the phased array system, gain and phase should accurately be measured in each channel including the array-elements and signal amplifier circuits.

There are two kinds of method for the calibration of the phased array. One method is to use radio waves from a distant radiation source [2, 3, 4, 5], while another method uses calibration test signals distributed to the phased array [5, 6, 7, 8, 9]. Although the former method allows us to measure the gain and phase of all the paths including reflectors and structures around the array-elements, a transmitter is generally necessary except when using a natural radio source. Even in the use of the natural radio source, the calibration time is limited around the meridian transit of the source. The radiated wave from a calibration source is picked up with the phased array controlling the phase shifters. The gain and phase of each channel are obtained by analyzing the received signal. The latter method has an advantage in that the automatic measurement of the gain and phase is possible whenever it is required. In this method, the additional calibration system is





necessary for measuring the gain and phase of the calibration test signal. The calibration test signal is distributed to each array-element through the calibration network, and the returned signal is collected through the gathering network of the receiver system. The distributed signal is modulated or rooted at the feed point to measure the gain and phase with an instrument.

A method which was previously employed in our system [9] measures relative differences of gain and phase between adjacent two elements of the phased array feeding a calibration test signal. However, this method has the following weak points: (1) Absolute measurement may involve systematic errors that accumulate in measuring the adjacent elements; (2) The absolute measurement becomes impossible even if only one element is broken. Therefore, a calibration method needs to satisfy the following conditions:

(i) High accuracy;
(ii) Measurable even if there are a few damaged array-elements; and
(iii) Automated calibration when it is required.

To satisfy these conditions, we introduce a "loop-method" and use a "REV-method" to check the calibration with the loop-method. The loop-method measures the gain and phase of each channel relative to a reference channel using a loop of transmission lines linked through signal inputs of pre-amplifier units of the array-elements. The great merit of the loop-method is that it does not require accurate knowledge of the electrical lengths for the transmission lines in the system. This is important for application to such large system as our phased array. However, the loop-method gives the phase solution ambiguity of 180°. The loop-method was proposed by Little and Payne-Scott [6], and was extended by Morimoto and Labrum [8] who employed this loop-method in the Culgoora radioheliograph(Australia). Morimoto and Labrum tried to exclude the ambiguity of 180° in the phase measurement, making the spacing between linking points a whole number of wavelength or approximately constant. But the distinction between system stability and measurement accuracy is not clearly described in their paper. We realize the loop-method to measure the gain and phase of each channel, and propose a method to eliminate the ambiguity of 180° in the phase measurement [10].

The measurement with the loop-method is limited to paths of the feed network behind signal inputs of the pre-amplifier units. Therefore, to measure the characteristics of element-antennas and structures around the phased array (e.g., reflectors), we apply the Rotating Electric-field Vector method (REV-method) [2]. The REV-method measures radio source scanning patterns which are made by an interferometer of any adjoining two elements of the phased array. The gain and phase of each channel are obtained from the scanning patterns.

In addition to the above two methods, the reflection-method is also introduced to measure the absolute gain of each channel. The reflection-method can determine the power level of the calibration test signal at inputs of the pre-amplifier units. Measuring the total gain through the calibration network, preamplifier units, and gathering network, the gain of each channel is obtained. In principle, the reflection-method can be applied to measurements of the calibration test signal at the inputs of all the pre-amplifier units. However, it is difficult to detect the reflected signals for all the array-elements because of the large loss caused by many steps of switch circuits and long cables. Hence, the reflection-method is employed for measuring the absolute signal level at the input of the calibration loop network. The combination of the reflection- and loop-methods was actually used for determining the gain of the feed network in the previous section.

## 4.2 Calibration System

Figure 4.1 shows a schematic diagram of the phased array and calibration system. The phased array consists of 144 half-wave dipole-antennas and 72 pre-amplifier units which include pre-amplifiers, phase shifters, and variable attenuators. Each dipole-antenna is placed every 0.56 wavelength in the east-west direction. Adjacent two dipole-antennas are connected to a pre-amplifier unit. The outputs from the 72 pre-amplifier units are combined to one through a signal combiner system. The calibration system consists of a signal oscillator section (A in Figure 4.1), a calibration signal selector section (B in Figure 4.1), and a calibration signal measurement section (C in Figure 4.1). In the signal oscillator section (located in the house, A in Figure 4.1), calibration signals



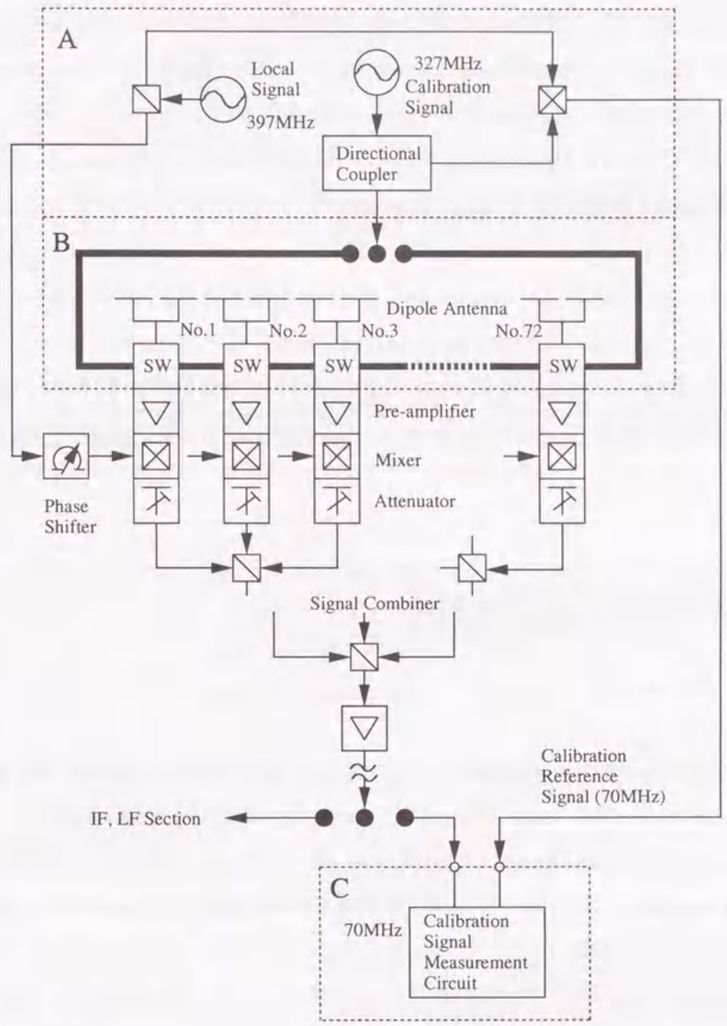


Figure 4.1: Circuit diagram of the calibration system (A: Signal oscillator section, B: Calibration signal selector section, C: Calibration signal measurement section). The heavy line is the loop line which is used for two calibration methods: loop-method and reflection-method. The calibration test signal is distributed to each element of the phased array through the loop line and switches in the calibration signal selector section.

are generated. The output signal (327 MHz) from a signal oscillator is divided into two signals which are used to measure the gain and phase. One is directly transmitted to the calibration signal measurement circuit as a reference signal, and the other is also transmitted to the circuit through the calibrated channel. In Figure 4.1 each local oscillator signal (397MHz) is distributed from the same standard signal, and the calibration reference signal (70MHz) is generated by mixing the calibration signal (327MHz) and the local oscillator signal (397MHz). The calibration signal selector section (located at midpoint between the dipole-antenna and the pre-amplifier; SW) selects the channel to be calibrated. Adjacent switches are serially connected each other to make a loop transmission line for gain and phase measurement with the loop-method (B in Figure 4.1). The calibration signal measurement section (located in the house) measures the gain and phase of the signal.

## 4.3 Reflection-Method

### 4.3.1 Principle

The reflection-method is applied to the absolute gain measurement of the both end channels in the phased array. Here, the reflection-method is explained using a principle schematic shown in Figure 4.2. If the amplitudes at the input and output point of DUT are measured, the gain of the DUT is obtained. It is easy to measure the amplitude at the DUT output point which is in the observation room. However, the direct measurement at the DUT input point is messy because it is in the primary feed of the antenna. We then use the reflection-method so that the amplitude and phase at the DUT input point can be measured remotely in the observation room. First, a calibration signal from the signal generator (SG) is reflected at the terminal point (T) where the DUT is connected. The reflected signal $\mathbf{R}_R$ from the terminal is then measured with the phase and gain measurement circuit (VVM). However, the measured signal actually involves the leak component $\mathbf{R}_N$ from the directional coupler (DC), connector junction, and so on. So, the required component can be detected by making the terminal opened and shorted.



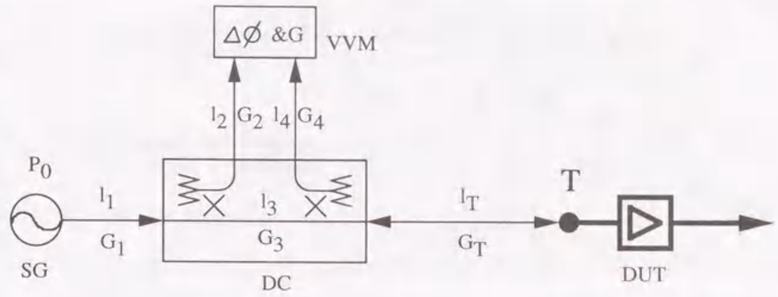


Figure 4.2: Principle schematic for measuring gain and phase with the reflection-method. The DUT to be measured is shown with a heavy line. The calibration test signal is reflected at the terminal point T. SG, DC, and VVM stand for a signal generator, directional coupler, and phase and gain measurement circuit, respectively.

The total reflected signal through the DC is given at the VVM as

$$\mathbf{R}_O = \mathbf{R}_R + \mathbf{R}_N \quad : \text{open}, \tag{4.1}$$

$$\mathbf{R}_S = -\mathbf{R}_R + \mathbf{R}_N \quad : \text{short}. \tag{4.2}$$

The reflected signal is the same in amplitude, but has phase difference $\pi$ between the open and the short at the terminal. It is assumed that the open and short of the terminal are switched within a short time, and the length and loss of the transmission line have no change during the measurement.

In Equation 4.1 and 4.2, the measurable parameters are the amplitude $|\mathbf{R}_O| = R_O$, $|\mathbf{R}_S| = R_S$ and phase $\theta_O$, $\theta_S$, while unknown parameters are $R_R$ ($=|\mathbf{R}_R|$), $\theta_R$, $R_N$ ($=|\mathbf{R}_N|$), and $\theta_N$. So, the unknown parameters are solved as

$$\mathbf{R}_R = \frac{1}{2}(\mathbf{R}_O - \mathbf{R}_S), \tag{4.3}$$

$$= \frac{1}{2}(R_O e^{j\theta_O} - R_S e^{j\theta_S}). \tag{4.4}$$

$$\mathbf{R}_N = \frac{1}{2}(\mathbf{R}_O + \mathbf{R}_S), \tag{4.5}$$

$$= \frac{1}{2}(R_O e^{j\theta_O} + R_S e^{j\theta_S}). \tag{4.6}$$

Here

$$R_R = \frac{\sqrt{(R_O\cos\theta_O - R_S\cos\theta_S)^2 + (R_O\sin\theta_O - R_S\sin\theta_S)^2}}{2}, \quad (4.7)$$

$$\theta_R = \tan^{-1}\frac{R_O\sin\theta_O - R_S\sin\theta_S}{R_O\cos\theta_O - R_S\cos\theta_S}, \quad (4.8)$$

$$R_N = \frac{\sqrt{(R_O\cos\theta_O + R_S\cos\theta_S)^2 + (R_O\sin\theta_O + R_S\sin\theta_S)^2}}{2}, \quad (4.9)$$

$$\theta_N = \tan^{-1}\frac{R_O\sin\theta_O + R_S\sin\theta_S}{R_O\cos\theta_O + R_S\cos\theta_S}. \quad (4.10)$$

Equation 4.7 and 4.8 are expressed using the gain and electrical length shown in Figure 4.2. The output signal $P_0$ from the SG is transmitted to the DC through the transmission line with gain $G_1$ and electric length $l_1$, and divided into two paths. One is transmitted to the VVM through the line with $G_2$ and $l_2$ for the reference signal of the measurement. The other signal reaches the terminal T through the line with $G_3$ and $l_3$, and with $G_T$ and $l_T$, and is perfect-reflected at the terminal T. The reflected signal returns to DC through the line with $G_T$ and $l_T$, and is transmitted to the VVM through the line with $G_4$ and $l_4$. Then $R_R$ and $\theta_R$ are expressed as

$$R_R = \sqrt{Z_0(P_0\cdot G_1\cdot G_3\cdot G_T\cdot G_T\cdot G_4)}, \quad (4.11)$$

$$\theta_R = \frac{2\pi}{\lambda}\{l_1 + l_2 - (l_1 + l_3 + l_T + l_T + l_4)\}, \quad (4.12)$$

where $\lambda$ is wavelength of the signal, and $Z_0$ is characteristic impedance of the transmission line. All the parameters $P_0$, $G_1$, $G_3$, $G_4$, $l_1$, $l_2$, $l_3$, and $l_4$ belong to the measurement system of the SG, DC, and VVM. So, they are actually treated as known parameters. Then, $G_T$ and $l_T$ are derived from Equation 4.11 and 4.12,

$$G_T = \frac{R_R}{\sqrt{Z_0(P_0\cdot G_1\cdot G_3\cdot G_4)}}, \quad (4.13)$$

$$l_T = \frac{1}{2}\cdot(l_2 - l_3 - l_4 - \frac{\lambda}{2\pi}\theta_R). \quad (4.14)$$

Thus, the amplitude $A_T$ and phase $\phi_T$ relative to the reference signal at the terminal T are

$$A_T = \sqrt{Z_0(P_0\cdot G_1\cdot G_3\cdot G_T)}, \quad (4.15)$$

$$= \sqrt{\sqrt{\frac{Z_0(P_0\cdot G_1\cdot G_3)}{G_4}}\cdot R_R}. \quad (4.16)$$



$$\phi_T = \frac{2\pi}{\lambda}(l_2 - (l_3 + l_T)), \quad (4.17)$$

$$= \frac{\pi}{\lambda}(l_2 - l_3 + l_4) + \frac{1}{2}\theta_R. \quad (4.18)$$

### 4.3.2 Practical System

Although the reflection-method is useful for measuring the amplitude and phase at the DUT input point (terminal T), the actual measurement is limited to a part of channels in the feed network. Because the signal loss varies largely with length of the transmission line in a high-frequency circuit, it is difficult for the VVM to cover the wide range of power level. Hence, the reflection-method is applied to the both end units No. 1 and 72. Once the amplitude of the end units is known, the absolute gain is obtained for all the channels from the loop-method.

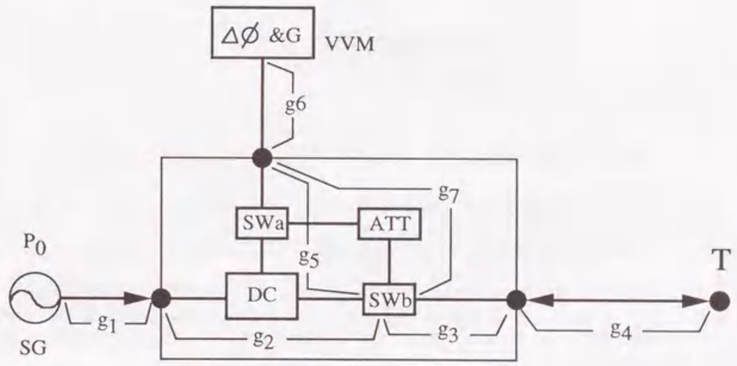


Figure 4.3: Self-calibration system of the reflection-method. The root through $SW_b$, ATT, and $SW_a$ is used for the self-calibration mode.

In Equation 4.16, the output level $P_0$ and gain $G_1, G_3, G_4$ are active parameters of the instrument in the observation room. The variation of room temperature could change values of those parameters. Then, the actual calibration system shown in Figure 4.3 has an additional circuit to monitor the level variation of the active elements. Switches $SW_a$ and $SW_b$ select two modes. One is the reflection mode that is the same as

the circuit shown in Figure 4.2, and measures the reflected signal from the terminal point T. The other one is the self-calibration mode that the signal from SG is transmitted to the VVM through $SW_b$, ATT, and $SW_a$.

The signal level of the reflection mode $L_a$, and the signal level of the self-calibration mode $L_b$ are in dB,

$$L_a = L_0 - (g_1 + g_2 + g_3 + g_4 + g_4 + g_3 + g_5 + g_6), \tag{4.19}$$

$$L_b = L_0 - (g_1 + g_2 + g_7 + g_6). \tag{4.20}$$

Here, $g_1$ and $g_6$ correspond to the gain of the calibration signal amplifier, and $g_4$ represents the cable loss between the calibration signal measurement circuit and the pre-amplifier unit in the feed system. $L_a$ and $L_b$ can be measured within a short time so that $L_0$, $g_1$, $g_2$, and $g_6$ do not change. The subtraction $\Delta L$ is

$$\Delta L = L_a - L_b, \tag{4.21}$$

$$= -2g_4 - 2g_3 - g_5 + g_7. \tag{4.22}$$

Then,

$$g_4 = \frac{1}{2}(-\Delta L - 2g_3 - g_5 + g_7), \tag{4.23}$$

$$= \frac{1}{2}\{-\Delta L - (g_3 + g_5) - (g_2 + g_3) + (g_2 + g_7)\}, \tag{4.24}$$

$$= \frac{1}{2}(-\Delta L - G_R - G_Q + G_S). \tag{4.25}$$

$G_R(g_3 + g_5)$, $G_Q(g_2 + g_3)$, and $G_S(g_2 + g_7)$ are measurable. The level of the calibration signal at the terminal point T is

$$L_T = L_0 - (g_1 + g_2 + g_3 + g_4), \tag{4.26}$$

$$= L_0 - g_1 - (g_2 + g_3) - g_4, \tag{4.27}$$

$$= L_0 - g_1 - G_Q - \frac{1}{2}(-\Delta L - G_R - G_Q + G_S). \tag{4.28}$$

The output level should also be checked for the calibration signal generator.

### 4.3.3 Measurement

Table 4.1 shows power levels of the calibration signal at the inputs of the pre-amplifier unit No. 1 and No. 72 which are located at the end elements of the phased array. The



output level of the self-calibration signal is 9.12 dBm, so the line loss from the calibration signal generator up to the end elements is about 27.7 dB. This corresponds to 160 m of the coaxial cable 5D-2V with a loss rate 180 dB/km at 300 MHz. Comparing the signal level with that directly measured with the power meter at the pre-amplifier unit inputs, the discrepancy is obtained to be 0.16 dB for No. 1 and 0.09 dB for No. 72. Thus, we confirm that the reflection-method can measure power level with accuracy of the order of 0.1 dB. The gain of the end channels can be determined by subtracting the signal level at the pre-amplifier unit input from the total gain over the whole route through the calibration network, pre-amplifier units, and gathering network.

Table 4.1: Signal level at the inputs of the pre-amplifier units with the reflection-method and the power meter.

| (dBm) | Reflection-method | Power meter |
|---|---|---|
| No. 1 | -18.17 | -18.33 |
| No. 72 | -19.05 | -19.14 |

The loss of the long coaxial cable from the signal generator to the pre-amplifier unit is large, so the output level of the calibration signal is set as high as 9.12 dBm in the reflection-method. However, the pre-amplifier might saturate with this high output signal. Then, the output level of the signal generator is set to $-31.28$ dBm instead of 9.12 dBm in measuring the output level of the receiver system. Thus, the gain is obtained to be 43.41 dB for No. 1 and 43.22 dB for No. 72.

## 4.4 Loop-Method

The principle of the loop-method is basically the same as Morimoto and Labrum [8]. However, the necessary portions are described to show an exclusion method of 180° ambiguity in the phase measurement. To simplify the explanation, we derive the relative phase and relative gain of two paths from a principle schematic of the loop-method as shown in Figure 4.4.

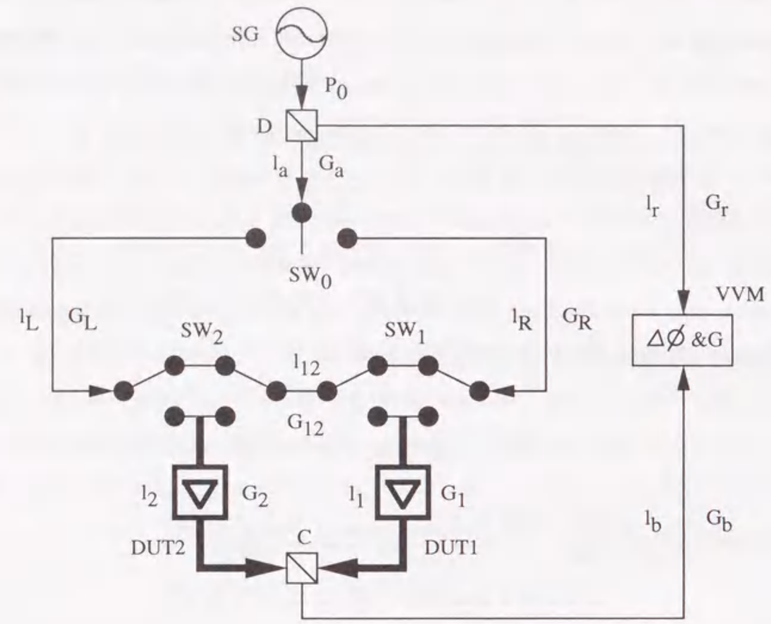


Figure 4.4: Principle schematic for measuring gain and phase with the loop-method. The DUTs to be measured are shown with heavy lines.

### 4.4.1 Principle

A signal $P_0$ from the calibration signal oscillator (SG) is divided into two signals with a signal divider. One is a reference signal which is transmitted to the phase and gain measurement circuit (VVM) through a transmission line with electric length $l_r$ and gain $G_r$ . The other one is transmitted to a loop line through the transmission line with $l_a$ and $G_a$. The signal on the loop line is led to the line of either right side ($l_R$, $G_R$) or left side ($l_L$, $G_L$) with a switch ($SW_0$). Each branch point connected with the transmission line ($l_{12}$, $G_{12}$) consists of switches ($SW_1$, $SW_2$) for taking the signal from the either right or left side. The electric length $l_1$ and $l_2$, and the gain $G_1$ and $G_2$ are parameters to be measured in paths (DUTs) 1 and 2. The output signal reaches the VVM through a signal



combiner (C) and the transmission line with $l_b$ and $G_b$.

In the VVM, the phase ($\phi_{1R}$, $\phi_{1L}$, and $\phi_{2R}$, $\phi_{2L}$) and gain ($G_{1R}$, $G_{1L}$ and $G_{2R}$, $G_{2L}$) for a calibration reference signal are obtained by switching $SW_1$, $SW_2$, and $SW_0$. The subscripts correspond to the clockwise and counterclockwise whose signals are supplied to the loop transmission line for the DUTs 1 and 2. The relation among these parameters is expressed as follows using a wavelength of the calibration signal $\lambda$,

$$\phi_{1R} = \frac{2\pi}{\lambda}\{l_r - (l + l_R + l_1)\} + 2n_{1R}\pi, \tag{4.29}$$

$$\phi_{1L} = \frac{2\pi}{\lambda}\{l_r - (l + l_L + l_{12} + l_1)\} + 2n_{1L}\pi, \tag{4.30}$$

$$\phi_{2R} = \frac{2\pi}{\lambda}\{l_r - (l + l_R + l_{12} + l_2)\} + 2n_{2R}\pi, \tag{4.31}$$

$$\phi_{2L} = \frac{2\pi}{\lambda}\{l_r - (l + l_L + l_2)\} + 2n_{2L}\pi, \tag{4.32}$$

$$G_{1R} = \frac{P_0}{\sqrt{2}} \cdot G \cdot G_R \cdot G_1, \tag{4.33}$$

$$G_{1L} = \frac{P_0}{\sqrt{2}} \cdot G \cdot G_L \cdot G_{12} \cdot G_1, \tag{4.34}$$

$$G_{2R} = \frac{P_0}{\sqrt{2}} \cdot G \cdot G_R \cdot G_{12} \cdot G_2, \tag{4.35}$$

$$G_{2L} = \frac{P_0}{\sqrt{2}} \cdot G \cdot G_L \cdot G_2. \tag{4.36}$$

Here, $l = l_a + l_b$ and $G = G_a \cdot G_b$. $n_{ij}\,(i = 1, 2;\ j = R, L)$ is an arbitrary integer. The actual range on the phase measurement $0 \sim 2\pi$ causes additions of $2n_{ij}\pi$ in the Equations 4.29 to 4.32.

The sum of the phase and the product of the gain for the clockwise and counterclockwise signals in the DUTs 1 and 2 give

$$\phi_{1R} + \phi_{1L} = \frac{2\pi}{\lambda}(L_t - 2l_1) + 2\pi(n_{1R} + n_{1L}), \tag{4.37}$$

$$\phi_{2R} + \phi_{2L} = \frac{2\pi}{\lambda}(L_t - 2l_2) + 2\pi(n_{2R} + n_{2L}), \tag{4.38}$$

$$G_{1R} \cdot G_{1L} = P_t \cdot G_1^2, \tag{4.39}$$

$$G_{2R} \cdot G_{2L} = P_t \cdot G_2^2, \tag{4.40}$$

where $L_t = 2(l_r - l) - (l_R + l_L + l_{12})$ and $P_t = (P_0^2/2) \cdot G^2 \cdot G_R \cdot G_L \cdot G_{12}$. The subtraction $\Delta\phi_{2-1}$ between Equations 4.37 and 4.38 and the division $\Delta G_{2-1}$ between Equations 4.39

and 4.40 are given as

$$\Delta\phi_{2\text{-}1} = 2\{-\frac{2\pi}{\lambda}(l_2 - l_1) + n\pi\}, \quad (4.41)$$

$$= 2(\phi_{2-1} + n\pi). \quad (4.42)$$

$$\Delta G_{2\text{-}1} = \left(\frac{G_2}{G_1}\right)^2. \quad (4.43)$$

Here the arbitrary integers are replaced by $n$. Then, the required relative phase $\phi_{2-1}$ and relative gain $G_2/G_1$ are obtained as

$$\phi_{2-1} = -\frac{1}{2}\Delta\phi_{2\text{-}1} + n\pi, \quad (4.44)$$

$$\frac{G_2}{G_1} = \sqrt{\Delta G_{2\text{-}1}}. \quad (4.45)$$

Thus, although the relative gain $G_2/G_1$ between the DUTs 1 and 2 is deduced from a square root of $\Delta G_{2-1}$, the relative phase $\phi_{2-1}$ cannot be derived from only $\Delta\phi_{2-1}$, because it contains an ambiguity of an integer multiple of $\pi$. Next, we explain the procedures for choosing a correct solution from the alternative phases (difference: $\pi$) in Equation 4.44.

### 4.4.2 Elimination of ambiguity $\pi$ in the relative phase

**A method that line-length between adjacent branches is taken to integer times of wavelength**

Morimoto and Labrum [8] have excluded the uncertainty $\pi$ in Equation 4.44, by making line-length between adjacent branches $l_{12}$ integer times of wavelength. Subtracting Equation 4.29 from 4.31, and Equation 4.30 from 4.32 yield

$$\phi_{2R} - \phi_{1R} = \frac{2\pi}{\lambda}\{-(l_2 - l_1) - l_{12}\} + 2\pi(n_{2R} - n_{1R}), \quad (4.46)$$

$$\phi_{2L} - \phi_{1L} = \frac{2\pi}{\lambda}\{-(l_2 - l_1) + l_{12}\} + 2\pi(n_{2L} - n_{1L}). \quad (4.47)$$

If $l_{12}$ is an integer multiple of the wavelength, the above equations are equal each other. That is, by introducing $l_{12} = n_0\lambda$ ($n_0$: arbitrary integer), the following equation can be established,

$$n_{2R} - n_{1R} = 2n_0 + n_{2L} - n_{1L}. \quad (4.48)$$



Then the arbitrary integer $n$ in Equation 4.44 is given as

$$n = n_{2R} + n_{2L} - n_{1R} - n_{1L}, \quad (4.49)$$

$$= 2(n_0 + n_{2L} - n_{1L}). \quad (4.50)$$

Thus, the uncertainty $\pi$ is eliminated.

When this method is applied to the phased array with 72 elements, the link-line lengths between any branches must keep integer times of wavelength. However, the length error in manufacture and phase change due to temperature variation become serious for the phase stability of the coaxial cables used for the link-lines among the 72 branches. Therefore, we propose an other elimination method in the next section.

**A method that line-length between adjacent branches is set within the range of 180°**

If the arbitrarity $2\pi$ is ignored in Equation 4.46, the relative phase is obtained as follows,

$$\phi_{2R} - \phi_{1R} = \frac{2\pi}{\lambda}\{-(l_2 - l_1) - l_{12}\}, \quad (4.51)$$

$$= -\phi_{2-1} - \phi_{12}, \quad (4.52)$$

where $\phi_{12}$ is the phase corresponding to the link-line $l_{12}$. Then

$$\phi_{2-1} = -(\phi_{2R} - \phi_{1R}) - \phi_{12}. \quad (4.53)$$

So this enables us to derive the relative phase between the DUTs 1 and 2, $\phi_{2-1}$ from the phase of the link-line between the two branch points $\phi_{12}$, which is independent of Equation 4.44. The subtraction of Equation 4.29 from 4.30 and subtraction of Equation 4.31 from 4.32 give

$$\phi_{1R} - \phi_{1L} = \frac{2\pi}{\lambda}\{-(l_R - l_L) + l_{12}\} + 2\pi(n_{1R} - n_{1L}), \quad (4.54)$$

$$\phi_{2R} - \phi_{2L} = \frac{2\pi}{\lambda}\{-(l_R - l_L) - l_{12}\} + 2\pi(n_{2R} - n_{2L}). \quad (4.55)$$

The subtraction between Equations 4.54 and 4.55 yields

$$\Delta\phi'_{2\text{-}1} = 2\{-\frac{2\pi}{\lambda}l_{12} + n'\pi\}, \quad (4.56)$$

then

$$\phi_{12} = -\frac{1}{2}\Delta\phi'_{2\text{-}1} + n'\pi, \tag{4.57}$$

where $n'$ is an arbitrary integer. Although $\phi_{12}$ in Equation 4.57 also contains the ambiguity $\pi$, this ambiguity is removed by comparison of the estimated $\phi_{12}$ with the designed value. That is, the unique solution of $\phi_{12}$ is determined by using the odd-even known length for the transmission lines used to link each branch point on the loop. Thus the ambiguity $\pi$ is excluded from the relative phase in Equation 4.53.

Actually, we consecutively derive $\phi_{12}$, $\phi_{23}$, $\phi_{34}$, $\cdots$, $\phi_{m(m+1)}$ from phase summation of the link-lines from the element No. 1, $\sum_{k=1}^{m}\phi_{k(k+1)}$. The phase relative to the element No. 1, $\phi_{(m+1)-1}$ is obtained as

$$\phi_{(m+1)-1} = -\{\phi_{(m+1)R} - \phi_{1R}\} - \sum_{k=1}^{m}\phi_{k(k+1)}. \tag{4.58}$$

$\phi_{(m+1)-1}$ in Equation 4.58 includes an accumulation error due to the phase summation of the link-lines between adjacent elements. However, the accumulation error is negligible when using $\phi_{(m+1)-1}$ as a reference to select the unique solution from two candidates of the relative phase with the ambiguity of $\pi$ in Equation 4.44. The actual line length between adjacent branch points $\phi_{m(m+1)}$ corresponds to roughly 40° including the phase of the calibration relays in the pre-amplifier unit.

### 4.4.3 Experimental Result of the loop-Method

The gain and phase measurement circuit (VVM) in the principle schematic of the loop-method (Figure 4.4) is identical to the calibration signal measurement circuit in Figure 4.1. The cosine and sine components of a signal are practically measured, and the gain and phase are calculated. The errors estimated from the input-output characteristics of the calibration signal measurement circuit are ±0.06dB for gain and ±0.5° for phase, respectively.

For the phased array installed in the asymmetric parabolic cylinder antenna, the gain and phase of each channel were measured using the calibration system shown in Figure 4.1. Figure 4.5 shows the experimental result of relative gain and relative phase for



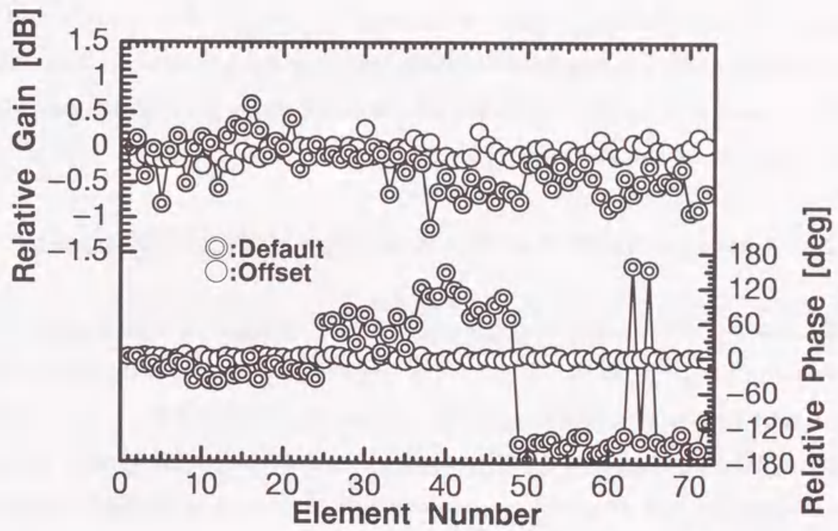


Figure 4.5: The relative gain and phase measured with the loop-method. The double circle represents the default status of phase shifters and variable attenuators. The signal circle represents gain and phase distributions after calibrating each channel using the offset values from the default status measurement.

each channel obtained with the loop-method. The upper and lower plots are the relative gain and relative phase, respectively. Channel No. 1 is taken as a reference. The double circle represents the measurement in the default status of the phase shifters and variable attenuators. The single circle represents the measurement after calibrating the gain and phase of each channel using the offset values from the default status measurement. Before the calibration, one can see that gain distribution is within the adjustable range of the variable attenuator ($\pm 1.6$ dB), and that there are three groups in the phase distribution. The reason why the three groups exist is that the signal gathering network consists of three groups in the phased array. The gain and phase of each channel after the calibration are set uniformly within standard deviation of 0.1dB for gain and 3.2° for phase, respectively, which indicate that the gain and phase were calibrated within the quantum error of the variable attenuator and phase shifter.

## 4.5 Comparison between Loop- and REV-methods

In the loop-method, the measurements are limited to the gathering network and receiver system after the pre-amplifier units and do not involve the properties of the array-element and structure around the phased array, e.g., reflector. To estimate its effect, we applied the Rotating Electric-field Vector (REV) method [2] to measure all over the paths including the pre-amplifier unit, array-element, and reflector. The results of the REV-method are compared with those of the loop-method.

### 4.5.1 REV-method

The REV-method measures beam patterns of the phased array using a distant radio source with the known position [2]. We then obtain gain and phase of the array-elements by analyzing the beam patterns. The beam scans the source in a short time by quickly phasing the array-element with a phase shifter. To simplify a control of the phase shifter, we takes the simplest case of the REV-method, by making an interferometer with two array-elements in the phased array (Figure 4.6).

Any two dipole-elements in the phased array receive the plane wave from a



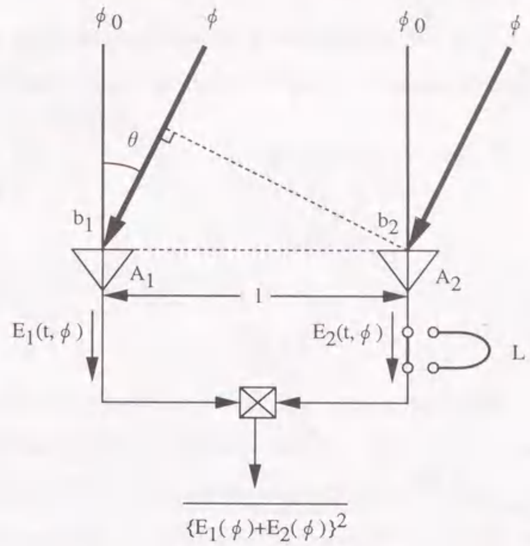


Figure 4.6: Interferometer with two array-elements. Radio waves come from the direction shown as fat arrows. $L$ represents a delay line in the phase shifter.

distant radio source. Amplitude and phase of the electric field vector are $E_0, \theta_0$ for a reference element and $E_n, \theta_n$ for the $n$th element. Phasing the $n$th element, the total electric field is given by

$$\mathbf{E}_T = E_0 e^{j\theta_0} + E_n e^{j(\theta_n + \Delta)}, \tag{4.59}$$

where $\Delta$ is the phase given by the phase shifter of the $n$th element. Then,

$$|\mathbf{E}_T|^2 = \{E_0 \cos\theta_0 + E_n \cos(\theta_n + \Delta)\}^2 + \{E_0 \sin\theta_0 + E_n \sin(\theta_n + \Delta)\}^2. \tag{4.60}$$

Here the amplitude ratio of the $n$th element to the reference element is

$$k = \frac{E_n}{E_0}. \tag{4.61}$$

Equation 4.60 reduces to the relative power expressed as

$$\begin{aligned} Q \equiv \frac{|\mathbf{E}_T|^2}{E_0^2} &= \{\cos\theta_0 + k\cos(\theta_n + \Delta)\}^2 + \{\sin\theta_0 + k\sin(\theta_0 + \Delta)\}^2, \\ &= 1 + k^2 + 2k\cos\{\theta_0 - (\theta_n + \Delta)\}. \end{aligned} \tag{4.62}$$

That is, the relative power $Q$ varies as a cosine function with the phase $\Delta$. The maximum of $Q$ is provided at $\Delta = \theta_0 - \theta_n$ in Equation 4.62, and $\Delta$ is the phase difference between the reference and the $n$th elements. The difference between the maximum and minimum in $Q$ is given by

$$\begin{aligned} Q_a &= (k+1)^2 - (k-1)^2, \\ &= 4k. \end{aligned} \tag{4.63}$$

Then

$$k = \frac{Q_a}{4}. \tag{4.64}$$

The difference $Q_a$ provides the relative gain between the reference and the $n$th element. Thus, the derivation of the relative gain and relative phase with the REV-method needs to measure the total power $Q$ of two elements by phasing the $n$th element, and to detect (1) phase $\Delta$ at the maximum of $Q$ and (2) difference $Q_a$ between the maximum and minimum of $Q$.

We use a natural radio source as the radiation source. The measurements are performed in the following conditions:

(i) Radio source : the Sun;
(ii) Measurement time : around meridian transit of the Sun;
(iii) Reference element : No. 35 and No. 36.

The detector is a square-law detector used for routine observations with the non high-pass mode described in Chapter 2. The measurement time was recorded to compensate for the motion of the Sun. Figure 4.7 shows an example of variation of the total output power, obtained from the combination of the element No. 10 and No. 35 by controlling a 5-bit phase shifter of No. 10. The power level is normalized by 2. The abscissa is the phase corresponding to the bit of the 5-bit phase shifter in the No. 10 element. The solid line is the theoretically predicted cosine-curve which is a least-squares fit to the measurement. The standard deviation of the differences between the measurements and least-squares fit cosine-curves was 3.8% for the average amplitude of the cosine-curve. This means that the variation of the total output power in phasing the element is consistent with the theoretical cosine-curve. In the combination of the element No. 10 and No. 35, the



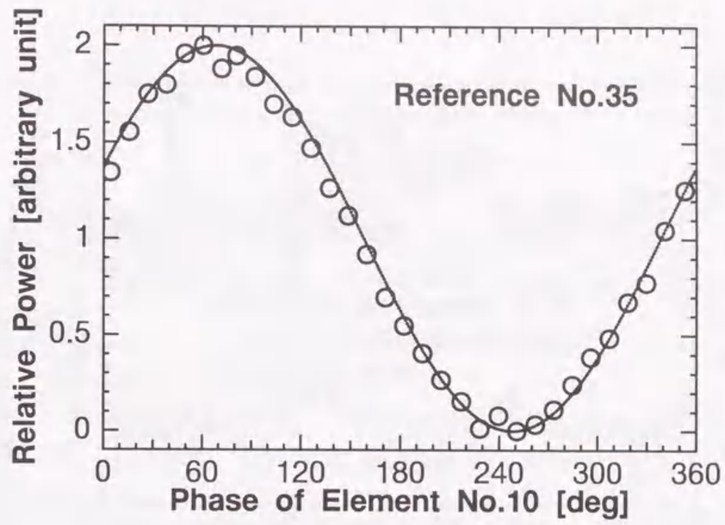


Figure 4.7: Variation of output power obtained by receiving the sun with element-antennas of No. 10 and No. 35. The abscissa is the phase corresponding to the bit of the 5-bit phase shifter in the No. 10 element. The solid line is the calculated sine-curve.

maximum of the cosine-curve was obtained at the phase of 68° in the element No. 10. Thus, the phase at the maximum point is calculated for all the combinations between the reference and the other elements. The relative phase of each channel is obtained after compensating the diurnal variation of the Sun. The relative gain is obtained from the amplitude ratio of the cosine-curves.

### 4.5.2 Comparison of the Results

Figures 4.8 and 4.9 show comparisons of the relative phase and relative gain between the loop- and REV-methods. The double-circle, diamond, and single-circle represent the loop-method, the REV-method, and differences between the two methods, respectively. Figure 4.8 tells us that phase distributions obtained by the both methods are in agreement with each other. The standard deviation of phase differences between

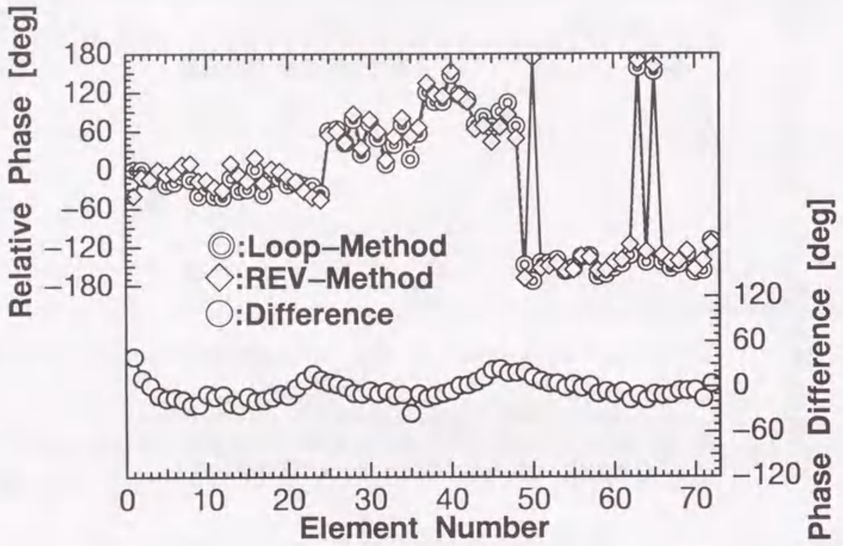


Figure 4.8: Comparison of the relative phase between the loop- and REV-methods. The double circle, diamond, and single circle represent the loop-method, REV-method, and differences between their two methods, respectively.

the both methods is 12.3°. The wavy distribution of the phase difference is due to phase errors which are caused by the sag of the stainless wires among the supporting frames of the main reflector. The phase error estimated from the sag of the stainless wires is 11.5° as discussed in Chapter 3, and this is comparable to the phase difference between both methods.

Comparison of the relative gains (Figure 4.9) indicates that gain distributions are very similar between both methods in the elements from No. 3 to No. 68, while there are large differences for the elements around both ends of the phased array. The both end elements have edge effect of the main reflector. The edge effect decreases the gain of the end elements, but it is not detectable with the loop-method. This gain reduction at the edge works as a taper of the aperture distribution, and modifies the beam pattern. The



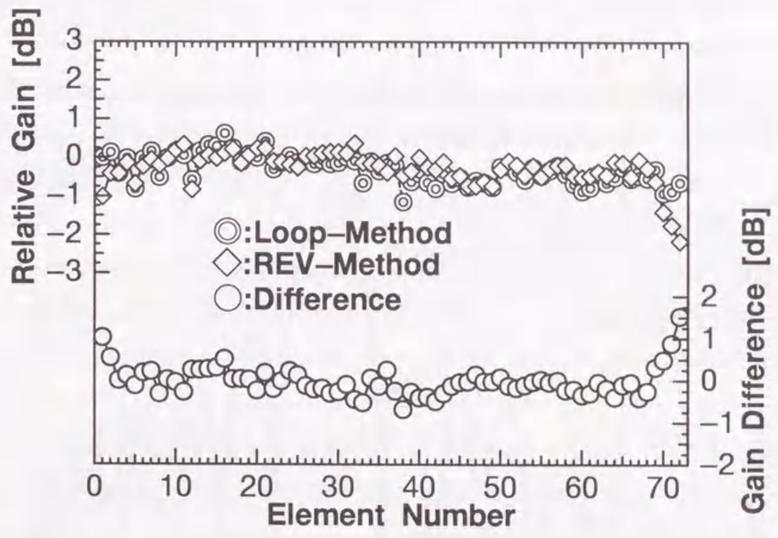


Figure 4.9: Comparison of the relative gain between the loop- and REV-methods. The marks represent the same meanings as the phase comparison.

effect before the pre-amplifier units for the relative phase and relative gain is primarily caused by the main reflector. The standard deviation of gain differences between both methods is 0.23 dB for the elements from No. 3 to No. 68.

## 4.6 Calibration Verification

We evaluate the loop-method by measuring a far-field pattern in azimuth which the phased array of the asymmetric parabolic cylinder antenna contributes to. The power pattern in the azimuth direction is measured by transit of a celestial radio source 3C144 [11] (Crab Nebula) which is regarded as a point source for the beam-width of the antenna.

Figure 4.10 shows the power patterns of the asymmetric parabolic cylinder

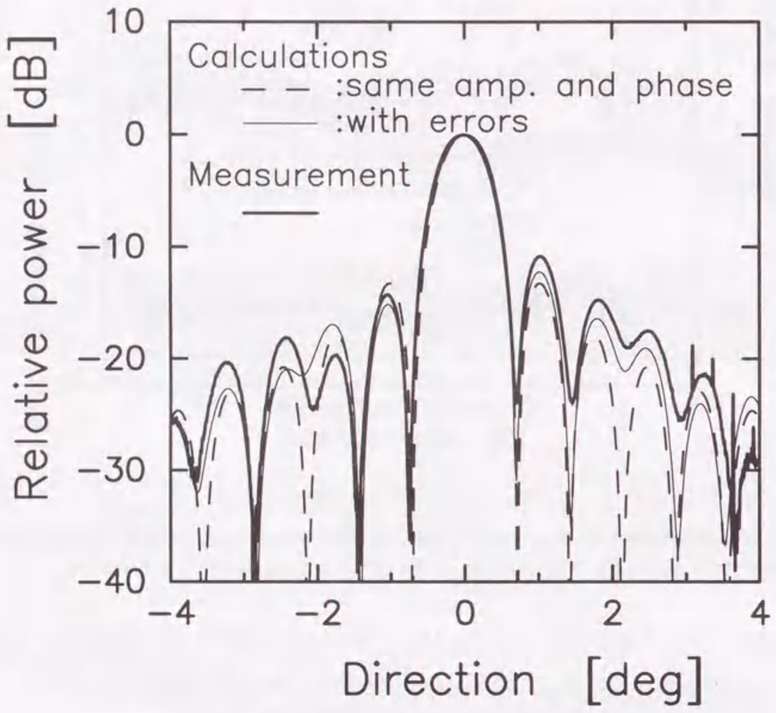


Figure 4.10: Power patterns of the asymmetric parabolic cylinder antenna in azimuth. The thick solid line is the measurement using a celestial object. The dashed line is the calculation in the assumption that each array-element is set to the same amplitude and phase. The thin solid line is also the calculation including the gain and phase differences deduced from the comparison between the loop- and REV-methods.



antenna in azimuth. The thick line indicates the measurement in which the gain and phase of the phased array are calibrated with the loop-method. The measurement was obtained by a drift scan of 3C144 with a fixed beam at the culmination. The dashed and thin lines are the power patterns theoretically calculated for a 144 half-wavelength dipole-array. In the dashed line, each element has the equal (ideal) amplitude and phase. In the thin line, the gain and phase differences deduced from the comparison between the loop- and REV-methods in Section 4.5.2 are offset for each element as errors which are caused by the antenna structure but are not calibrated with the loop-method. The 3 dB beam-width of the measured directivity is 0.7° which is almost consistent with the calculated values. Comparing the measured pattern with the calculated one including the errors, the directivities are very similar throughout the direction, though a level disagreement between the second and third sidelobes exists in the east side (minus side in the horizontal axis of Figure 4.10). The sidelobes locate at similar directions each other, but the sidelobe levels do not agree so well as those in the former comparison. Accordingly, the gain and phase differences between the loop- and REV-methods are in a reasonable range. The gain loss due to the reflector surface warp is small and comparable to the decrease of the aperture efficiency estimated in the design of the antenna [1]. Once the relative gain and relative phase of the total system are measured with the REV-method, the loop-method is convenient and enough for the system check. This is because long term changes due to surface errors on the reflector are almost negligible for the metric wavelength antenna.

## 4.7 Summary

We have discussed three methods used to measure gain and phase of each channel in the phased array system installed in an asymmetric parabolic cylinder antenna. In the reflection-method, a calibration test signal is used to measure the power level at the opened or shorted terminal where the pre-amplifier unit is located. The absolute gain is measurable within the accuracy of 0.1 dB. However, the reflection-method is not applicable to the calibration for all the channels in the large phased array system.

The loop-method measures the relative gain and relative phase of each chan-

nel, and can calibrate them to make uniform distributions within quantum errors of the variable attenuators and phase shifters. The phased array was calibrated within standard deviations of 0.1dB for gain and 3.2° for phase, respectively. The ambiguity $\pi$ in the relative phase is eliminated by using a method that the line-length between adjacent branches is set within the range of 180°.

The REV-method, making a two-element interferometer in the phased array, is used to measure the gain and phase for the whole route including the element-antenna and structure around the phased array. We can estimate the gain drop of the end elements due to the edge effect and the phase error due to the deformation of the reflectors. The power pattern examinations in the azimuth direction verify that the calibrations with the loop- and REV-methods are valid for the phased array system. The total system is once measured with the REV-method, the loop-method is convenient and sufficient for the system check.

# Bibliography


[1] K. Asai, M. Kojima, H. Misawa, Y. Ishida, K. Maruyama, N. Yoshimi, M. Wakasa, and M. Karakida, Design of an asymmetric parabolic cylinder antenna with high aperture efficiency, *Transactions of the Institute of Electronics, Information and Communication Engineers*, **J78-B-II**, No. 3, pp.102–109, 1995.

[2] S. Mano, and T. Katagi, A method for measuring amplitude and phase of each radiating element of a phased array antenna, *Transactions of the Institute of Electronics, Information and Communication Engineers*, **J65-B**, No. 5, pp.555–560, 1982.

[3] S. Fukao, T. Sato, T. Tsuda, S. Kato, K. Wakasugi, and T. Makihira, The MU radar with an active phased array system, 1.Antenna and power amplifiers, *Radio Science*, **20**, No. 6, pp.1155–1168, 1985.

[4] P.-S. Kildal, Radiation characteristics of the EISCAT VHF parabolic cylindrical reflector antenna, *IEEE Transactions on Antennas and Propagation*, **AP-32**, No. 6, pp.541–552, 1984.

[5] W. A. Coles, R. G. Frehlich, and M. Kojima, Design of a 74MHz antenna for radio astronomy, *Proceedings of the IEEE*, **82**, pp.697–704, 1994.

[6] A. G. Little, and R. Payne-Scott, The position and movement on the solar disk of sources of radiation at a frequency of 97 Mc/s. (I. Equipment), *Australian Journal of Science Research*, **A4**, pp.489–507, 1951.

[7] G. Swarup, and K. S. Yang, Phase adjustment of large antennas, *I.R.E. Transactions on Antennas and Propagation*, **AP-9**, pp.75–81, 1961.

[8] M. Morimoto, and N. R. Labrum, The phase and gain calibration system, *Proceedings of the Institution of Radio and Electronics Engineers Australia*, **28**, No. 9, pp.352–360, 1967.

[9] M. Kojima, Y. Ishida, K. Maruyama, and T. Kakinuma, An observation system of interplanetary scintillation at UHF, Proceedings of the Research Institution of Atmospherics, Nagoya University, **29**, pp.61–83, 1982.

[10] K. Asai, M. Kojima, Y. Ishida, K. Maruyama, N. Yoshimi, H. Misawa, and K. Miyasato, Calibration of Gain and Phase on the Phased Array System Installed in a Radio Telescope, *Transactions of the Institute of Electronics, Information and Communication Engineers*, **J79-B-II**, No. 12, pp.994–1002, 1996.

[11] J. D. Kraus, *Radio Astronomy (2nd edition)*, pp.8.81–8.83, Cygnus-Quasar Books (1986).

# Chapter 5

# Heliospheric Tomography using Interplanetary Scintillation Data

The development and improvement of the UHF radio telescopes have been conducted as an upgrade project so that one can measure a large number of IPS radio sources. This has made it possible to study the solar wind with better spatial and temporal resolution. Here the observational results are described. From IPS data of the Solar-Terrestrial Environment Laboratory (STELab) we derive relation between solar wind speed and electron density fluctuations, which is important for the solar wind study.

## 5.1 Computer Assisted Tomography

Interplanetary scintillation (IPS) is a useful means to measure global structure of the solar wind in regions where *in situ* measurements are difficult. However, the IPS measurements provide solar wind properties biased by line of sight integration through the three-dimensional structured solar wind, which in particular leads to underestimation of the velocity of fast solar wind from a polar coronal hole. So we have to address the problem of bias involved in the IPS data. Several attempts have been made to remove the bias from the IPS observations. Grall et al. [1] determined the best fit solar wind distribution along a line of sight by model-fitting the shape of a cross-correlation function. Kakinuma et al. [2] optimized a latitudinal speed distribution using a model-fitting method. We have developed a method which uses a computer assisted tomography (CAT) to obtain unbiased longitudinal and latitudinal distributions of the wind speed and electron

density fluctuations [3].

The CAT is generally used to reconstruct distribution of an object by combining many projection images from multi-direction measurement, and is applied to the various fields such as medical electric engineering, measurements of Earth's interior structure, plasma diagnostics, and so on. The well-known application is to probe the human body as a non-invasive way, reconstructing its internal structure in three dimensions [4]. In the case of the human body, X-ray is used for probing the medium. One of the earliest works to recover the true distribution from the observations is in solar radio astronomy [5]. The CAT techniques have extended its application to studies of accretion disks [6] and binary stars [7] in astrophysics, acoustic sounding in oceanography [8], seismic studies in geology [9], and refractometric sounding in atmospheric modeling [10].

In coronal and heliospheric physics there are numerous attempts to determine the three dimensional structures of coronal mass ejections (CMEs), coronal streamers, and interplanetary medium. Jackson et al. [11] observed coronal mass ejections from the multiple perspectives with the Solwind coronagraph and the solar maximum mission (SMM). Jackson and Froehling [12] performed a CAT analysis of CMEs on the Solwind coronagraph and Helios spacecraft photometer observations to reconstruct its three dimensional density distribution. Coronal tomography has been made by Zidowitz et al. [13] using solar rotation to reconstruct coronal densities from Mark III coronagraph observations. Jackson et al. [14] compared the density fluctuation distribution of the solar wind, reconstructed from Cambridge IPS index data using the CAT technique, with in situ observations of the IMP spacecraft.

In general, if perspective views from many different directions are available for an object, the resolution of its three dimensional structure becomes fine. Heliospheric tomography combines information from a large number of IPS radio sources to construct three-dimensional views of the interplanetary medium which the lines of sight have traversed. The following conditions make it possible to apply the CAT to our IPS analysis. The IPS observation system of STELab measures more than 30 IPS sources per day covering various elongation angles, and thus a thousand lines of sight are available in one



solar rotation period. Both solar rotation and solar wind outward motion give perspective views of three-dimensional solar wind structure. Iterative tomographic technique can be used to produce a three-dimensional heliospheric model of the solar wind speed and density fluctuations.

The intensity scintillation is sensitive to electron density fluctuations on the scales smaller than 100 km whose information is difficult to be extracted from *in situ* spacecraft measurements because of low sampling rates. We concentrate on relationship between wind speed and electron density fluctuations with scale sizes of the order of 100 km at heliocentric distances of 0.3 to 0.8 AU. We make a direct comparison of wind speed and electron density fluctuations measured by the IPS method at the STELab. Important issues addressed in these studies are the origin of the density fluctuations, and their evolution with radial propagation.

## 5.2 Observations

The quantities derived from our IPS observations are the intensity of a radio source and its temporal scintillation. The scintillation index and IPS velocity (solar wind velocity deduced from the IPS observation) are obtained by analyzing these data. We can use the scintillation index to obtain information on the electron density fluctuations. For the CAT analysis, information on both velocity and electron density fluctuations is necessary because these parameters are coupled in the IPS observations.

### 5.2.1 Scintillation Index

The scintillation index is given by a root mean square (r.m.s.) of radio intensity fluctuations $\Delta I(t)$ divided by a mean intensity [15]. The r.m.s. of the intensity fluctuations due to IPS is equivalent to a square root of a total integral of the IPS power spectrum. Hence, the scintillation index $m$ is estimated by using the relation,

$$m^2 = \frac{\langle \Delta I(t)^2 \rangle}{\langle I \rangle^2} \tag{5.1}$$

$$= \frac{\int_0^{f_c} (P(f) - W_{noise}) df}{\langle I \rangle^2}. \tag{5.2}$$

Here, $P(f)$ is the scintillation power at the temporal frequency $f$. $f_c$ is the cut-off frequency where the scintillation power becomes equal to a white noise level in the high frequency region, while the power spectrum reaches a finite level in the low frequency region because of the Fresnel filtering effect [16]. $W_{noise}$ is the white noise level, and $\langle I \rangle$ is the mean source intensity. The angular brackets denote an ensemble average. The measurement of each source is made for about 10 minutes, as shown in Figure 5.1. As described in Chapter 2, the source tracking is done every 30 seconds. The first 30-second interval and the last two 30-second intervals are taken for off-source measurements which give a reference zero level including sky-background radiation, ground radiation, receiver noise, and so on. In the first interval and the former of the last two intervals, the antenna beam points the west side of the source, but in the last interval the east side. The interval between the off-source measurements is taken for on-source measurements. The mean intensity of the observed source is estimated from the difference between the mean intensity levels of on- and off-source modes.

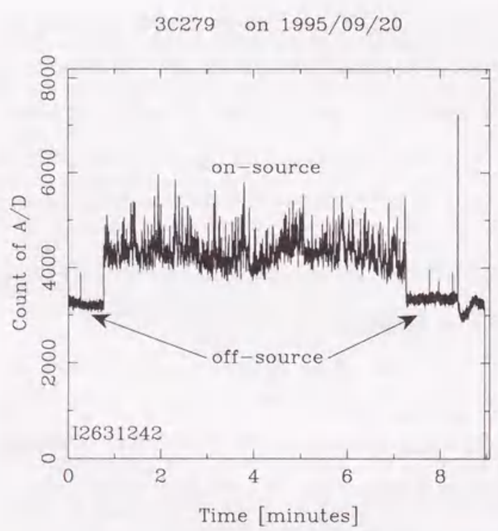


Figure 5.1: Scintillation signal received for the IPS radio source 3C279 on September 20, 1995. The radio source is located at a solar distance of 70 $R_\odot$ and a heliographic latitude of 0°. The first 30 seconds and the last 1 minutes are off-source measurements.



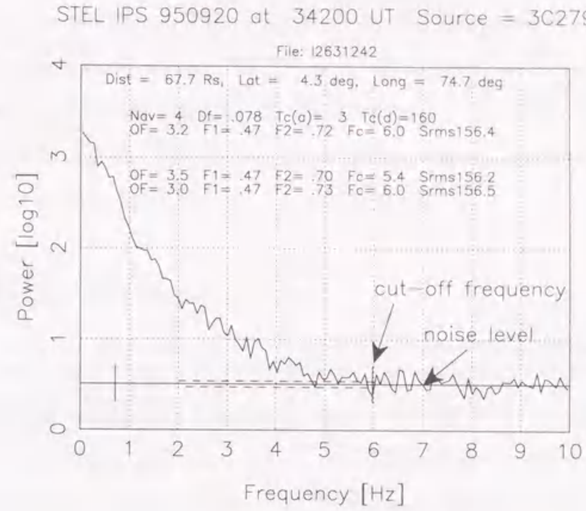


Figure 5.2: Power spectrum of interplanetary scintillation. The area above the noise level indicates scintillation power. The noise level is determined with the power level in the frequency range of 8 to 10 Hz. The cut-off frequency is given as the second point below the noise level. The power level of low frequencies below 0.016 Hz is extrapolated by the above power levels.

Figure 5.2 shows IPS power spectrum which is derived from the intensity fluctuations in the on-source mode after manually eliminating noisy spikes from the raw data (Figure 5.1). The Fourier transform is performed with every $2^{10}$ sampling data. The power spectrum has a frequency resolution of 0.020 Hz. The lowest frequency component in the spectrum could have interfered with effects caused by interstellar scintillations and ionospheric scintillations. Hence, the first eight points of the spectrum are extrapolated by fitting a second-degree polynomial to the next forty points. In the IPS power spectrum of Figure 5.2 we take the running mean of four data for visually judging its overall quality. The noise level is determined with the power level at the frequency range of 8 to 10 Hz.

As an example, Figure 5.3 shows a data plot of scintillation index measurements for the radio source 3C279. The abscissa is the distance of the closest point to the Sun on the line of sight. The vertical bars indicate errors estimated from the white noise

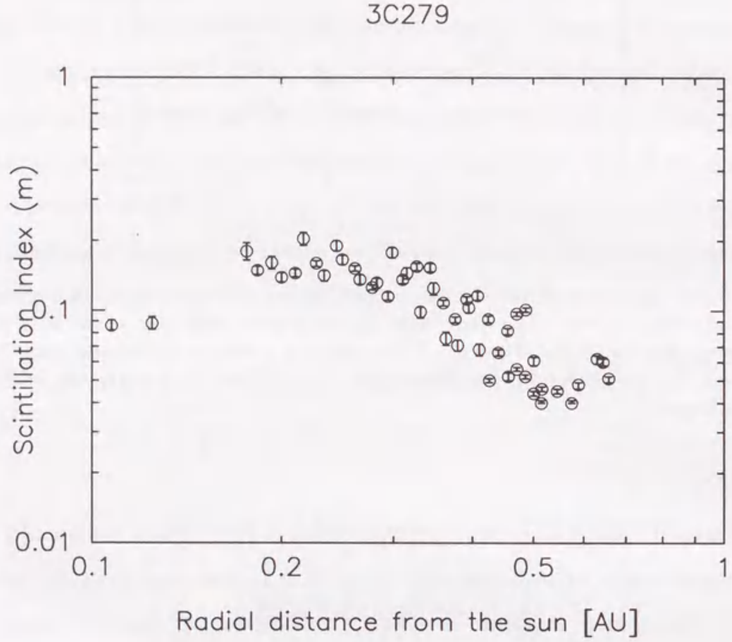


Figure 5.3: Scintillation index observed for the IPS radio source 3C279. Abscissa is the distance of the closest point to the Sun on a line of sight. The vertical bars indicate errors estimated from the white noise level and mean source intensity.



level and mean source intensity. As the radio source approaches to the Sun, the electron density fluctuations increase and the scintillation index then goes up. The scintillation index reaches a peak value at a certain distance, and for any source with a finite size it then decreases inside the distance [15, 16]. The turnover for 327 MHz occurs at a distance around 0.2 AU in the transition from weak to strong scattering where the r.m.s. phase fluctuations start to exceed 1 rad [17].

### 5.2.2 Velocity Estimation

When the spatial diffraction pattern drifts past the observers, the temporal intensity scintillations are received at each station. Let us assume that the diffraction pattern drifts with IPS velocity $\mathbf{V}$ and its structure does not change within a distance between IPS observation sites. We also assume that there are an infinite number of antennas on the observer's plane. Correlations among intensity fluctuation signals from each receiver provide the spatial cross-correlation functions of the two-dimensional diffraction pattern. Since we require statistical structure for the diffraction patterns, we analyze the size and anisotropy for spatial spectrum of the diffraction pattern. If the spatial cross-correlation function approximates to elliptical symmetry, the two-dimensional cross-correlation function is given by [18]

$$\rho(\mathbf{r},\tau) = \rho\{(\mathbf{r}^t[Q]\mathbf{r})/s_o^2,\tau\}, \tag{5.3}$$

in the coordinate moving with $\mathbf{V}$. Here the associated matrix $[Q]$ consists of quadratic coefficients characterized by an axial ratio $\gamma$ of the ellipse and an orientation angle $\beta$ of the major axis [19],

$$[Q] = \begin{pmatrix} A & H \\ H & B \end{pmatrix}, \tag{5.4}$$

$$= \begin{pmatrix} \cos^2\beta + \gamma^2\sin\beta & (1-\gamma^2)\sin\beta\cos\beta \\ (1-\gamma^2)\sin\beta\cos\beta & \sin^2\beta + \gamma^2\cos^2\beta \end{pmatrix}. \tag{5.5}$$

and $s_o$ is a characteristic scale length of the diffraction pattern. Then on the observer's frame,

$$\rho_o(\mathbf{r},\tau) = \rho\{((\mathbf{r}-\mathbf{V}\tau)^t[Q](\mathbf{r}-\mathbf{V}\tau))/s_o^2,\tau\}. \tag{5.6}$$

This cross-correlation function in Equation 5.6 takes the maximum value for a time lag $\tau_m$ [22],

$$\tau_m = (\mathbf{q} \cdot \mathbf{r}), \tag{5.7}$$

$$\mathbf{q} = \frac{[Q]\mathbf{V}}{\mathbf{V}^t[Q]\mathbf{V}}, \tag{5.8}$$

where $\mathbf{r} = (x, y)$ is the baseline vector between antennas.

We derive four parameters of the velocity $\mathbf{V}$ (magnitude and direction), the axial ratio $\gamma$, and the orientation angle $\beta$ from the correlation analysis. An infinite number of antennas are not practically available for the observations, but we can obtain the cross-correlation functions for six baselines among four stations. The six-baseline observations produce six time lags $\tau_{mi}(i$=1,2,$\cdots$,6), but two of them are independent at least. We assume a radial flow of the solar wind whose assumption has been verified outside 0.3 AU [20, 21]. This reduces the required parameters to $V = |\mathbf{V}|$ and $H/A$. Thus, Equation 5.9 is rewritten as

$$\tau_{mi} = \frac{x_i + \frac{H}{A} y_i}{V}. \tag{5.9}$$

$V$ and $H/A$ are calculated by using the two time lags, though $\gamma$ and $\beta$ are not observed separately. Fortunately, the parameter $H/A$ determines the polarity of the pattern orientation angle with respect to the flow direction which was already assumed to be radial. There are two unknown parameters in Equation 5.9, but six observable time lags. The redundancy can produce the estimation error of the velocity. Actually, we take the time lag value either of the midpoint at half level or of the peak of the cross-correlation function.

## 5.3 IPS Model

### 5.3.1 Line of Sight Integration

In the Born approximation, generally used in the analysis of IPS observations in weak scattering conditions [23], the extended scattering medium is assumed to consist of multiple thin scattering layers perpendicular to the line of sight. In this approximation, an observed quantity is represented by a weighted sum of contributions from each layer. Here



the IPS model is described for the CAT analysis to reconstruct the solar wind structure, based on the Born approximation.

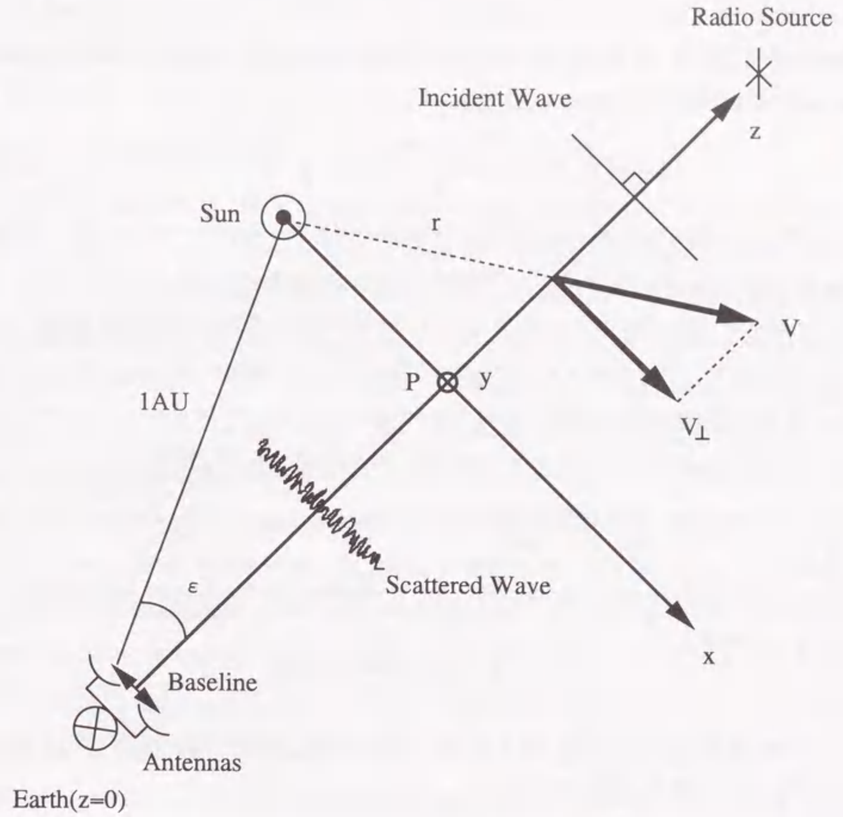


Figure 5.4: Geometry of IPS observations.

The geometry of IPS observations is shown in Figure 5.4, in which the $x$ coordinate is taken parallel to the solar wind velocity component $V_\perp(z)$ perpendicular to the line of sight, that is, $x$ axis is parallel to the projected direction on the observer's plane, and $z$ axis is along the line of sight from the Earth to the radio source. The IPS measures a weighted average along the line of sight in the solar wind parameters. If each

thin screen layer is identical, the spatial spectrum of a diffraction pattern $G(\kappa_x, \kappa_y)$ in the local rest frame of the solar wind can be represented as

$$G(\kappa_x, \kappa_y) \propto F(\kappa)\Phi_{Ne}(\kappa_x, \kappa_y, \kappa_z = 0), \tag{5.10}$$

where $\Phi_{Ne}(\kappa_x, \kappa_y, \kappa_z = 0)$ is the spectrum of the refractive index or electron density fluctuations, and $F(\kappa)$ is given by [24]

$$F(\kappa) = \int_0^\infty \delta N_e^2(z) \sin^2\left(\frac{\kappa^2 \lambda z}{4\pi}\right) \exp\left(-\frac{\theta_0^2 \kappa^2 z^2}{2}\right) dz. \tag{5.11}$$

Here, $\delta N_e(z)$ is the distribution function representing the electron density fluctuations along the line of sight, which has an inverse square dependence on the distance from the Sun. $\kappa$ the wavenumber ($\kappa^2 = \kappa_x^2 + \kappa_y^2$), $z$ the distance of the scattering region from an observer, and $\lambda$ the radio wavelength. When the diffraction patterns move with a speed $V_\perp$ over hypothetical observers at two separate stations $(0,0)$ and $(x,y)$, the spatial spectrum $G(\kappa_x, \kappa_y)$ is observed as a temporal cross-spectrum $P_c(f)$ [25],

$$P_c(f) = \int_{-\infty}^{\infty} \frac{\exp(-i2\pi f x/V_\perp)}{2\pi V_\perp} G(-2\pi f/V_\perp, \kappa_y) \exp(i\kappa_y y) d\kappa_y. \tag{5.12}$$

The temporal cross-correlation function $C(t)$ is obtained by the Fourier transform of the cross-spectrum $P_c(f)$,

$$C(t) = \frac{\int_{-\infty}^{\infty} P_c(f) \exp(i2\pi f t) df}{m^2}. \tag{5.13}$$

The square of the scintillation index $m^2$ is proportional to the integral of the weighting function $\omega(z)$ along the line of sight,

$$m^2 \propto \int_0^\infty \omega(z) dz, \tag{5.14}$$

$$\omega(z) = 2\pi\delta N_e^2(z) \int_0^\infty d\kappa \sin^2\left(\frac{\kappa^2 \lambda z}{4\pi}\right) \exp\left(-\frac{\theta_0^2 \kappa^2 z^2}{2}\right) \kappa^{1-\alpha}. \tag{5.15}$$

The squared sine term in the weighting function $\omega(z)$ is the Fresnel propagation filter, which cuts off contributions near the Earth on the line of sight and limits the outer-scale size of the fluctuations. The exponential term is a filtering function due to the finite radio source size $\theta_0$, which suppresses contributions at farther distances than several AU from the Earth. The wavelength $\lambda$ is 0.917 m (327 MHz) in our IPS observations, so the IPS data inside 0.3 AU where the wave propagation might be in strong scattering



are excluded from our analysis. We assumed a power-law spectrum $q^{-\alpha}$ for the electron density fluctuations. We use $\alpha = 3.3$, because the power-law exponent, which depends on the wind speed and the radial distance from the Sun, is in the range of 2.9 to 4.1 for spatial scales sensitive to the IPS [26, 27, 28]. Actually, the results do not significantly depend on the spectral index. The half angular source size $\theta_0$ is assumed to be 0.1 arcsecond for all IPS sources. The integrations are performed from 0 (at Earth) to 2 AU for $z$, and from 0 to $7.7/(\theta_0 z)$ for $\kappa$.

Variations of the weighting function with the exponent $\alpha$ and elongation $\varepsilon$ are calculated by using Equation 5.15. Figure 5.5 shows the weighting function for the exponent $\alpha$ varying between 2.8 and 3.6 at an elongation of 30°. The weighting function is almost independent of the exponent $\alpha$, though the change of $\alpha$ makes small shift of the entire distribution. Figure 5.6 shows the weighting function with the elongation varying between 10° and 60°. When the elongation is small, the contribution to the IPS is centralized on the point P which is the closest point from the Sun on the line of sight. While, the large elongations give the broad contribution to the IPS over the line of sight and a peak of the weighting function approaches to the Earth. Although we normalized the maximum values to 1, the weighting function actually become small at large elongations because the lines of sight are far from the Sun.

A simpler method for the line of sight integration is to integrate the cross-correlation function on each screen layer instead of the cross-spectrum in Equation 5.13. The cross-correlation function between two hypothetical stations at $(0,0)$ and $(x,0)$ is given by

$$C(x,\tau) = \frac{\int_0^\infty \omega(z) g(x,\tau,z) dz}{\int_0^\infty \omega(z) dz}, \tag{5.16}$$

$$g(x,\tau,z) = \exp\left\{-\left(\frac{x - V_\perp(z)\tau}{s_o}\right)^2\right\}, \tag{5.17}$$

where $g(x,\tau,z)$ is a cross-correlation function on the single screen, and $s_o$ is the characteristic scale length of the diffraction pattern. The IPS speed ($V_{cal}$) is then calculated from a time lag derived from the cross-correlation function $C(x,\tau)$. This cross-correlation analysis method is also used to estimate an observed IPS speed $V_{obs}$ from daily IPS obser-

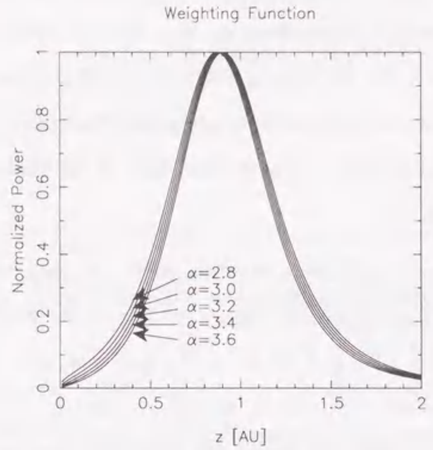


Figure 5.5: Weighting function vs. distance $z$ from the Earth with various exponents $\alpha$.

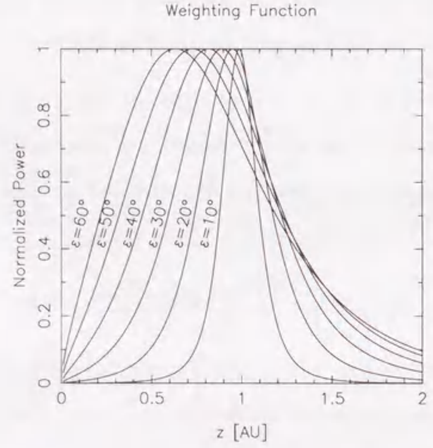


Figure 5.6: Weighting function vs. distance $z$ from the Earth with various elongations $\varepsilon$. The maximum value is normalized to 1.



vations at STELab. To reduce the computation time, we use a more simplified method which is to integrate speed itself,

$$V_{cal} = \int_0^\infty \omega(z) V_\perp(z) dz. \tag{5.18}$$

Kojima et al. [29] examined the speed differences between the cross-correlation analysis using Equation 5.16 and calculation using Equation 5.18 for a solar wind structure typical for the solar minimum phase, and obtained an average discrepancy of 11 km s$^{-1}$.

### 5.3.2 Relative Electron Density Fluctuations

The electron density fluctuation level is assumed to decrease as the inverse square of heliocentric distance,

$$\delta N_e(z) \propto r^{-2}(z) \delta N'_e(z), \tag{5.19}$$

where $r(z)$ is the heliocentric distance along the line of sight, and $\delta N'_e(z)$ is the relative electron density fluctuations. $\delta N'_e(z)$ depends on the solar wind structure (e.g., the latitudinal velocity profile), but is assumed to be independent of heliocentric distance between 0.3 and 0.8 AU. The radial dependence of the electron density fluctuations can be obtained from the analytical solution of the IPS line of sight integral; it has been shown that the power-law index of $r$ for $\delta N_e$ is in the range of 2.0 to 2.2 [30, 31, 15]. The power-law index affects the weighting function, but the effect of varying the index from 2.0 to 2.2 is negligible in the CAT analysis.

The scintillation index depends not only on the level of electron density fluctuations, but also on the radio source size. However, radio source sizes are not known for all sources observed at the STELab. To avoid the source size problem in the analysis, we use a normalized scintillation index, similar to the g-value introduced by the Mullard Radio Astronomy Observatory (Cambridge, England) [32]. The normalized index represents the value of the electron density fluctuations relative to that in a hypothetical solar wind with a radially expanding non-structured flow. If we calculate Equation 5.14 in the hypothetical solar wind, $m = m_o r^{-1.6}$ is obtained for the heliocentric distance dependence of the scintillation index. The magnitude $m_o$ is determined by performing the least-squares fit to the data in the elongation range of 30° to 90°. In Figure 5.7 the best-fit of the

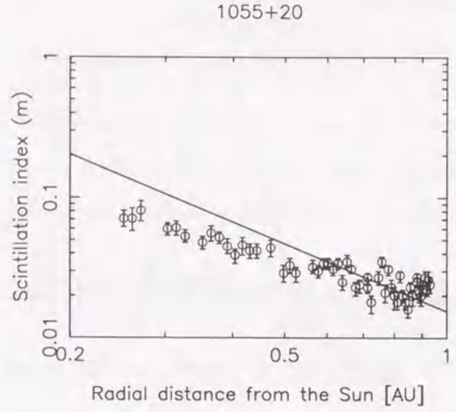


Figure 5.7: Scintillation index observed for IPS radio source 1055+20. The abscissa is the distance of the closest point to the Sun on a line of sight. The vertical bars indicate errors estimated from the white noise level and mean source intensity. The solid line is a power-law form $m \propto r^{-1.6}$ scaled to make the best-fit to the data beyond 0.5 AU.

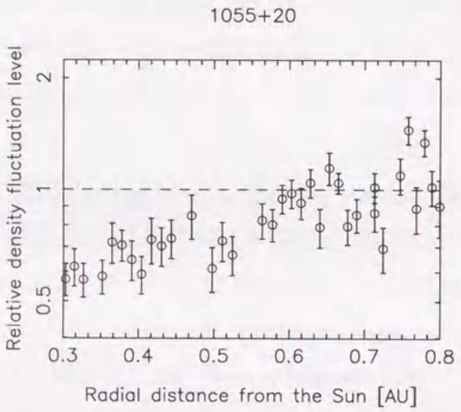


Figure 5.8: Relative electron density fluctuations deduced from the scintillation index shown in Figure 1. The relative electron density fluctuations are defined as a ratio of the observed scintillation index to that estimated from the best-fit line. The vertical bars are estimation errors based on the errors of the scintillation indices.



power-law form $m \propto r^{-1.6}$ is drawn as a solid line. The deviation of the observed points from the best-fit line for radial distances less than 0.5 AU is attributed to the fact that the radio ray path moves into the polar coronal hole as the radial distance decreases.

Then we define the relative electron density fluctuations $\delta N'_{obs}$ from the scintillation index measurements at an elongation $\varepsilon$ as

$$\delta N'_{obs} = \frac{m(\varepsilon)}{m_s(\varepsilon)}, \tag{5.20}$$

and those from the line of sight integration in the CAT analysis as

$$\delta N'_{cal} = \frac{m}{\sqrt{\int_0^\infty \frac{\omega(z)}{\delta N'_e(z)} dz}}. \tag{5.21}$$

Here, $m(\varepsilon)$ represents the observed scintillation index, and $m_s(\varepsilon)$ is the index value obtained from the least-squares fit line $m = m_o r^{-1.6}$. Figure 5.8 shows the relative electron density fluctuations obtained from the scintillation index measurements of the radio source 1055+20. The vertical bars are estimation errors based on the errors of the scintillation indices in Figure 5.7. The points below 1 for radial distances less than 0.5 AU reflect the deviations from the best-fit line in Figure 5.7. The least-squares fit line does not represent the fast solar wind from high-latitude coronal holes, because most observations in the elongation range where the least-squares fit is performed are at low heliographic latitudes. Therefore, the scintillation indices of fast solar wind are generally below the least-squares fit line, and the fluctuation level takes values smaller than 1.

## 5.4 Reconstruction Algorithm

Using Equations 5.18 and 5.21, the following algorithm is applied to the CAT reconstruction of the solar wind structure from all observed IPS data:

1. Make synoptic maps of the initial distribution of the wind speed and relative electron density fluctuations in Carrington longitude and latitude on a reference sphere at a height of 2.5 $R_\odot$ by mapping back the IPS data. We do this by assigning the observed IPS speed $V_{obs}$ and relative electron density fluctuation level $\delta N'_{obs}$ to the resolution bins which are intersected by the projection of the line of sight on the reference sphere. All

the values assigned to a particular bin are then used to calculate a weighted average for that bin with a weighting function $\omega(z)$ and an estimation error. The same values are assigned to resolution bins within an angular distance of $\pm 5°$ from the projected line of sight. Consequently, the actual spatial resolution on the maps is $10° \times 10°$.

2. Make a three-dimensional model structure of the solar wind by radially expanding the distributions from the reference sphere; then we calculate the line of sight integrals for the speed and relative electron density fluctuation level in this model structure using Equations 5.14, 5.18, 5.19, and 5.21.

3. Compare the values of speed and relative electron density fluctuations calculated by the above integrations with those of the IPS observations, and assign differences of the calculated and observed values to each resolution bin. After this procedure is completed for all the lines of sight, the difference values in each resolution bin are weighted-averaged with a weight factor $\Omega$,

$$\Omega = \exp\left\{-\frac{3 \times (Estimation\ error)}{(Observed\ value)}\right\}\omega(z). \tag{5.22}$$

Then, the values of the speed and density fluctuations in each resolution bin are modified with the difference values.

4. Steps 2 and 3, which together comprise one iteration in the fitting procedure, are repeated until the differences between calculated (line of sight integrated) and observed values have decreased sufficiently.

In Step 1, the total number of mesh points $360 \times 180$ is used for the maps. In Step 2, the line of sight integrations are performed using a step size $dz$=0.05 AU. At that time, if there are resolution bins with no data in them, the data are interpolated from neighboring bins. However, if there are bins which do not have more than three line-of-sight contributions, the data of those bins are removed in the next iteration and are shown in the synoptic maps as white areas.

We use several assumptions in the reconstruction algorithm. In mapping back the IPS data onto the reference sphere of 2.5 $R_\odot$ and expanding the distributions to make the three-dimensional solar wind structure, we assume that the solar wind flows out radially at constant speed. In addition, we ignore stream-stream interactions, such as the merging of high-speed wind overtaking low-speed wind, mass accumulation at the interaction region, and rarefaction behind the high-speed wind. However, these assumptions do not have a significant impact on the results from our CAT analysis, because the solar wind speed structure during the period analyzed is almost flat and parallel to the equator. Furthermore, we assume that the solar wind structure is stable during the observation period.



## 5.5 Data

We use the IPS data obtained with the IPS observation system at the STELab, which consists of four separated antennas operated at a frequency of 327 MHz [33]. In the period from September to October in 1995 (Carrington rotations 1900 and 1901), we made simultaneous observations of velocity and scintillation index. The velocity is estimated by cross-correlation analysis [25, 34] between the IPS signals received at the separated antennas. The analysis procedure has been described in detail in Section 5.2.2. The scintillation index is estimated using Equation 5.2. The shape of the IPS power spectrum is used to judge the quality of the data by eye; noisy data are excluded from the CAT analysis.

We analyze the global structure of the solar wind in the period between September 7 and October 29 in 1995 when the solar wind structure was stable and simple. Observed speeds above 900 km $s^{-1}$ are excluded from the analysis, because they might be related to transient phenomena such as coronal mass ejections. For the same reason we exclude the observed relative electron density fluctuations larger than 1.6. In addition, relative electron density fluctuations less than 0.4 are discarded because these are considered unrealistic. The excluded data constitute 4% of the total and do not change the global structure. We only use data observed between elongations 17° and 53°, i.e. in the weak scattering region, based on the result that the IPS at a frequency of 327 MHz saturates at an elongation of 12° in the equatorial zone and at 7.5° in the polar regions during solar minimum [15]. We do not deal with IPS sources which are not observed

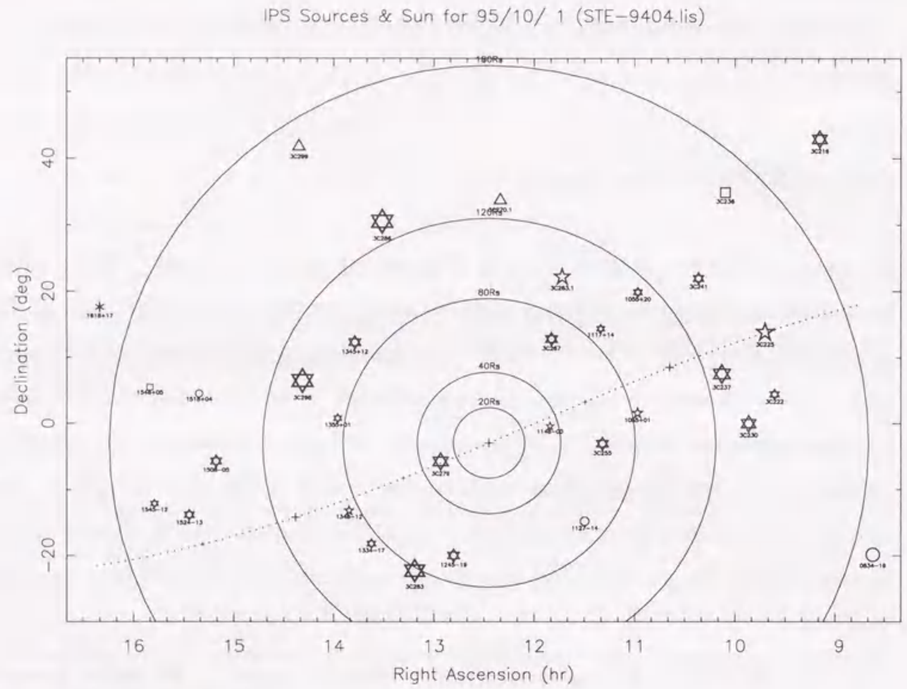


Figure 5.9: Position of the Sun (center of circles) on October $1^{st}$, 1995 projected against the radio sources. The dotted line represents the locus of the Sun. The size of star symbols indicates IPS quality from the past observations. Open-circles, squares, and triangles are unknown sources for the IPS quality, but predicted to be good. The asterisk is unknown at all, and tried for the first time. The solid circles are marked at 20, 40, 80, 120, 180 $R_\odot$ from the position of the Sun.



beyond an elongation 30°, because the least-squares fit of the distance dependence of scintillation index is performed in the elongation range of 30° to 90°. Actually the sources whose closest points to the Sun do not reach inside 0.5 AU might always measure the fast solar wind at the high latitudes, so we carefully made the data reduction for these kinds of sources. After all the data selections, a total number of 472 data during two Carrington rotations 1900 and 1901 are left to be used for the CAT analysis. The Sun's daily position in right ascension and declination is plotted in Figure 5.9 projected against IPS radio sources for the observation period.

## 5.6 Results

Figure 5.10 shows solar wind distribution maps on a reference sphere at 2.5 $R_\odot$ of (a) solar wind speed and (b) relative electron density fluctuations made at Step 1 of the reconstruction algorithm, which are an initial models before the CAT reconstruction, based on the observed IPS data. The gray scale corresponds to the magnitude of the speed and electron density fluctuations, as shown at the right hand side of the maps. Contours are overlaid on the gray scale to identify the boundary of the variations easily. White areas at the south pole regions indicate that no data are available here, because these regions are at too low elevations to be observable from the site of the STELab Observatory. One can see that the low-speed regions coincide with the location of high-density-fluctuation regions over the equatorial belt, which occupies a latitude range of ±15 to 20°. Reconstructed maps from the CAT analysis are shown in Figure 5.11. These are the results of three iterations (Steps 2 and 3) of the reconstruction algorithm. The regions which do not have more than three line-of-sight contributions are shown as white. It is clear that high-speeds around 800 km $s^{-1}$ are retrieved at the high-latitudes, and a sharp speed gradient is reconstructed at the boundary between low-speed and high-speed regions. Although there are some structures at middle latitudes in the map of the relative electron density fluctuations, the contrast between low and high fluctuation regions has become sharper.

To test the quality of the CAT reconstruction we compared the actual IPS

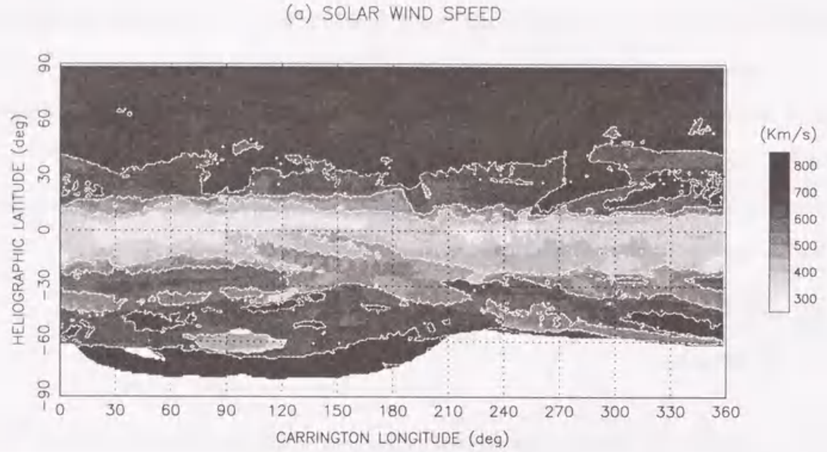


Figure 5.10: The initial solar wind models for the CAT analysis, based on IPS data observed at the STELab from September 7 to October 29, 1995, corresponding to Carrington rotations 1900 and 1901; (a) speed, and (b) relative electron density fluctuations. The maps are made using Step 1 of the reconstruction algorithm.



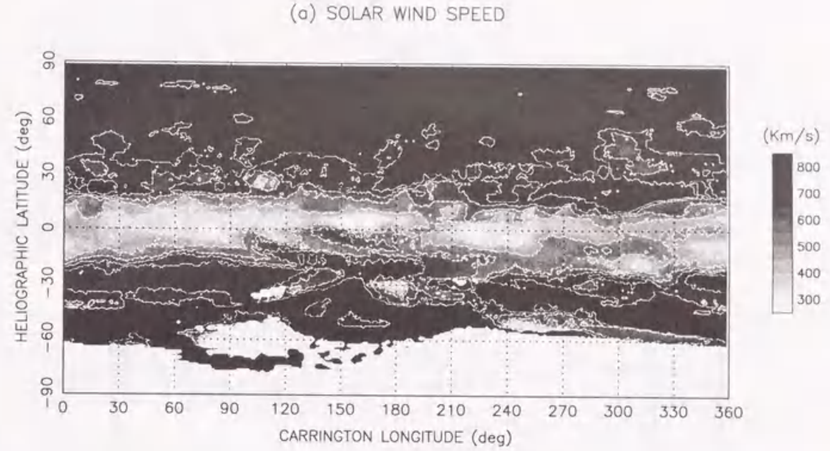


Figure 5.11: The reconstructed results from the CAT analysis for the same period as in Figure 5.10; (a) speed, and (b) relative electron density fluctuations. The maps are made iterating Step 2 to 3 of the reconstruction algorithm.

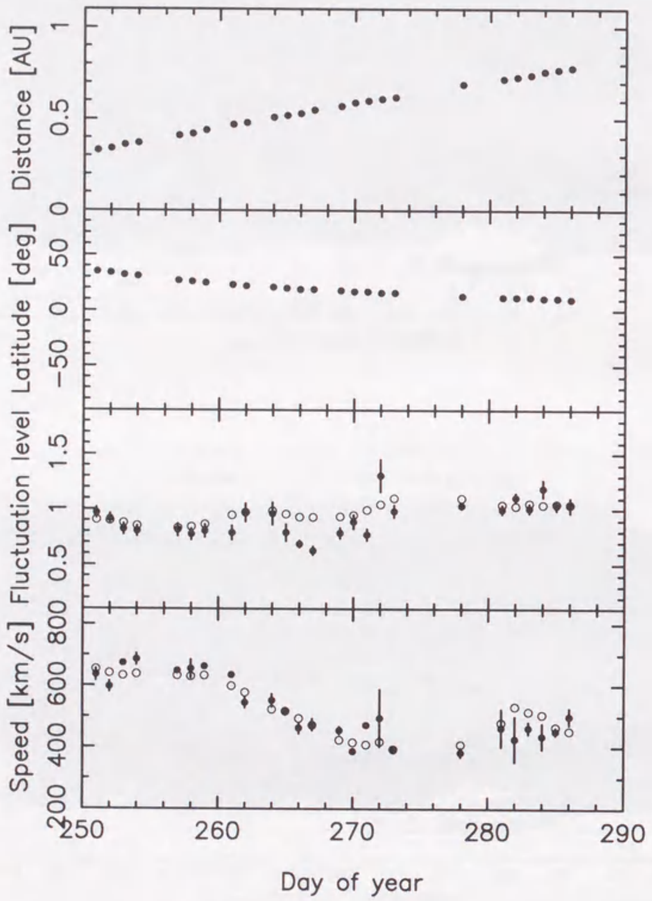


Figure 5.12: Comparison between observed and line of sight integrated IPS values of speed and relative electron density fluctuations for radio source 3C241. Line of sight integrations were made in the reconstructed solar wind. The observations are shown by dots and line of sight integrated values are shown by open circles.



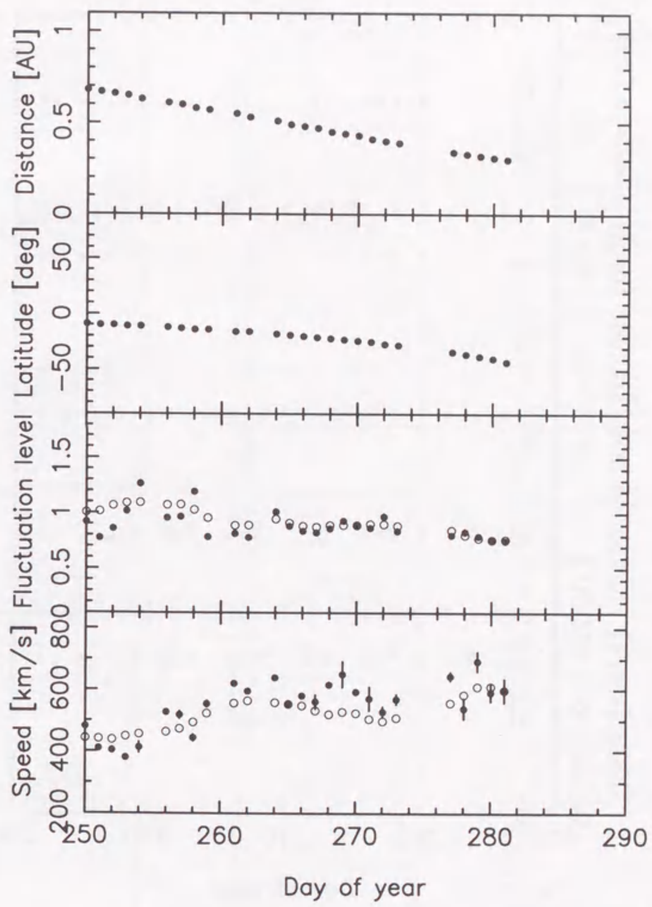


Figure 5.13: Comparison between observed and line of sight integrated IPS values of speed and relative electron density fluctuations for radio source 3C283.

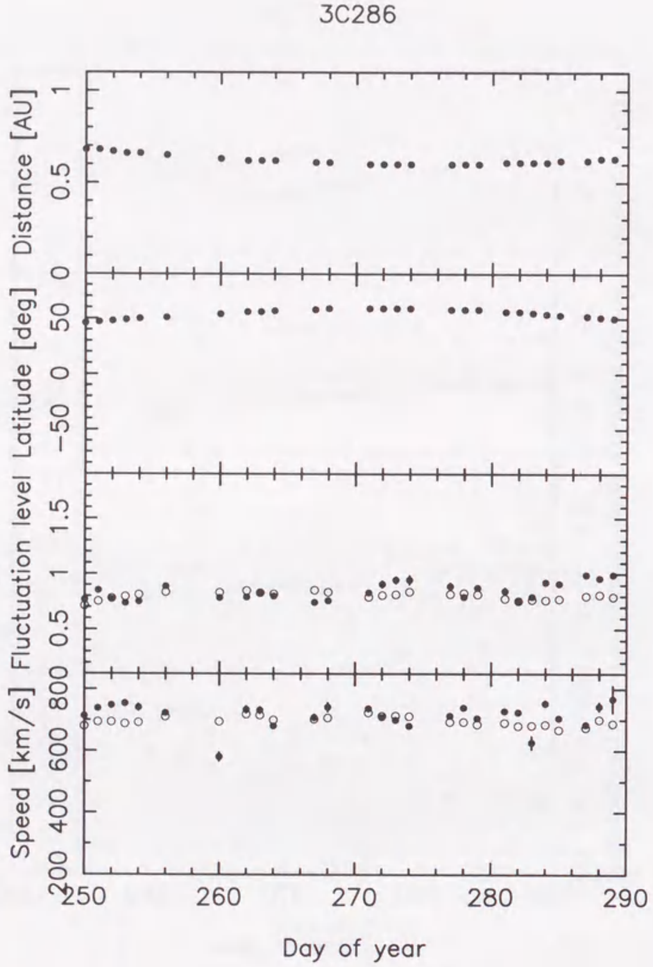


Figure 5.14: Comparison between observed and line of sight integrated IPS values of speed and relative electron density fluctuations for radio source 3C286.



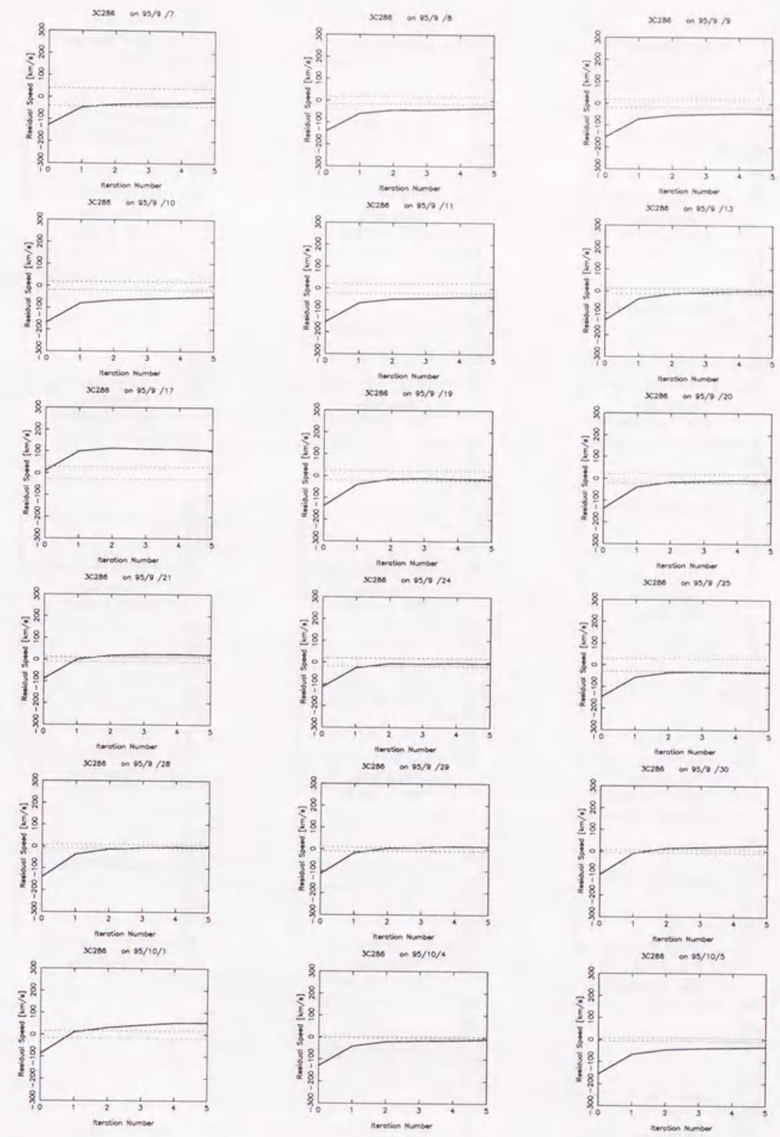


Figure 5.15: Convergence of speed with iteration (Steps 2 and 3). The solid line is the subtraction between observation and calculation, and the area within the dashed line represents the range of the observation error.

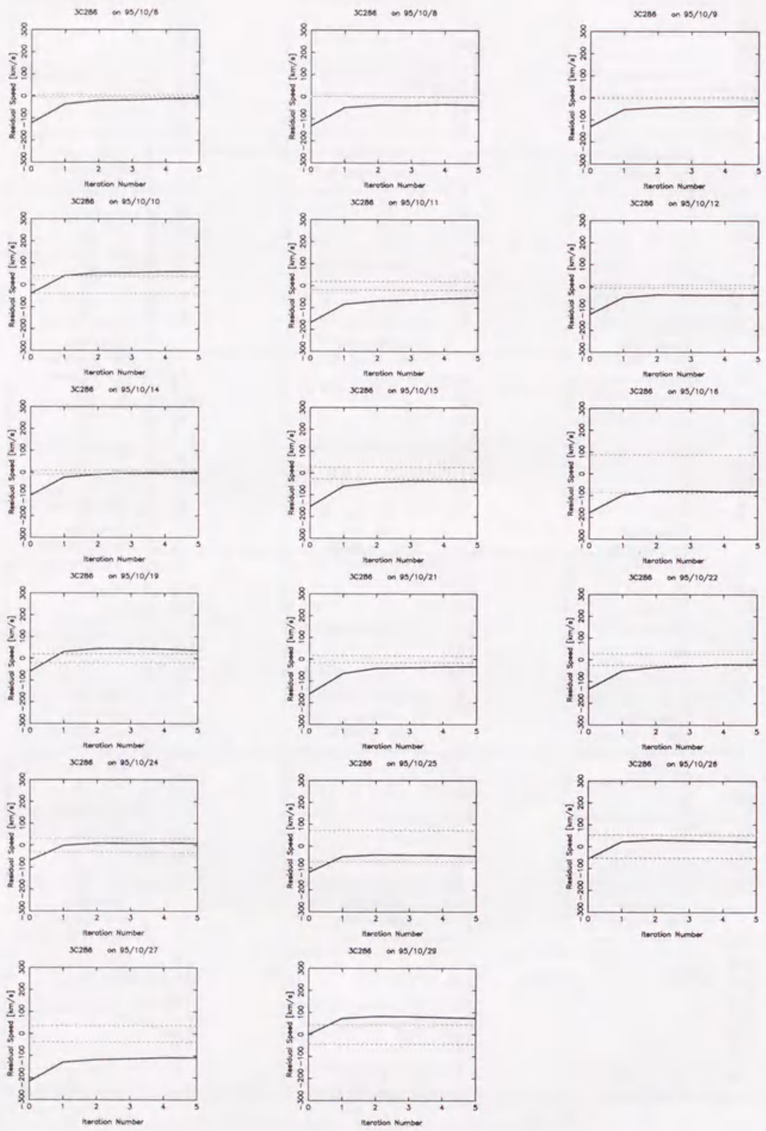


Figure 5.15: Continuation



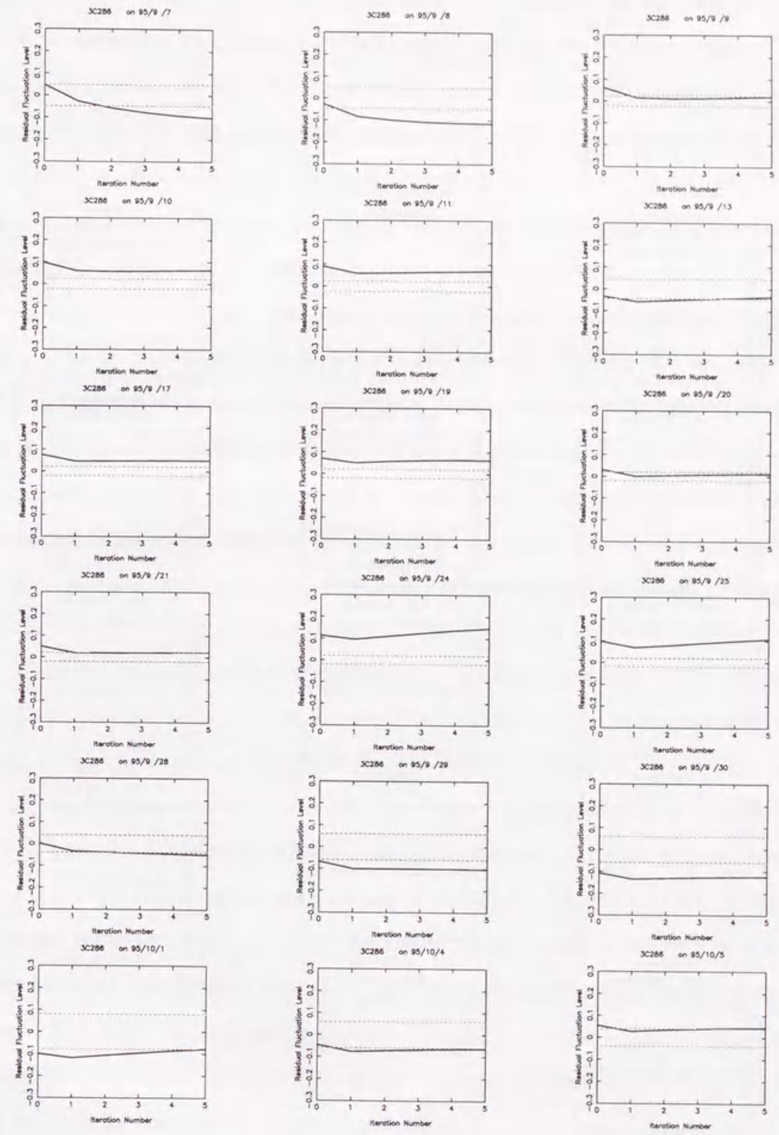


Figure 5.16: Convergence of relative electron density fluctuation level with iteration (Steps 2 and 3). The solid line is the subtraction between observation and calculation, and the area within the dashed line represents the range of the observation error.

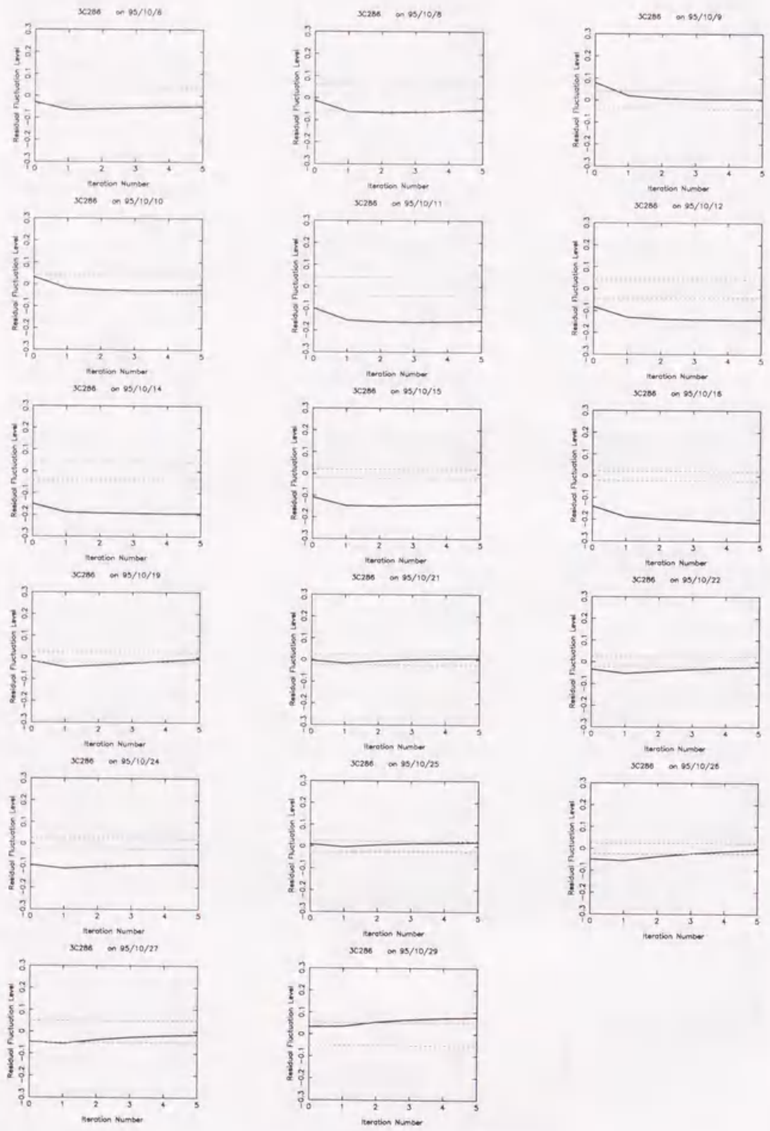


Figure 5.16: Continuation



observations with synthetic IPS observations, calculated by the line of sight integration through the reconstructed solar wind model using the weighting function (Equation 5.15). Figure 5.12 shows this comparison for the IPS source 3C241 over one solar rotation. Even though in this period the line of sight to 3C241 covers a fairly wide range of heliocentric distances (0.3-0.8 AU) and heliographic latitudes (10°-35°), the agreement is quite satisfactory except for fine variations. We should note that the reconstructed maps display the global structure of the solar wind, because the averaging process might remove effect of the transient phenomena such as CMEs, solar bursts, and interplanetary shocks. Figure 5.13 shows an example (3C283) that the source position is located in the southern hemisphere. Figure 5.14 is 3C286 which keeps high latitudes, and the IPS with this source observed continuous high speeds around 650 to 750 km $s^{-1}$ and low density fluctuation levels lower than 1.0. They indicate strong reliability of the CAT analysis for the reconstruction of the solar wind structure. The differences between the observation and the calculation are displayed per iteration for each source to monitor convergence of the CAT program. We plot these values of speed and relative density fluctuation level for 3C286 in Figure 5.15 and 5.16. The vertical area within the dashed lines represents the range of the observation error. These figures indicate that three iterations are almost enough to give the solution convergence, though there are several cases that the differences converge increasing with iteration. Other sources show the similar convergence with iteration. Table 5.1 shows how the CAT results become more stable with increasing number of iterations. The second and third lines show the r.m.s. values of differences between the observed and calculated values of the IPS speed and electron density fluctuations. This table also indicates that the solution converges after only three iterations. In the three iterations, the r.m.s. differences between the observed and calculated values for all the data are 71.8 km $s^{-1}$ for the speed and 0.137 for the relative electron density fluctuations. These values seem to be large, but reasonable, because the average observation errors are 39.6 km $s^{-1}$ for the speed and 0.13 for the relative density fluctuations.

Table 5.1: The r.m.s. differences between observed and line of sight integrated IPS values. The iteration number '0' corresponds to the initial maps at Step 1 of the reconstruction algorithm.

| Iteration Number | 0 | 1 | 2 | 3 | 4 | 5 |
|---|---|---|---|---|---|---|
| Wind speed (km $s^{-1}$) | 89.4 | 78.1 | 73.8 | 71.8 | 70.4 | 69.4 |
| Density fluctuations | 0.161 | 0.149 | 0.142 | 0.137 | 0.133 | 0.130 |

### 5.6.1 Relation of Wind Speed and Electron Density Fluctuations

We examine the speed dependence of the electron density fluctuations from the two maps in Figure 5.11, using the assumption that the density fluctuation level $\delta N_e$ is a power-law function of speed $V$ with an index $\gamma$,

$$\delta N_e(r) \propto r^{-2} V^{-\gamma(r)}, \tag{5.23}$$

where $r$ is the heliocentric distance. First we prepare a data set of pairs of speed and relative electron density fluctuations by combining values from the same longitude and latitude bins in the maps. The range of solar wind speeds is split up into speed ranges of 100 km $s^{-1}$ wide, i.e. 200-300 km $s^{-1}$, 300-400 km $s^{-1}$, etc. The pairs of data are then sorted according to these speed groups, and an average for the relative electron density fluctuations is calculated for each group. Figure 5.17 shows the averages as a function of speed using logarithmic axes; vertical and horizontal bars represent standard deviations for the density fluctuations and bin widths for the speed groups, respectively. The solid line is a least-squares power-law fit of $\delta N_e \propto V^{-\gamma}$ with $\gamma = 0.5 \pm 0.15$. This result confirms the validity of assumptions made for the speed dependence of the electron density fluctuations based on the latitudinal structure of solar wind speed for observations beyond 0.3 AU by Kakinuma et al. [2] and Kojima et al. [29].

We can determine the radial dependence of the power-law index $\gamma$ by applying the above power-law relation of speed and electron density fluctuations to the results of previous workers who made observations of the electron density fluctuations at small scales by radio propagation methods. Coles et al. [35] estimated the fluctuation level of electron density at solar distances of 5 to 15 $R_\odot$ using a bandwidth coherent measurement



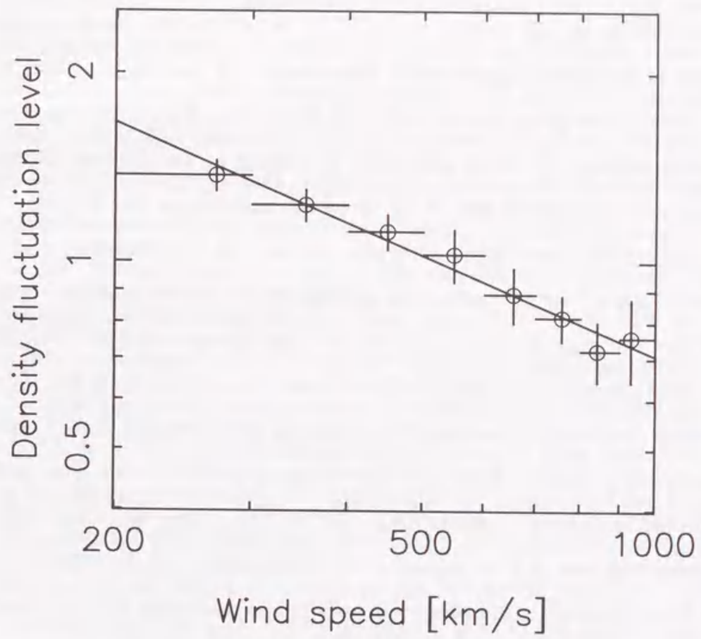


Figure 5.17: Relation between the speed and relative density fluctuations in the reconstructed solar wind. The solid line is the best fit power-law relation of $\delta N_e \propto V^{-0.5\pm0.15}$. Data are averaged in 100 km $s^{-1}$ speed bins (indicated by horizontal bars). The vertical bars are standard deviations for the electron density fluctuations.

Table 5.2: The radial variation of the power-law index $\gamma$ in the power-law relation $\delta N_e \propto V^{-\gamma}$. Each $\gamma$ is derived from the results of Coles et al. (0.02∼0.07 AU), Manoharan (0.1∼0.2 AU), Jackson et al. (1 AU), and ours (0.3∼0.8 AU).

| Solar distance [AU] | 0.02∼0.07 | 0.1∼0.2 | 0.3∼0.8 | 1.0 |
|---|---|---|---|---|
| Power-law index $\gamma$ | 1.8 | 1.2 | 0.35∼0.65 | 0.3∼0.6 |

technique. They measured the microscale fluctuations at scales of the order of 10 km during solar minimum, and showed that $\delta N_e^2$ in the polar fast stream is a factor of 15 smaller than in the lower latitude wind. Manoharan [15] has reported that the density fluctuation level in the polar regions is about 2.5 times less than in the equatorial regions during solar minimum. This was estimated by looking at the turnover distances of the scintillation index between 28 and 44 $R_\odot$ using the assumption that $\delta N_e \propto r^{-2.2}$ without compensating for the line of sight integration inherent in interplanetary scintillation. If we assume 750 km s$^{-1}$ for the polar wind and 350 km s$^{-1}$ for the equatorial wind, $\gamma \simeq 1.8$ is derived from the result by Coles et al. [35] for solar distances of 5 to 15 $R_\odot$, and $\gamma \simeq 1.2$ from the result by Manoharan [15] for the distance range of 28 to 44 $R_\odot$. Jackson et al. [14] compared the density fluctuation distribution, reconstructed from Cambridge IPS index data using a different CAT technique from ours, with *in situ* observations of the IMP spacecraft, and found a relation $\delta N_e = N_e^{0.3}$ at 1 AU. Assuming that either mass flux $N_e V$ or momentum flux $N_e V^2$ is the same for different speed streams, this relation implies $\gamma$ =0.3 or 0.6, respectively. Including these observational results and ours, the estimated power indices $\gamma$ are listed in Table 5.2. We find that $\gamma$ decreases with heliocentric distance.

### 5.6.2 Speed Dependence of Fractional Electron Density Fluctuations

The fractional density fluctuations (i.e. the density fluctuations normalized by density) are important for solar wind turbulence, whereas the electron density fluctuations directly affect the IPS velocity measurements. From the speed correlation of electron density fluctuations $\delta N_e \propto V^{-0.5}$, the speed correlation of fractional electron density fluctuations is derived as $\delta N_e/N_e \propto V^{+0.5}$ or $\delta N_e/N_e \propto V^{+1.5}$, if we assume mass flux $N_e V$ or momentum



flux $N_e V^2$ is identical among different speed flows, respectively [36, 37]. In either case, it follows that the power index of $V$ is positive, i.e., that the fractional electron density fluctuation level in the high-speed wind is larger than in the low-speed wind.

An independent confirmation of the relation between speed and fractional electron density fluctuations can be obtained by applying the functional form $\delta N_e = \mu V^\nu N_e^\beta$ to the correlation between the relative fluctuation level and proton temperature investigated by Celnikier et al. [38]. Celnikier et al. [38] measured density fluctuations using a radio wave propagation technique between two satellites at 1 AU. Their measurements indicate that the fractional electron density fluctuations $\delta N_e/N_e$ in the high proton temperature wind is larger than that in the low temperature wind. Figure 5.18 is reproduced from Figure 13 of Celnikier et al. [38]. Although the data are classified by temperature in three groups in the original figure, we convert the temperature to speed using the relationship derived from Helios 1 data by Lopez and Freeman [39] who showed that high-speed wind has higher temperature than low-speed wind at 1 AU: $T^{1/2} = 0.031V - 4.39$ for the low-speed wind (< 500 km s$^{-1}$), and $T = 0.77V - 265$ for the high-speed wind (> 500 km s$^{-1}$). The three temperature groups correspond to speed ranges of 285–391 km s$^{-1}$ (low-speed), 391–525 km s$^{-1}$ (medium-speed), and 525–733 km s$^{-1}$ (high-speed), respectively. To simplify the following discussion, the velocities in each group are fixed to an average value for the calculation of $\beta$. First, the power index $\beta$ is computed for each speed group by a least-squares fit; we obtain $\beta = 0.795$ for the low-speed wind, $\beta = 0.845$ for the medium-speed wind, and $\beta = 0.945$ for the high-speed wind. Then $\mu$ and $\nu$ are calculated using as the representative speed for each group the upper boundary speed (391, 525, and 733 km s$^{-1}$), the lower boundary speed (285, 391, 525 km s$^{-1}$), and the median speed (338, 458, 629 km s$^{-1}$), respectively. The differences among the three calculated values of $\nu$ are quite small; $\nu$ is 0.31 for the upper boundary speed, 0.30 for the median speed, and 0.31 for the lower boundary speed. The best-fits of the form $\delta N_e = \mu V^\nu N_e^\beta$ are denoted by solid lines in Figure 5.18. In the high-speed group, we did not use the data whose $log < N_e >$ is larger than 1 because the combination of high temperature and high density leads us to suspect that these data are not observed in high-speed streams, but

rather in interaction regions. The form $\delta N_e = \mu V^\nu N_e^\beta$ gives following two equations,

$$\frac{\delta N_e}{N_e} = \mu (N_e V)^{\beta-1} V^{\nu-\beta+1}, \quad (5.24)$$

$$\frac{\delta N_e}{N_e} = \mu (N_e V^2)^{\beta-1} V^{\nu-2\beta+2}. \quad (5.25)$$

Equation 5.24 represents the speed correlation of the fractional electron density fluctuations when $N_e V$ is equal for different speed flows, while Equation 5.25 represents the speed correlation when $N_e V^2$ is equal. Using the average values $\nu$=0.31 and $\beta$=0.86, we obtain for the power indices of the speed: $\nu - \beta + 1$ =0.45 and $\nu - 2\beta + 2$ =0.59, respectively. In either case, the fractional density fluctuations $\delta N_e/N_e$ are larger in the high-speed wind than in the low-speed wind. This is in good agreement with our result. Since density fluctuations depend on the scale length, it should be noted that the temporal frequency range analyzed by Celnikier et al. [38] is from 0.019 to 16 Hz which covers the frequency range of intensity scintillations.

Interestingly, these results with respect to the small scale size are not consistent with those at large scale size. The relation between speed and fractional density fluctuations at larger scales has been discussed by Huddleston et al. [40], Woo et al. [41], and Pätzold et al. [42], who showed that the fractional density fluctuations in the low-speed wind are higher than in the high-speed wind. Huddleston et al. [40] analyzed the density fluctuations in a period range of 10 minutes to 1 hour using *in situ* plasma measurements at 1 AU. This period range corresponds to spatial scales much larger than those discussed above. They reported that the fractional electron density fluctuations in plasma sheets are larger than that in flows from coronal holes. This result differs from our result and that of Celnikier et al. [38], indicating a scale-size dependence of the relation between wind speed and fractional density fluctuations. Woo et al. [41] measured the fractional electron density fluctuations $\delta N_e/N_e$ in a frequency range of $6 \times 10^{-5}$ to $8 \times 10^{-4}$ Hz at heliocentric distances between 5 and 40 $R_\odot$ using 1991 Ulysses dual-frequency ranging measurements. They reported that $\delta N_e/N_e$ varies from 20% in the slow wind near the neutral sheet to 1% in the fast wind far from the neutral sheet, though the line of sight integration effect was not considered. Pätzold et al. [42] also made dual-frequency Doppler measurements of the Ulysses down link carrier signals recorded during the spacecraft's



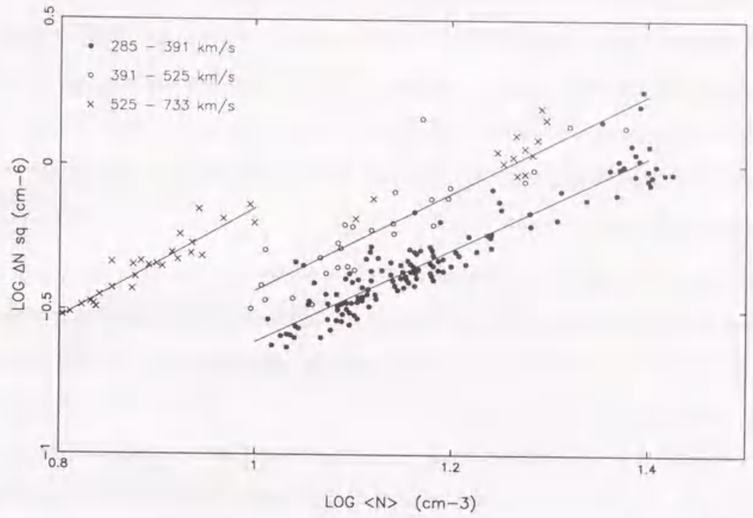


Figure 5.18: Log (electron density fluctuation squared) as a function of log (mean density). This is reproduced from Figure 13 in the paper of Celnikier et al., but data are classified by speed. Solid lines are the best-fit lines for the relation $\delta N_e = \mu V^\nu N_e^\beta$.

1995 solar conjunction. They showed that the fractional electron density fluctuations at 25 $R_\odot$ are larger in the coronal streamer than in the coronal hole by a factor of 5.

### 5.6.3 Radial Evolution of the Speed Dependence of Fractional Electron Density Fluctuations

It is shown that the speed dependence of the electron density fluctuations varies with radial distance from the Sun. Using the assumption that either $N_e V$ or $N_e V^2$ is conserved among different speed streams, the power-law indices $\xi$ on $\delta N_e/N_e \propto V^\xi$ at various solar distances can be derived from the indices $\gamma$ listed in Table 2. The results of this calculation, together with Celnikier's results, shows the radial evolution of the correlation between solar wind

speed and fractional electron density fluctuations (Figure 5.19). Although we assumed 750 km $s^{-1}$ for the polar wind and 350 km $s^{-1}$ for the equatorial wind, there is a possibility that the equatorial wind at the solar distances of 5 to 15 $R_\odot$ or even at 28 to 44 $R_\odot$ has not yet reached its asymptotic value [36, 43]. Smaller values for the equatorial solar wind speed at these distances will yield larger values for $\xi$. The result of Manoharan [15] involves the line of sight integration; The compensation for effect of the line of sight integration may produce larger difference between fast and slow streams for electron density fluctuations, and then will yield smaller value of $\xi$.

Summarizing the results of the previous works introduced in this paper [35, 15, 38, 14] and ours, we conclude that the power-law index in $\delta N_e/N_e \propto V^\xi$ has a tendency to grow with heliocentric distance, and to become approximately constant beyond 0.3 AU. This suggests that the fast solar wind obtains its strong turbulence at heliocentric distances inside 0.3 AU. We know of no physical process that can explain why the faster wind has larger fractional density fluctuations on the scales around 100 km at heliocentric distances larger than 0.3 AU. However, if the density fluctuations are due to Alfvén waves, the radial growth of density fluctuations can be interpreted as the amplitude evolution of the Alfvén waves. There may be a connection with the existence of a local flattening in the density fluctuation power spectrum around scales of 100 km [45, 46], implying an enhancement of density fluctuations at small scales. *Grall et al.* [47] have suggested from radio scattering observations that the enhanced small-scale fluctuations are independent of the large-scale turbulence and are therefore likely to be due to a different physical mechanism.

Here, it should be recognized that the density fluctuations depend on the scale sizes. Marsch and Tu [44] made a spectral analysis of the fractional proton density fluctuations $\delta N_P/N_P$ measured by the Helios spacecraft at distances beyond 0.3 AU. They found that the spectral power density in the high-speed wind increases with distance from the Sun, while in the low-speed wind the power density is almost independent of distance. The spectral index of the high-speed wind shows a flattening at the large wavenumbers. A remarkable point is that the spectral power density of the high-speed wind becomes comparable to that of the low-speed wind around wavenumbers of $2 \times 10^{-5}$ $km^{-1}$. Their



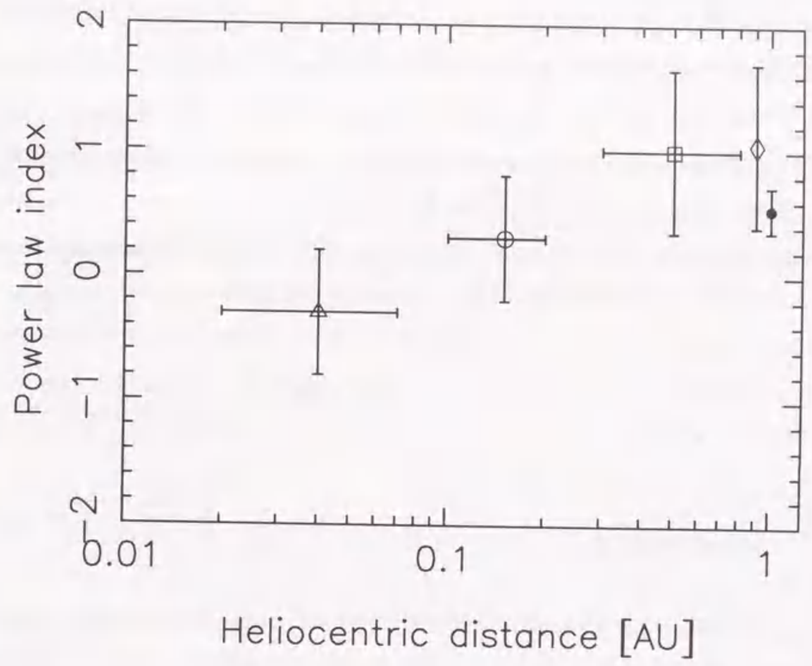


Figure 5.19: Speed dependence of fractional electron density fluctuations ($1-\gamma$ and $2-\gamma$) versus radial distance. In the vertical bars, the top is $2-\gamma$, derived with momentum flux density constant; the bottom is $1-\gamma$, derived with mass flux density constant. The horizontal bars represent the distance range of the observations. A triangle (△) at 0.04 AU is from coherence bandwidth measurements of IPS [Coles et al., 1996]. An open circle (◯) at 0.2 AU is from interplanetary scintillation data in the assumption of $\delta N_e \propto r^{-2.2}$ [Manoharan, 1993]. Our results estimated from the CAT analysis are shown with an open square (□). The point marked by an open diamond (◇) at 1 AU are from CAT analysis combining Cambridge interplanetary scintillation index data with IMP spacecraft data [Jackson et al., 1996,1997]. A solid circle (•) is from phase scintillation experiments using ISEE 1 and 2 satellites [Celnikier et al., 1987].

results suggest that the fractional density fluctuation level of the fast wind may exceed that of the slow wind at larger wavenumbers. This suggestion supports our result about a positive correlation between speed and fractional density fluctuations, though there is possibly a difference between proton density fluctuations and electron density fluctuations. There are reports that the proton might be efficiently heated by wave dissipation [e.g., McKenzie et al, 1995], based on the evidence that $T_p > T_e$ in the fast wind and $T_p < T_e$ in the slow wind at 1 AU.

We have discussed density fluctuations at spatial scales smaller than $10^3$ km, and obtained the result that the higher fluctuation level is observed in the high-speed, high-latitude region outside 0.3 AU, which is spatially uniform and separated from the low-speed wind at low-latitudes with a sharp speed gradient as shown in Figure 5.11. This fact is important because it may indicate that the growth of the fractional electron density fluctuations in the high-speed wind with heliocentric distance is not caused by a velocity shear effect.

## 5.7 Summary

We have developed a CAT analysis method to reconstruct the unbiased solar wind structure from IPS observations which are subject to line of sight integration. Scintillation index data are used together with IPS velocity data for the CAT analysis. The scintillation index data were needed to obtain the electron density fluctuations, as well as to determine the weighting function along the line of sight. The CAT reconstructed distribution maps show that the fast solar wind recovers the high speed and low density fluctuations at the high-latitude regions. The comparison of the distribution maps of speed and electron density fluctuations provided the best fit power-law relation of $\delta N_e \propto V^{-\gamma}$ with $\gamma = 0.5 \pm 0.15$. The power-law index $\gamma = 0.5$ implies the important result that $\delta N_e / N_e$ increases with speed if we suppose that either mass flux $N_e V$ or momentum flux $N_e V^2$ is invariant between different speed flows. It should be noted that this result was obtained for the electron density fluctuations of micro-scale sizes around 100 km and at heliocentric distances beyond 0.3 AU, because the relation between wind speed and fractional density



fluctuations at large scales indicates the opposite characteristics.

The CAT technique is a powerful tool to deconvolve the line of sight integration in the IPS observations. The technique holds considerable promise for studying solar wind plasma with IPS observations. Here we have described the average distribution between 0.3 and 0.8 AU in the wind speed and electron density fluctuations, based on the constant speed assumption. The more detailed turbulent behavior of the solar wind plasma will be clarified not only by high-resolution observations analyzed using CAT techniques without the constant speed assumption, but also by observations of solar wind acceleration regions near the Sun.

# Bibliography


[1] R. R. Grall, W. A. Coles, M. T. Klinglesmith, A. R. Breen, P. J. S. Williams, Jussi Markkanen, and Ruth Esser, Rapid acceleration of the polar solar wind, *Nature*, **379**, pp.429–432, 1996.

[2] T. Kakinuma, H. Washimi and M. Kojima, Three-dimensional distribution of the solar wind velocity deduced from IPS observations, *Proceedings of the STIP Symposium on Solar Radio Astronomy, Interplanetary scintillation and coordination with spacecraft*, edited by M. A. Shea, D. F. Smart, D. J. McLean and G. J. Nelson, AFGL Special Report #233, pp.153–162, 1982.

[3] K. Asai, M. Kojima, M. Tokumaru, A. Yokobe, B. V. Jackson, P. Hick, and P. K. Manoharan, Heliospheric tomography using interplanetary scintillation observations III - The correlation between speed and electron density fluctuations in the solar wind, *Journal of Geophysical Research*, **103**, pp.1991–2001, 1998.

[4] P. Gilbert, Iterative methods for the three-dimensional reconstruction of an object from projections, *Journal of Theoretical Biology*, **36**, pp.105–117, 1972.

[5] R. N. Bracewell, Strip integration in radio astronomy, *Australian Journal of Physics*, **9**, pp.198–217, 1956.

[6] T. R. Marsh, and K. Horne, Images of accretion discs - II. Doppler tomography, *Monthly Notices of the Royal Astronomical Society*, **235**, pp.269–286, 1988.

[7] D. R. Gies, A. W. Fullerton, C. T. Bolton, W. G. Bagnuolo Jr., M. E. Hahula, and R. Wiemker, HD 53975: An O-type spectroscopic binary with a large mass ratio, *The Astrophysical Journal*, **422**, pp.823–830, 1994.







[8] P. F. Worcester, B. D. Cornuelle, and R. C. Spindel, A review of ocean acoustic tomography: 1987-1990, *Reviews of Geophysics (supplement)*, pp.557–570, 1991.

[9] D. L. Anderson, and A. M. Dziewonski, Seismic Tomography, *Scientific American*, **251**, No.4, PP.60–68, 1984.

[10] M. E. Gorbunov, Three-dimensional satellite refractive tomography of the atmosphere: Numerical simulation, *Radio Science*, **31**, No.1, pp.95–104, 1996.

[11] B. V. Jackson, R. A. Howard, N. R. Sheeley, Jr., D. J. Michels, M. J. Koomen, and R. M. E. Illing, Helios Spacecraft and Earth perspective observations of three looplike solar mass ejection transients, *Journal of Geophysical Research*, **90**, pp.5075–5081, 1985.

[12] B. V. Jackson, and H. R. Froehling, Three-dimensional reconstruction of coronal mass ejections, *Astronomy and Astrophysics*, **299**, pp.885–892, 1995.

[13] S. Zidowitz, B. Inhester, and A. Epple, The three-dimensional structure of the solar corona, in *Solar Wind Eight, AIP Conference Proceedings 382*, edited by D. Winterhalter, J. T, Gosling, S. R. Habbal, W. S. Kurth, and M. Neugebauer, Woodbury, pp.165–168, 1995.

[14] B. V. Jackson, P. L. Hick, M. Kojima and A. Yokobe, Heliospheric tomography using interplanetary scintillation observations I – Combined Nagoya and Cambridge data, *Journal of Geophysical Research*, 1998 (in press).

[15] P. K. Manoharan, Three dimensional structure of the solar wind: variation of density with the solar cycle, *Solar Physics*, **148**, pp.153–167, 1993.

[16] W. A. Coles, Interplanetary scintillation, *Space Science Review*, **21**, pp.411–425, 1978.

[17] L. T. Little, and A. Hewish, Interplanetary scintillation and its relation to the angular structure of radio sources, *Monthly Notices of the Royal Astronomical Society*, **134**, pp.221–237, 1966.

[18] J. W. Armstrong, and W. A. Coles, Analysis of Three-station interplanetary scintillation, *Journal of Geophysical Research*, **77**, pp.4602–4610, 1972.

[19] G. Bourgois, W. A. Coles, G. Daigne, J. Silen, T. Turunen, and P. J. Williams, Measurements of the solar wind velocity with EISCAT, *Astronomy and Astrophysics*, **144**, pp.452–462, 1985.

[20] J. H. Wolfe, The large-scale structure of the solar wind, in *Solar Wind*, edited by C. P. Sonett, P. J. Coleman, Jr., and J. M. Wilcox, pp.170-201, NASA, Washington, D.C., 1971.

[21] M. Kojima, Anisotropic structure of solar-wind plasma irregularities observed with interplanetary scintillations, *Publications of the Astronomical Society of Japan*, **31**, pp.231–249, 1979.

[22] M. Kojima, and T. Kakinuma, Anisotropic structure of micro-turbulence in the solar wind observed with interplanetary scintillation, *Journal of Geomagnetism and Geoelectricity*, **40**, pp.1303–1318, 1988.

[23] V. I. Tatarski, *Wave propagation in a turbulent medium*, McGraw-Hill, New York, 1961.

[24] A. T. Young, Interpretation of interplanetary scintillation, *Astrophysical Journal*, **168**, pp.543–562, 1971.

[25] T. Kakinuma, H. Washimi, and M. Kojima, On the analysis of the observations of interplanetary scintillations obtained with three spaced receivers, *Publications of the Astronomical Society of Japan*, **25**, pp.271–280, 1973.

[26] W. A. Coles, and J. P. Filice, Changes in the microturbulence spectrum of the solar wind during high-speed streams, *Journal of Geophysical Research*, **90**, pp.5082–5088, 1985.

[27] P. K. Manoharan, M. Kojima, and H. Misawa, The spectrum of electron density fluctuations in the solar wind and its variations with solar wind speed, *Journal of Geophysical Research*, **99**, pp.23411–23420, 1994.



[28] Y. Yamauchi, M. Kojima, M.Tokumaru, H. Misawa, H. Mori, T. Tanaka, H. Takaba, T. Kondo, and P. K. Manoharan, Micro-turbulence in the solar wind at 5–76 Rs observed with interplanetary scintillation, *Journal of Geomagnetism and Geoelectricity*, **48**, pp.1201-1217, 1996.

[29] M. Kojima, M. Tokumaru, H. Watanabe, A. Yokobe, K. Asai, B. V. Jackson, and P. L. Hick, Heliospheric tomography using interplanetary scintillation observations II – Latitude and heliocentric distance dependence of solar wind structure at 0.1-1 AU, *Journal of Geophysical Research*, **103**, pp.1981–1989, 1998.

[30] A. C. S. Readhead, Interplanetary scintillation of radio sources at meter wavelength, II, theory, *Monthly Notices of the Royal Astronomical Society*, **155**, pp.185–197, 1971.

[31] J. W. Armstrong, and W. A. Coles, Interplanetary scintillation of PSR 0531+21 at 74MHz, *Astrophysical Journal*, **220**, pp.346–352, 1978.

[32] G. R. Gapper, A. Hewish, A. Purvis, and P. J. Duffett-Smith, Observing interplanetary disturbances from the ground, *Nature*, **296**, pp.633–636, 1982.

[33] K. Asai, Y. Ishida, M. Kojima, K. Maruyama, H. Misawa, and N. Yoshimi, Multi-station system for solar wind observations using the interplanetary scintillation method, *Journal of Geomagnetism and Geoelectricity*, **47**, pp.1107–1112, 1995.

[34] W. A. Coles, and J. J. Kaufman, Solar wind velocity estimation from multi-station IPS, *Radio Science*, **13**, pp.591–697, 1978.

[35] W. A. Coles, R. R. Grall, M. T. Klinglesmith, and G. Bourgois, Solar cycle changes in the level of compressive microturbulence near the Sun, *Journal of Geophysical Research*, **100**, pp.17069–17079, 1995.

[36] R. Schwenn, Large-scale structures of the interplanetary medium, in *Physics of the Inner Heliosphere I, Large Scale Phenomena*, edited by R. Schwenn and E. Marsch, pp.99-181, Springer-Verlag, New York, 1990.

[37] J. L. Phillips, S. J. Bame, A. Barnes, B. L. Barraclough, W. C. Feldman, B. E. Goldstein, J. T. Goslong, G. W. Hoogeveen, D. J. McComas, M. Neugebauer, and

S. T. Suess, Ulysses solar wind plasma observations from pole to pole, *Geophysical Research Letters*, **22**, pp.3301-3304, 1995.

[38] L. M. Celnikier, L. Muschietti, and M. V. Goldman, Aspects of interplanetary plasma turbulence, *Astronomy and Astrophysics*, **181**, pp.138–154, 1987.

[39] R. E. Lopez, and J. W. Freeman, Solar wind proton temperature-velocity relationship, *Journal of Geophysical Research*, **91**, pp.1701–1705, 1986.

[40] D. E. Huddleston, R. Woo, and M. Neugebauer, Density fluctuations in different types of solar wind flow at 1 AU and comparison with results from Doppler scintillation measurements near the Sun, *Journal of Geophysical Research*, **100**, pp.19951–19956, 1995.

[41] R. Woo, J. W. Armstrong, M. K. Bird, and M. Pätzold, Variation of fractional electron density fluctuations inside 40 $R_\odot$ observed by Ulysses ranging measurements, *Geophysical Research Letters*, **22**, pp.329–332, 1995.

[42] M. Pätzold, J. Karl, and M. K. Bird, Coronal radio sounding with Ulysses: dual-frequency phase scintillation spectra in coronal holes and streamers, *Astronomy and Astrophysics*, **316**, pp.449–456, 1996.

[43] M. K. Bird, H. Volland, M. Pätzold, P. Edenhofer, S. W. Asmar, and J. P. Brenkle, The coronal electron density distribution determined from dual-frequency ranging measurements during the 1991 solar conjunction of the Ulysses spacecraft, *Astrophysical Journal*, **426**, pp.373–381, 1994.

[44] E. Marsch, and C. Y. Tu, Spectral and spatial evolution of compressible turbulence in the inner solar wind, *Journal of Geophysical Research*, **95**, pp.11945–11956, 1990.

[45] W. A. Coles, and J. K. Harmon, Propagation observations of the solar wind near the Sun, *Journal of geophysical Research*, **337**, pp.1023–1034, 1989.

[46] W. A. Coles, W. Liu, J. K. Harmon, and C. L. Martin, The solar wind density spectrum near the Sun: Results from Voyager radio measurements, *Journal of Geophysical Research*, **96**, pp.1745-1755, 1991.



[47] R. R. Grall, W. A. Coles, S. R. Spangler, T. Sakurai, and J. K. Harmon, Observations of field-aligned density microstructure near the Sun, *Journal of Geophysical Research*, **102**, pp.263-273, 1997.

[48] L. M. Celnikier, C. C. Harvey, R. Jegou, M. Kemp, and P. Moricet, A determination of the electron density fluctuation spectrum in the solar wind, using ISEE propagation experiment, *Astronomy and Astrophysics*, **126**, pp.293–298, 1983.

# Chapter 6

# Conclusion

The UHF radio telescope dedicated to the IPS observations requires high sensitivity. For this requirement, we made various development and improvement of the system. To maximize aperture efficiency of the asymmetric parabolic cylinder antenna, the primary feed system was designed with the optimum structure parameters. The optimum design produced high aperture efficiency of 71%. The primary feed system of the antenna is a phased array with a corner reflector. Gain and phase of all the array-elements should be calibrated for source-tracking with the phased array. The loop-method keeps gain errors less than 0.1 dB(rms) and phase errors less than 2°(rms). The UHF radio telescope at the Kiso station achieved to have the minimum detectable flux density of 0.43 Jy at a bandwidth of 10 MHz and an integration time of 100 ms. The Fuji, Toyokawa, and Sugadaira telescopes improved the sensitivity with a reduction of the receiver system noise, making the low noise amplifiers.

These development and improvement of the instruments enable us to measure a large number of IPS radio sources. This makes it possible to apply the computer assisted tomography (CAT) technique to the IPS analysis. A thousand lines of sight are available in one solar rotation period. The CAT analysis could reconstruct solar wind distributions eliminating the line-of-sight integration effect on the IPS. The fast solar wind recovered high speeds around 800 km $s^{-1}$ at the high latitudes. The sharp gradient appeared in the boundary between high-speed and low-speed regions. The relation between speed and electron density fluctuations indicates $\delta N_e \propto V^{-0.5}$ at the heliocentric distances of 0.3 to 0.8 AU on the scales around 100 km. This relation suggests that the fractional electron





density fluctuations have positive correlation with the speed. The next study will solve the reason why the faster solar wind has larger fractional density fluctuations at this scale size, which might be a key to understand the acceleration mechanism of the solar wind.

The elimination of the line-of-sight integration effect will take the IPS observations into the next stage. The UCSD group made a different kind of IPS analysis to remove the integration effect, and obtained the interesting result that the fast solar wind exceeds 600 km $s^{-1}$ at 10 solar radii. The clarification of the solar wind acceleration mechanism needs detail observations of the acceleration regions near the Sun. A non-radial component of the velocity ("random velocity") cannot be neglected near the Sun. Our four-station system has redundancy to estimate the random velocity component. This measurement will provide more detail information on turbulent phenomena in the solar wind. The comparison with the other observations is also significant for the solar wind study in the near-Sun regions, such as SOHO and SPARTAN 201.

The measurement of the sunspot number shows the solar activity is gradually increasing from the solar minimum in 1997. The ULYSSES spacecraft will make the second approach to the solar poles in 2000 and 2001 when the solar activity is expected to be around the peak. This mission will bring deep understanding about various phenomena in the interplanetary space during the solar maximum phase. The 21st century will have many opportunities to take human beings outside the Earth. At that time, energetic particles from the Sun are very dangerous for a human body as well as instruments of the satellite. The space weather prediction is one of the current hot topics in the solar-terrestrial physics research. The IPS can contribute to the predictions by observing the transient phenomena such like CMEs and interplanetary shocks.